Vers un nouveau cadre de modélisation rhéologique de la banquise

Lucas Girard

Laboratoire de Glaciologie et Géophysique de l'Environnement

LABORATOIRE DE GLACIOLOGIE ET GÉOPHYSIQUE DE
L'ENVIRONNEMENT - UMR 5183
Centre National de la Recherche Scientifique
Université Joseph Fourier - Grenoble I
54, rue Molière - Domaine Universitaire BP 96

38402 St-Martin d'Hères Cedex (France)

Vers un nouveau cadre de modélisation rhéologique de la banquise

Lucas GIRARD

Thèse de doctorat de l'Université de Grenoble

(Arrêtés ministériels du 5 juillet 1984 et 30 mars 1992)

Spécialité : Sciences de la Terre, de l'Univers et de l'Environnement

Date de Soutenance :
24 Septembre 2010

Composition du jury :

Daniel FELTHAM	Rapporteur
Jean SCHMITTBUHL	Rapporteur
Marie-Noëlle HOUSSAIS	Membre du jury
Jérôme WEISS	Membre du jury
Bernard BARNIER	Membre du jury
David AMITRANO	Président de jury

Rencontres

Cher lecteur, le document que tu tiens entre les mains est le fruit d'un travail effectué au laboratoire de Glaciologie et de Géophysique de l'Environnement, dans la charmante ville de Grenoble, non loin du 45^{e} parallèle, mais l'une des rencontres qui l'a motivé s'est déroulée à une latitude un peu plus élevée...

Durant l'été 2005, j'embarque à bord du brise glace suédois *Oden* pour traverser l'océan Arctique entre Barrow en Alaska et Longyearbyen au Spitsberg. Les 60 jours de traversée sont l'occasion d'observer la banquise sous toutes les coutures et d'en discuter avec les nombreux scientifiques à bord, notamment avec Göran Björk, océanographe à Göteborg. Lorsque je lui explique mon envie de travailler sur la dynamique de la banquise il me répond qu'il s'est lui même intéressé au sujet avant d'ajouter, l'air dépité, qu'il était rapidement passé à autre chose lorsqu'il s'était rendu compte que les modèles de banquise étaient incapables de reproduire correctement la dynamique de la glace. Selon ses dires, le comportement mécanique de la banquise n'avait pas encore été correctement identifié. Rencontre prémonitoire ? Les questions que Göran avait soulevées allaient m'occuper durant les trois années de ma thèse...

C'est une autre série de rencontres qui aura rendu possible l'aventure qu'on appelle une thèse. Celle de Jérôme, directeur de thèse exemplaire, qui a su m'aiguiller sur de bonnes pistes et a montré un intérêt sans limite pour mon travail, à qui j'associe également la rencontre de Bernard qui a co-dirigé ma thèse. C'est ensuite la rencontre de David Amitrano qui a permis d'initier le développement du nouveau modèle rhéologique dont nous avions commencé à réver. David s'est ensuite rapidement associé à mon travail et y a montré beaucoup d'intérêt.

La fin de l'aventure fût riche en rebondissements. Il y eut la brève rencontre de Daniel Feltham, rapporteur, qui, bravant les grêves et les annulations de vols, arriva à Grenoble juste à temps pour assister à ma soutenance avant de repartir illico pour Londres. Puis, une rencontre manquée avec Jean Schmittbuhl, également rapporteur de ma thèse qui ne pût être présent le jour *J*. Ma soutenance qui fût également l'occasion de faire la rencontre de Marie-Noëlle Houssais.

Bien d'autres rencontres ont ponctué les différentes étapes de l'aventure. Celle de Jean-Marc Molines, passionné (et passionnant !) ingénieur de recherche de l'équipe des océanographes grenoblois, et au LGGE quelques coups de pouce d'Olivier Gagliardini. Il y eut également la rencontre de l'équipe de modélisation de la banquise de Louvain-la-Neuve, Thierry Fichefet, Vincent Legat, Sylvain Bouillon, Olivier Lietaer, Martin Vancoppenolle, récemment rejoints par Pierre Mathiot.

Il y a finalement les rencontres quotidiennes, les plus importantes, avec les amis du labo ou d'ailleurs ! Celle de Pierre qui donnait lieu à des discussions enflammées sur la banquise (ou beaucoup d'autres choses) ! Celles de mes chers co-bureaux Cécile, Aurélien et Alex, mais aussi Floflo, Anne-soso, Vincent, Manu, Roro le mécano, machine à laver ou encore double montre ! Je n'oublierai pas les rencontres des sorties très socialisantes au resto U souvent animées par Florent. Il y eut aussi des rencontres montagnardes, tantôt orientées godille, comme avec Bazz et Nobru, Sisi, Soph, Alix, Marion, Rémi, Berna, Guillaume et Lionel,

tantôt plus goulotesques avec Adri et Marie, ou encore orientées goinfrage de fondue avant descente à la pleine lune, agrémentées d'une baignade rafaichissante, mais pour cette dernière catégorie les participants sont trop nombreux pour être cités ici !

Un clin d'oeil aux amis du grand Nord, dont Mats et Nic, bientôt j'irai vous re-rencontrer pour d'autres aventures à ski ou à voile !

Je n'oublie pas non plus les rencontres régulières avec la famille, bien présente pour m'écouter le jour de ma soutenance pour mon plus grand plaisir ! Je dois finalement mentionner que toute cette aventure n'aurait peut être pas eu lieu sans le coup de main de mes parents qui ont pris en charge les formalités administratives qui m'ont permis de décrocher un financement, alors que j'avais quitté la civilisation pendant quelques mois pour aller faire le tour du Spitsberg à ski. Un dernier clin d'oeil à ma grand-mère qui a pris soin de relire le chapitre d'introduction.

Vous l'aurez compris, *le mot-clé, pour savoir ce que nous sommes, eh bien, ce sont les rencontres que nous avons faites*. (Albert Jacquard)

Towards a new modeling framework for sea ice mechanics

Abstract

In this thesis, new approaches are used to model the mechanical behavior of sea ice and to evaluate sea ice models in terms of ice drift and deformation.

It is first shown how the statistical and scaling properties of sea ice drift and deformation can be used as an evaluation metric for sea ice models. These properties are known to play an important role regarding ice growth estimates and should therefore be captured in sea ice models. The evaluation metric is applied to simulations performed with a coupled ocean/sea ice model, where the mechanical behavior of sea ice is represented using the Viscous-Plastic (VP) rheology, as in most current global ocean and climate models. The VP model is shown to be unable to capture the statistical and scaling properties of sea ice deformation. As these properties are a signature of the ice mechanical behavior, it suggests that the VP rheology is inappropriate for sea ice modeling.

The new mechanical model developped during this thesis is based on the hyopthesis that sea ice deformation is mainly accommodated by fracturing and frictional sliding (brittle behavior) over a wide range of scales (stresses can be transmitted on long distances). The main characteristics of this new model, named the Elasto-Brittle (EB) rheology, are progressive damage to represent the brittle behavior, and an elastic constitutive law to allow long-range elastic interactions to take place.

The EB rheology is first used to carry out a fundamental study of fracture in heterogeneous media. Simulations show that fracture is preceded by a divergence of the correlation length, measured from a correlation analysis of discrete events and from a scaling analysis of the continuous strain-rate field. The scaling properties of deformation that emerge in the vicinity of failure ressemble those observed for the brittle deformation of geophysical objects such as sea ice or the earth's crust. These results, that argue for a critical point interpretation of fracture, are discussed in the context of fracture at geophysical scales.

Secondly, short term simulations of the winter Arctic sea ice cover are carried out using the EB rheology. The results show that the EB rheology captures well the statistical and scaling properties of sea ice deformation, motivating the implementation of the EB rheology in global sea ice models. On longer time scales, sea ice can recover its mechanical properties through refreezing of fractures. A healing law accounting for this process is presented along with preliminary results from simulations accounting for the effect of healing. Finally, a methodology for the implementation of the EB rheology within a global sea ice model is presented and discussed.

Keywords : sea ice, rheology, dynamics, fracture, spatial and temporal scaling

Vers un nouveau cadre de modélisation rhéologique de la banquise

Résumé

Fine couche de glace flottant à la surface des océans polaires, la banquise est un objet dynamique qui joue un rôle clé dans le système climatique. Isolant l'océan de l'atmosphère, la banquise contrôle par l'intermédiaire de l'épaisseur de glace et de la fraction d'eau libre les flux d'énergie entre ces deux milieux, et ce de manière fortement non linéaire : dans une banquise dont 0.5% de la surface est constituée de fractures, 50% des flux de chaleur s'effectuent le long de ces fractures. Il apparait donc essentiel de mieux comprendre et modéliser les processus de déformation et de rupture de la banquise.

Dans la première partie de ce travail, le cadre de modélisation mécanique actuellement utilisé dans les modèles de banquise, la rhéologie Visqueuse-Plastique (VP), est évalué sur la base des propriétés statistiques et propriétés d'échelle des vitesses de dérive et de déformation de la banquise. Ces propriétés jouent un rôle important pour les flux de chaleur air-mer et la production de glace, d'autre part elles peuvent être considérées comme une empreinte du comportement mécanique de la banquise. Cette évaluation met en évidence les limitations du cadre de modélisation VP et notamment son incapacité à reproduire les propriétés de déformation de la banquise. Cela suggère que la rhéologie VP n'est pas adaptée à la modélisation de la banquise.

Le nouveau cadre de modélisation mécanique developpé au cours de cette thèse fait l'hypothèse que la déformation de la banquise est principalement accommodée par fracturation et glissement le long de failles (comportement fragile) sur une vaste gamme d'échelles (transmission de contraintes à grande distance). Dans ce nouveau modèle, baptisé la rhéologie Elasto-Fragile (EB), la banquise est considérée comme une plaque solide élastique, permettant les interactions à grande distance, associée à une loi d'endommagement progressive, décrivant un comportement fragile.

Le modèle EB est premièrement utilisé pour mener une étude fondamentale sur la rupture dans les matériaux hétérogènes. Une divergence de la longueur de corrélation est mise en évidence à partir des fonctions de corrélation des évènements d'endommagement ainsi que par l'analyse d'échelle du champ de déformation. Les propriétés d'échelles du champ de déformation qui émergent à l'approche de la rupture sont proche de celles observées pour la déformation fragile des objets géophysiques tel que la banquise ou la croûte terrestre. Ces résultats soutiennent l'analogie entre rupture et point critique.

Une application idéalisée de la rhéologie EB à la banquise Arctique, adaptée à des simulations courtes (3 jours), est présentée. Les propriétés statistiques et propriétés d'échelle obtenues pour la déformation simulée sont comparables à celles obtenues pour la banquise. Ces premiers résultats prometteurs soutiennent que les propriétés de déformation de la banquise émergent du comportement mécanique élasto-fragile de la banquise et motivent l'implémentation de la rhéologie EB dans les modèles globaux de banquise. Sur des périodes de temps plus longues, l'effet du regel des failles et fractures présentent au sein de la banquise doit être pris en compte. Une loi de cicatrisation décrivant ce processus est présentée ainsi que des résultats préliminaires de simulations prenant en compte cet aspect. Finalement, une méthodologie pour l'implémentation de la rhéologie EB dans un modèle global de banquise est présentée.

Mots-clés : glace de mer, banquise, rhéologie, rupture, loi d'échelle spatiale et temporelle

Table des matières

Grenoble, le 4 octobre 2010
Lucas Girard

Chapitre 1

Contexte et motivations scientifiques

1.1 La banquise, une composante du système climatique

Fine couche de glace flottant à la surface des océans polaires, la banquise, ou glace de mer, représente environ deux tiers de la cryosphère terrestre en surface. La banquise est une composante importante du système climatique qui contraint fortement les échanges entre l'océan et l'atmosphère. Sa faible conductivité thermique (Pringle *et al.*, 2007) et son albedo élevé (Perovich *et al.*, 2002; Eicken *et al.*, 2004; Brandt *et al.*, 2005) en font un très bon isolant qui limite le rayonnement solaire absorbé par l'océan et modifie le bilan énergétique de surface. D'autre part, la formation et la fonte de glace de mer entraînent des variations de salinité à la surface de l'océan qui modifient la stratification océanique, jouant un rôle capital dans la circulation océanique aux hautes latitudes, la formation d'eaux denses et, par conséquent, la circulation thermohaline mondiale (McBean *et al.*, 2005; Aagaard & Carmack, 1989).

La grande étendue spatiale (milliers de km) et la faible épaisseur (quelques mètres) de la banquise rendent son évolution sensible aux changement climatiques. Durant les trente dernières années, la banquise Arctique a subi un déclin spectaculaire de son étendue et de son épaisseur. Ce déclin s'accompagne d'une accélération de la vitesse de dérive et de déformation de la banquise. Si le réchauffement global de la planète observé depuis le début de l'ère industrielle a pu amorcer cette évolution, la rapidité du déclin actuellement observé est probablement l'empreinte de l'emballement du système climatique Arctique. Nous verrons dans cette section que cet emballement pourrait s'expliquer par différents processus impliquant une rétroaction positive du recul de la banquise.

1.1.1 Déclin de la banquise Arctique

Depuis la fin des années 1970, des mesures satellitaires basées sur des capteurs de micro-ondes passives permettent d'estimer l'évolution de l'étendue de la banquise (définie comme la surface couverte par au moins 15% de glace de mer). De part sa fine épaisseur, de l'ordre du mètre, cette étendue subit une forte variabilité saisonnière, évoluant d'environ $5 \times 10^6\,\mathrm{km}^2$ (Septembre) à $15 \times 10^6\,\mathrm{km}^2$ (Mars). Les mesures satellitaires montrent qu'une tendance pluri-annuelle à la diminution se surimpose au cycle saisonnier. Cette tendance est particulièrement marquée en été (-9.1% par décennie sur la période 1979-2006 (Stroeve *et al.*, 2007)) et s'accélère au début du XXI^e siècle. Tendance qui est aussi observée en hiver depuis quelques années, atteignant -3% par décennie (Comiso, 2006). En septembre 2007, l'étendue minimale la plus faible depuis le début des mesures satellitaires a été atteinte, $4.3 \times 10^6\,\mathrm{km}^2$, pulvérisant le précédent record établi en 2005 de plus de 20% (Comiso *et al.*, 2008).

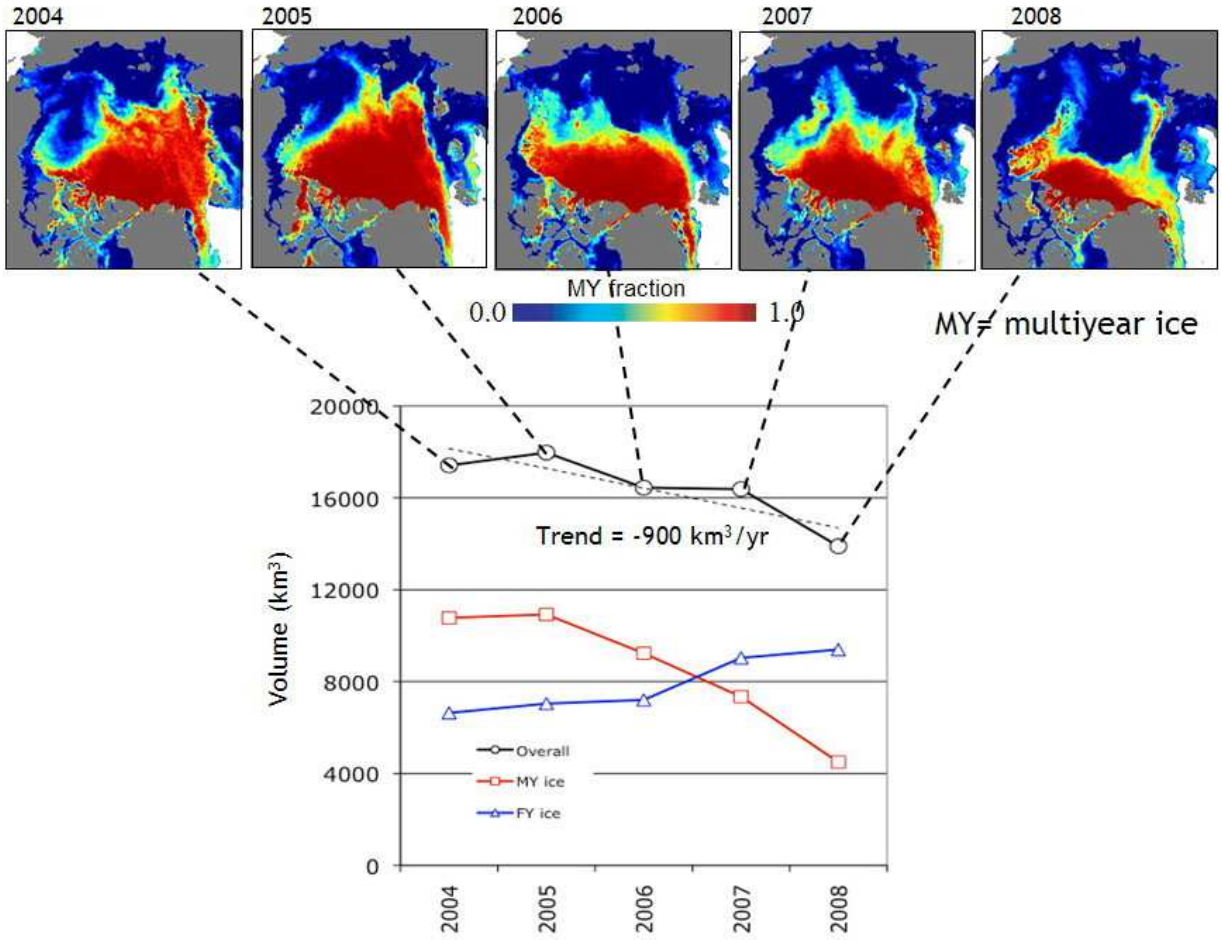

FIG. 1.1: Evolution de l'étendue de la fraction de glace pluri-annuelle et du volume de glace de mer estimés à partir des campagnes ICESat (Kwok *et al.*, 2009). MY fait référence à la glace pluri-annuelle, FY à la glace de l'année.

Il faut néanmoins souligner que ces tendances à la diminution sont extraites de séries temporelles d'observations relativement courtes qui sont affectées par des fluctuations interannuelles importantes. D'autre part, les variations d'étendue de la banquise ne traduisent pas forcément l'évolution du bilan de masse des glaces. En effet, le bassin Arctique étant relativement confiné, la redistribution des épaisseurs de glace par les vents et les courant marins peut modifier de manière significative l'étendue spatiale de la banquise, sans pour autant que son volume soit modifié.

Des mesures d'épaisseur de la banquise ont été obtenues par sonar lors de campagnes sous-marines (Rothrock *et al.*, 2008; Wadhams & Davis, 2000) ou par sondeur électromagnétique (Haas, 2004). Ces mesures montrent une importante réduction de l'épaisseur moyenne (-36% entre 1975 et 2000, (Rothrock *et al.*, 2008)).

Des altimètres laser (ICESat) et radar (ERS) permettent de mesurer le franc-bord de la banquise, c'est à dire la hauteur entre la surface supérieure de la banquise et le niveau de la mer (Kwok & Rothrock, 2009; Laxon *et al.*, 2003). L'épaisseur de glace peut être déduite du franc-bord, mais cela nécessite d'estimer l'épaisseur de neige couvrant la banquise. Cette dernière ne pouvant pas être mesurée directement elle est actuellement modélisée. Les estimations d'épaisseur de banquise obtenues de cette manière confirment une importante perte d'épaisseur qui s'explique principalement par un déclin des glaces pluri-annuelles, c'est à dire des glaces ayant survécu à la fonte durant au moins un été (figure 1.1) (Comiso, 2002, 2005; Kwok *et al.*, 2009). Les mesures d'épaisseur restent à ce jour insuffisantes pour suivre de manière précise le bilan de

masse de la banquise Arctique, néanmoins, toutes les études récentes tendent à conclure qu'une disparition progressive de la banquise pluri-annuelle semble inéluctable (Serreze *et al.*, 2007; Lemke *et al.*, 2007). L'océan Arctique se retrouverait alors libre de glace à la fin de chaque été, avant de retrouver une couverture de glace de mer durant la saison hivernale.

1.1.2 Dérive et déformation

Soumise aux contraintes exercées par le vent et les courants marins, la banquise est mise en mouvement, elle dérive et se déforme. Dans le bassin Arctique, le vent géostrophique explique à lui seul 70% des variations de vitesse de dérive de la banquise (Thorndike & Colony, 1982).

Moyennée à grande échelle spatiale et temporelle, la dérive de la banquise fait apparaitre deux structures principales, la dérive transpolaire, transportant les glaces du large des côtes sibériennes vers le détroit de Fram (situé entre le Groënland et le Spitsberg), d'où elles sont expulsées hors de l'océan Arctique, le long de la côte Est du Groënland. La deuxième grande structure de dérive de la banquise est un gyre situé au large de l'Alaska en mer de Beaufort (figure 1.2). En utilisant une approche inspirée de la turbulence fluide, Rampal *et al.* (2009a) ont montré que le champ de dérive de la banquise Arctique pouvait être décomposé en un champ moyen et des fluctuations. Les échelles appropriées pour définir ce champ moyen de dérive sont de $400\,$km et 5 mois et demi en hiver, $200\,$km et $2\,$mois et demi en été. Le champ de dérive moyen calculé à ces échelles à l'aide des données de bouées dérivantes de l'International Arctic Buoy Program (IABP) montre une forte variabilité inter- et intra-annuelle. La seule structure persistante est la dérive transpolaire. Les fluctuations de vitesse de dérive montrent des propriétés statistiques particulières qui diffèrent de la turbulence fluide, telle qu'observée dans l'atmosphère et dans l'océan. Ces fluctuations ne sont donc pas héritées des forçages dynamiques mais émergent du comportement de la banquise et de sa fracturation.

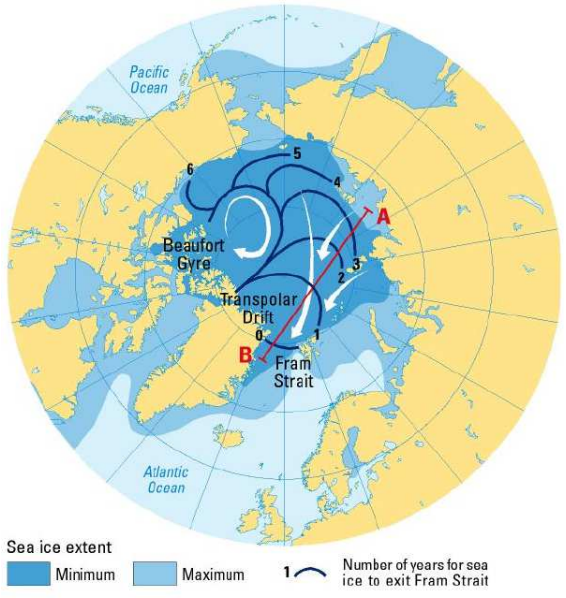

FIG. 1.2: Circulation générale de la banquise Arctique obtenue par moyennisation de trajectoires de bouées dérivantes sur les échelles de temps et d'espace maximales. Les flèches blanches mettent en évidence la dérive transpolaire et le gyre de Beaufort, d'après Pfirman *et al.* (1997).

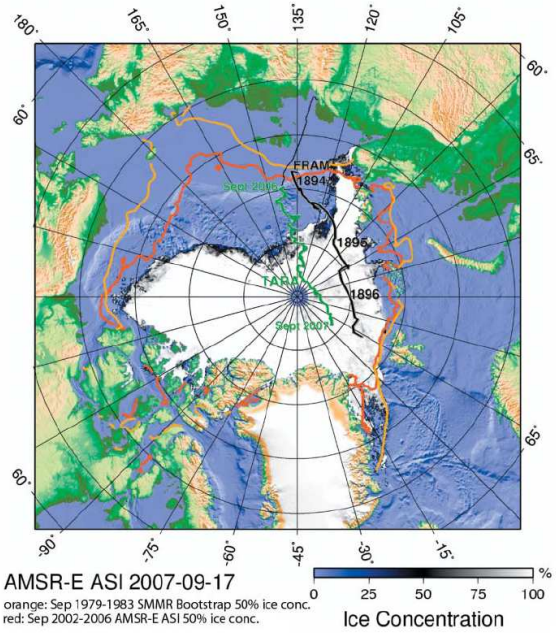

FIG. 1.3: Trajectoires de dérive du voilier Tara (de sept. 2006 à sept. 2007) et du Fram (1894-1896), superposées à la concentration de glace minimale de septembre 2007 estimée à partir de données AMSR-E (Gascard *et al.*, 2008).

En effet, la déformation de la banquise est principalement accommodée par l'ouverture et le glissement le long de chenaux et de fractures (Schulson, 2004; Weiss *et al.*, 2007). Ces fractures contribuent donc à modifier la fraction d'eau libre présente au sein de la banquise, la distribution des épaisseurs et indirectement la dérive de la banquise. La fracturation de la banquise contrôle de manière fortement non linéaire les flux d'énergie entre l'océan et l'atmosphère. A titre d'exemple, en hiver, dans une banquise fracturée à 0.5%, 50% des flux d'énergie entre l'océan et l'atmosphère s'effectuent le long des fractures (Heil & Hibler, 2002).

Les travaux de Rampal *et al.* (2009b), également basés sur l'analyse des données de bouées dérivantes IABP, ont mis en évidence une accélération des vitesses de dérive et de déformation de la banquise. Entre 1979 et 2007, la vitesse moyenne de dérive a ainsi augmentée de 17% par décade en hiver (8.5% en été) et la vitesse de déformation d'environ 50% par décade. Cette accélération a été illustrée en 2007 par l'expédition du voilier Tara, qui, 113 ans après l'aventure du Fram, se laissait prendre dans les glaces au large de la Sibérie, pour y dériver avec le courant transpolaire. La dérive de Tara s'avéra plus de deux fois plus rapide que celle du Fram (figure 1.3) !

Cette intensification de la cinématique n'est pas liée à un changement du forçage atmosphérique mais probablement à l'amincissement de la banquise. En effet, la diminution d'épaisseur de la banquise contribue à réduire sa résistance mécanique, favorisant la fracturation. La banquise peut ainsi se déformer et dériver plus facilement.

1.1.3 Rétroaction positive du recul de la banquise Arctique

La banquise, de part son albédo élevé, ~ 0.9 en présence de neige fraiche, limite l'absorption du rayonnement solaire incident par l'océan. Une diminution d'étendue de la couverture de glace entraîne donc une diminution moyenne de l'albedo de la surface (l'albedo de l'océan étant ~ 0.2) provoquant une augmentation importante du rayonnement solaire incident absorbé. Cela facilite la fonte de la banquise et favorise d'autant plus la diminution de l'étendue des glaces. Il existe donc une boucle de rétroaction positive du système banquise-océan sur la diminution d'étendue de la banquise. Ce mécanisme s'applique également à

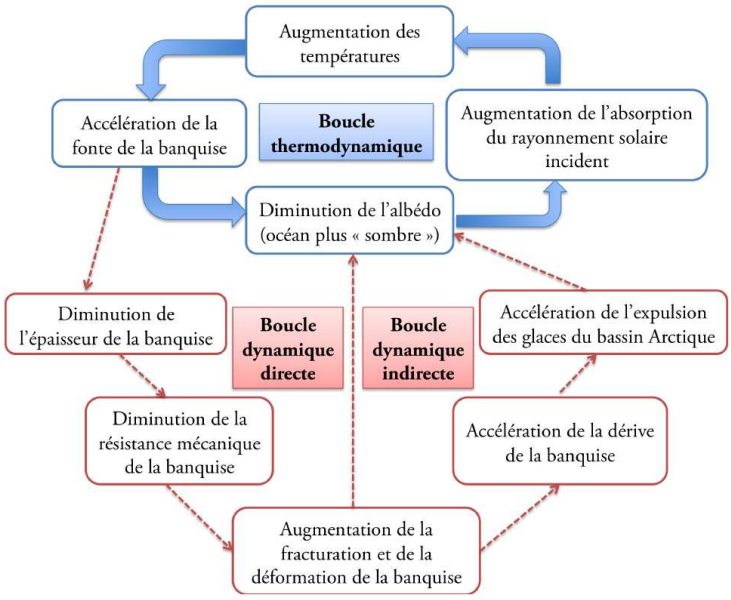

FIG. 1.4: Boucle de rétroaction de l'albedo illustrant les interactions entre les processus thermodynamiques (bleu) et les processus mécaniques (rouge) (Rampal, 2008).

la glace fine, dont l'albedo est moins élevé que celui de la glace épaisse. Une couche de glace fine absorbe donc une plus grande part du rayonnement solaire incident et fond plus rapidement que la glace épaisse. Cette boucle de rétroaction contribue également à réchauffer les couches supérieures de l'océan, retardant le regel de la banquise lors de l'hiver suivant.

Cette rétroaction joue un rôle clé dans l'accélération du déclin de la banquise actuellement observé. Lindsay & Zhang (2005) parlent du passage d'un « point de non retour » dans l'évolution du système banquise-océan. Cette évolution serait lié à un préconditionnement : hausse graduelle des températures sur les 50 dernières années entraînant une diminution moyenne de l'épaisseur des glaces formées durant l'hiver, ainsi qu'à un déclencheur : un régime de vent estival favorisant l'export des glaces anciennes et épaisses, et finalement la rétroaction positive décrite précédemment. La notion de « point de non retour » vient du fait que l'évolution du système ne semble plus dominée par les forçages externes mais par des changements thermodynamiques internes (rétroaction positive de l'albédo) impliquant la notion d'irréversibilité.

D'autre part, l'évolution de la dynamique de la banquise renforce cette rétroaction positive du déclin de la banquise. En effet, la diminution de l'épaisseur moyenne des glaces contribue à diminuer leur résistance mécanique et à favoriser leur fracturation. Une banquise plus fracturée entraîne une diminution de l'albedo moyen de surface, rejoignant la boucle de rétroaction thermodynamique décrite ci-dessus. D'autre part, l'intensification de la fracturation de la banquise facilite l'accélération de la dérive et éventuellement de l'export des glaces hors du bassin Arctique, principalement par le détroit de Fram, situé entre le Groënland et le Spitsberg (figure 1.4) (Rampal *et al.*, 2009b).

1.2 Comportement mécanique de la banquise

De part son rapport d'aspect très élevé, étendue / épaisseur $\sim 10^6$, la banquise peut être considérée comme un plaque solide bidimensionelle. Soumise aux efforts exercés principalement par les vents et les courant marins (Thorndike & Colony, 1982), cette plaque se déforme et se fracture. La déformation de la banquise, l'ouverture de fractures et de cheneaux d'eau libre, contribuent à modifier la fraction d'eau libre, la répartition des épaisseurs, jouant un rôle considérable dans le bilan de masse des glaces et le bilan d'énergie de surface de l'océan Arctique par le biais des processus et des rétroactions décrites précédemment.

Du point de vue mécanique, la banquise peut être considérée, sous certains aspects, comme un analogue de la croûte terrestre (Weiss *et al.*, 2009) ; différents arguments justifiant cette analogie seront présentés dans cette section. La cinématique de la banquise est bien plus intense que celle de la croûte terrestre, les vitesses de déformation étant de l'ordre de $\sim 10^8$ fois plus élevées. D'importants jeux de données permettant de caractériser le comportement mécanique de la banquise ont ainsi pu être obtenus en quelques années grâce à cette cinématique intense. Ces données ont permis d'une part d'analyser les contraintes internes à la banquise, les propriétés de rupture et d'ouverture de failles, d'autre part de caractériser les propriétés statistiques de la déformation. L'un de ces principaux jeux de données est le RADARSAT Geophysical Processor System (RGPS). Le RGPS effectue le suivi lagrangien de points de la banquise à partir d'images satellites SAR successives, permettant de calculer le champ de déformation sur une vaste gamme de résolutions spatiales, allant de 10 km à 1000 km, soit l'échelle du bassin Arctique (Fily & Rothrock, 1990; Kwok, 1998b). Une revue complète des résultats présentés dans cette section et de l'analogie banquise-croûte terrestre est donnée par Weiss & Schulson (2009).

1.2.1 Rupture cisaillante et friction

Rupture de Coulomb

Les images satellites de la banquise mettent en évidence l'existence de failles, de fractures et de chenaux d'eau libre (figure 1.5). Ceux-ci peuvent s'étendre sur plusieurs centaines de kilomètres en longueur. Différents auteurs ont noté la présence de chenaux conjugués, avec des angles d'intersections variant entre $20°$ et $50°$ (Marko & Thomson, 1977; Erlingsson, 1988), similaires aux failles conjuguées observées pour la croûte terrestre (Anderson, 1905). Ces simples observations suggèrent que le mécanisme de rupture de Coulomb joue un rôle important dans la déformation de la banquise (Schulson, 2004).

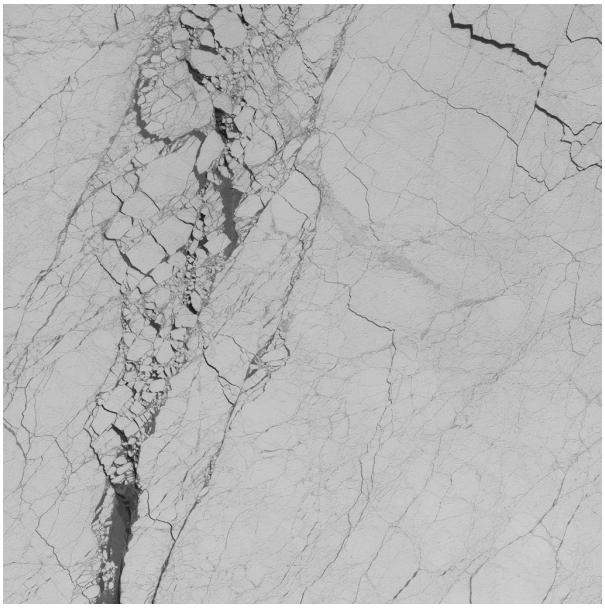

FIG. 1.5: Image satellite SPOT de la banquise sur l'océan arctique ($80°11'$N, $103°33'$W), avril 1996. L'image représente une zone de 60 km de large.

Proposé il y a plus de 200 ans pour décrire la rupture par cisaillement des roches (Coulomb, 1773), le critère de Coulomb reste un concept pertinent pour décrire l'enveloppe de rupture de nombreux matériaux fragiles tel que les roches et la glace (Weiss & Schulson, 2009). Ce critère suggère que la contrainte cisaillante τ nécessaire pour atteindre la rupture doit

dépasser une cohésion τ_0 et une résistance liée à la friction donnée par le produit d'une constante μ et de la contrainte normale σ_n :

$$|\tau| = \tau_0 + \mu\sigma_n, \tag{1.1}$$

σ_n et τ étant définies en fonction des contraintes principales σ_1 et σ_2 par les relations suivantes :

$$\sigma_n = \frac{1}{2}(\sigma_1 + \sigma_2), \qquad \tau = \frac{1}{2}(\sigma_1 - \sigma_2). \tag{1.2}$$

Le critère de Coulomb peut en fait s'appliquer à deux problèmes :

- La rupture d'un matériau initialement intact par formation de failles cisaillantes
- Le glissement le long d'une faille cisaillante existante

Dans le premier cas, μ est appelé le coefficient de friction interne et $\phi = \tan^{-1}(\mu)$ est l'angle de friction interne, alors que dans le second cas, μ représente le coefficient de glissement par friction. En d'autres termes, lorsque la rupture a lieu, la contrainte de Coulomb $|\tau| - \mu\sigma_n$ dépasse la cohésion τ_0 dans le plan considéré. Pour un matériau isotrope, l'orientation θ du plan de faille dans l'espace des contraintes principales qui maximise la contrainte de Coulomb est donnée par :

$$\tan(2\theta) = \frac{1}{\mu} \tag{1.3}$$

Des valeurs de θ ont ainsi été estimées pour la banquise à partir d'images satellites mais l'incertitude, la variabilité de ces estimations et la forte sensibilité de μ par rapport à θ rendent difficiles toute comparaison avec des valeurs du coefficient de friction mesurées en laboratoire sur des échantillons (Schulson, 2004).

Les champs de déformation obtenus à l'aide du RGPS montrent des zones linéaires de forte déformation, désignées comme « Linear Kinematic Features » (LKF) dans la littérature (Kwok, 2001). Les LKF sont des zones qui concentrent la déformation cisaillante mais également la déformation divergente. Cela soutient l'hypothèse suivant laquelle la déformation est accomodée par rupture cisaillante accompagnée de dilatance.

La rupture de Coulomb a lieu lorsque la vitesse d'accumulation de contrainte dépasse la vitesse de relaxation de contrainte par fluage. Pour un précurseur constitué d'une fracture d'origine thermique, de 100m de long, Schulson (2004) a estimé que la transition ductile-fragile avait lieu à un taux de déformation d'environ 10^{-8}s^{-1}. Les taux de déformations obtenues par RGPS à l'échelle de $10\,$km et $\sim 3\,$jours dépassent presque tous ce seuil (Marsan *et al.*, 2004). A ces échelles, le taux de déformation moyen est de $3 \times 10^{-7}\text{s}^{-1}$, mais cette valeur augmente lorsque les échelles spatiales et temporelles d'observation diminuent, comme expliqué dans le paragraphe 1.2.2. Cela confirme que les conditions de rupture de Coulomb sont réunies dans le cas de la banquise.

Enveloppe de rupture

Des mesures de contraintes *in-situ* ont été effectuées durant la campagne SHEBA, en mer de Beaufort, à l'aide d'un réseau de capteurs (Richter-Menge *et al.*, 2002; Weiss *et al.*, 2007). La figure 1.6 présente les contraintes principales enregistrées par l'un de ces capteurs entre octobre 1997 et juillet 1998, avec fréquence d'enregistrement horaire. Les états de contraintes observés sont contenus dans une enveloppe de Coulomb. La valeur $\mu = 0.7$ estimée avec les données de la figure 1.6 est similaire à celle obtenue par Schulson *et al.* (2006a) pour l'enveloppe de rupture d'échantillons de glace de mer soumis à des essais biaxiaux de laboratoire à $-10°$C.

Le coefficient de friction semble donc être une propriété mécanique invariante d'échelle. Par contre, la valeur de cohésion τ_0 déduite de la figure 1.6 est plus petite que la valeur correspondante déterminée en laboratoire, d'un facteur 15 à 30 (Weiss *et al.*, 2007). En d'autres termes, l'enveloppe de Coulomb des mesures

SHEBA est une version contractée de l'enveloppe obtenue à partir d'essais en laboratoire. Cela suggère la présence de concentrateurs de contrainte (défauts) plus grands sur le terrain qu'en laboratoire.

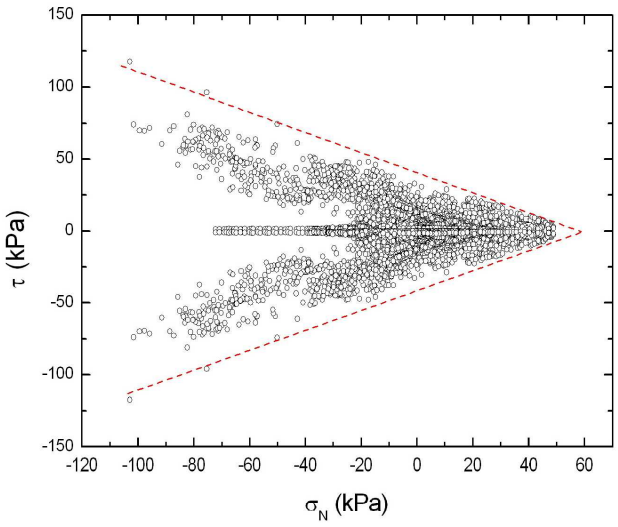

FIG. 1.6: Etats de contraintes enregistrés par le capteur « Baltimore » durant la campagne de mesures SHEBA (10/1997 - 06/1998). La ligne pointillée représente l'enveloppe de Coulomb $|\tau| = \tau_0 + \mu\sigma_n$, avec $|\tau_0| = 40\,\text{kPa}$ et $\mu = 0.7$ (Weiss *et al.*, 2007).

En mécanique de la rupture, il existe une relation entre l'échelle associée à une fracture et la contrainte nécessaire pour l'activer $\sigma \sim l^{-1/2}$: plus l'échelle l est grande, plus la contrainte nécessaire est petite. Cette relation permet de comparer la valeur $\sigma_c = 250\,\text{kPa}$ obtenue avec les mesures SHEBA (figure 1.6) et celle obtenue à partir d'essais de compression uniaxiale en laboratoire, $\sigma_c \simeq 5\,\text{MPa}$ (Schulson *et al.*, 2006a). Si l'on estime une échelle pour le concentrateur de contrainte de l'ordre de grandeur de la taille de grain, soit de quelques millimètres à quelques centimètres, on obtient une échelle de concentrateur de l'ordre du mètre sur le terrain. Cette estimation semble plausible puisqu'elle correspond environ à l'épaisseur de la banquise. Ces précurseurs à la rupture pourraient être générés par de la rupture thermique. Les états de contrainte d'origine thermique (cisaillement nul, divergence ou convergence uniquement) sont d'ailleurs visibles sur la figure 1.6, sur la droite d'équation $\tau = 0$ (Weiss *et al.*, 2007).

1.2.2 Hétérogéneité et intermittence de la déformation

Dans le paragraphe précédent, nous avons mis en évidence le comportement fragile et l'importance du mécanisme de rupture de Coulomb pour la banquise. Ces propriétés caractérisent également le comportement mécanique de la croûte terrestre. La rupture de Coulomb est un mécanisme multi-échelle : il s'applique sur une vaste gamme d'échelle avec une physique similaire, il est caractérisé par une physique invariante d'échelle. C'est un mécanisme à seuil, qui entraîne une redistribution des contraintes élastiques et, dans les matériaux hétérogènes, conduit à une fracturation multi-échelle. Le champ de déformation résultant de ces processus est hétérogène (traduit la localisation spatiale), intermittent (notion d'amassement temporel) (Cowie *et al.*, 1995; Sornette *et al.*, 1990) et multi-fractal (Marsan *et al.*, 2004). La physique sous-jacente à la déformation de la banquise et la déformation de la croûte sont, de ce point de vue, similaires.

Dans le cas de la banquise Arctique, l'hétérogéneité et l'intermittence de la déformation a pu être mise en évidence grâce aux jeux de données satellitaire RGPS et de bouées dérivantes IABP. En effet, le taux de déformation moyen est caractérisé par des lois d'échelles spatiale et temporelle (Marsan *et al.*, 2004; Rampal *et al.*, 2008). La loi d'échelle spatiale du taux de déformation $\dot{\epsilon}$ est donnée par :

$$\dot{\epsilon}(R) \sim R^{-\beta} \tag{1.4}$$

où l'exposant β caractérise le degré d'hétérogéneité de la déformation, R étant l'échelle spatiale. Un champ de déformation homogène correspond à la valeur $\beta = 0$, comme dans le cas d'un écoulement visqueux, tandis qu'une localisation extrême de la déformation, sur une seule faille, entraînerait la valeur $\beta = d$, d

étant la dimension topologique, soit $d = 2$ pour la banquise. De la même manière, la loi d'échelle temporelle est donnée par :

$$\dot{\epsilon}(t) \sim t^{-\alpha} \tag{1.5}$$

où α caractérise l'intermittence du processus de déformation, t étant l'échelle de temps. La valeur $\alpha = 0$ correspond à une déformation sans aucune intermittence, par exemple de type visqueuse, tandis que $\alpha = 1$ correspond à une déformation accomodée par un seul évenement.

La cinématique de la croûte terrestre ne permet pas une analyse directe des champ de déformation. Néanmoins, des relations comparables ont été établies pour la déformation de la croûte terrestre, caractérisant l'amassement spatial des hypocentres de seismes (Kagan & Knopoff, 1980; Kagan, 1991) et leur intermittence (Kagan & Jackson, 1991).

Les observations ont montré que les valeurs des exposants caractérisant l'hétérogénéité et l'intermittence ne sont pas universelles. Pour la banquise, β décroit lorsque l'échelle de temp t augmente mais n'atteint jamais la valeur limite $\beta = 0$ même pour des échelles de l'ordre de plusieurs mois (figure 1.7). Cela signifie que la déformation de la banquise devient plus homogène lorsque l'on augmente l'échelle de temps considérée, mais elle garde tout de même un certain degré d'hétérogénéité à ces grandes échelles de temps. De la même manière, α décroit lorsque l'échelle spatiale R est augmentée mais n'atteint jamais la valeur limite $\alpha = 0$, même pour une échelle spatiale de $300\,\text{km}$ (figure 1.7). Cela signifie que l'intermittence de la déformation décroit lorsque l'échelle spatiale augmente mais qu'elle persiste à des échelles comparables à la taille du bassin Arctique (Rampal *et al.*, 2008). La dépendance de l'exposant β par rapport à t et de l'exposant α par rapport à R met en évidence un couplage spatio-temporel qui caractérise la déformation fragile des objets géophysiques (Weiss *et al.*, 2009).

Comme nous le verrons dans la section 1.3, le cadre de modélisation mécanique actuellement utilisé dans la plupart des modèles globaux de banquise est basé sur la rhéologie Visqueuse-Plastique (VP). Les résultats que nous venons de présenter montrent que, même aux grandes échelles spatiales et temporelles, la banquise n'a pas un comportement visqueux-plastique. Ils suggèrent donc que la rhéologie VP n'est pas appropriée à décrire le comportement mécanique de la banquise.

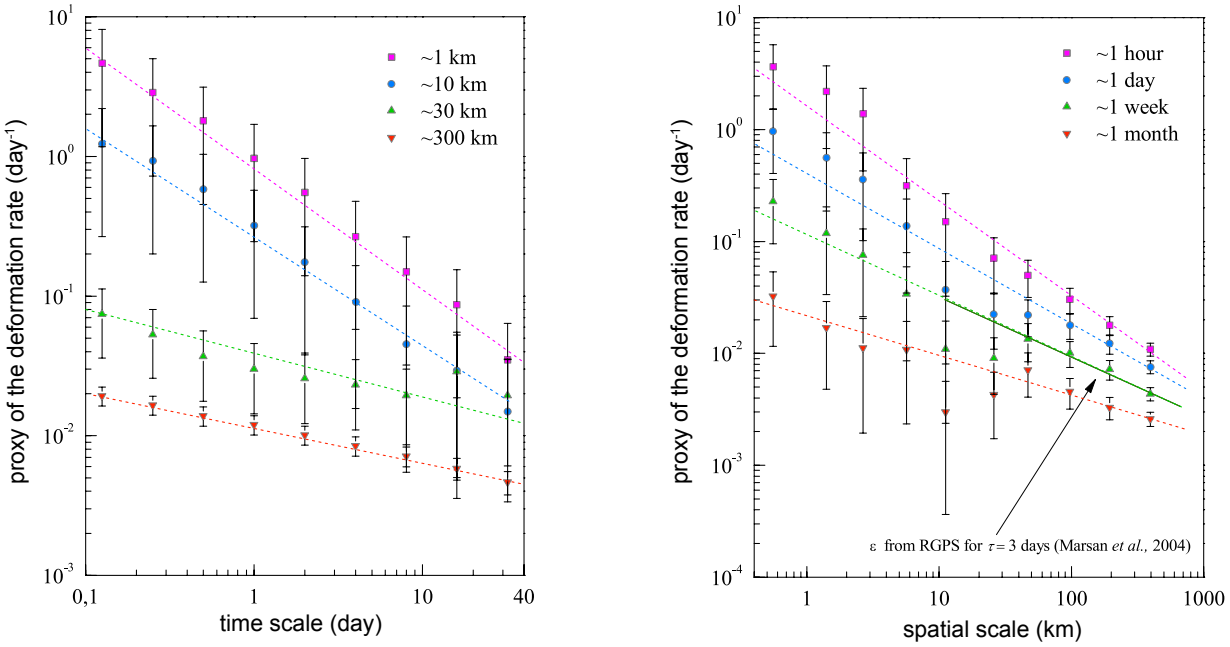

FIG. 1.7: Loi d'échelle temporelle (gauche) et spatiale (droite) du taux de déformation de la banquise arctique mettant en évidence le couplage spatio-temporel de la déformation (Rampal *et al.*, 2008).

1.3 Modélisation de la banquise

Comme décrit dans la section 1.1, la banquise joue un rôle clé dans le climat polaire et influence également le climat global par de nombreux processus. Pour ces raisons, les modèles de climat intègrent tous une représentation sophistiquée de la banquise. Dans cette section, nous passons en revue les aspects dynamiques et mécaniques. Dans la plupart de ces modèles, le comportement mécanique de la glace est décrit par la rhéologie Visqueuse-Plastique (VP). La présentation de cette rhéologie mettra en lumière des différences fondamentales avec le comportement mécanique décrit précédemment à partir d'observations. Ces différences, qui amènent à questionner la pertinence de la rhéologie VP, sont à la base de ce travail de thèse.

Feltham (2008) offre une revue complète de la modélisation rhéologique de la banquise, dans le cadre de la mécanique des milieux continus. D'autre part, des résultats intéressants ont également été obtenus avec des modèles anisotropes (Schreyer *et al.*, 2006; Wilchinsky & Feltham, 2004, 2006a), des modèles discrets (Hopkins & Thorndike, 2006) et granulaires (Tremblay & Mysak, 1997), mais le couplage de ce type de modèle à des modèles d'océan ou de climat est complexe et encore trop couteux en temps de calcul à l'heure actuelle.

1.3.1 Principales composantes des modèles

Le cadre de modélisation que nous présentons considère la banquise comme un milieu continu. Les bases de ce cadre de modélisation ont été jetées par Coon *et al.* (1974) dans le modèle de banquise AIDJEX (Arctic Ice Dynamics Joint Experiment). Ces auteurs considèrent que la banquise se déplace dans un plan bidimensionnel et ils font l'hypothèse que, pour une échelle spatiale de discrétisation bien plus importante que la taille des *floes* (fragment de banquise), la vitesse de la banquise peut être définie par un champ continu et dérivable $\mathbf{u}(\mathbf{x}) = (u,\ v)$, où $\mathbf{x}$ est la position horizontale sur la surface.

Les modèles de banquise sont principalement constitués d'une composante thermodynamique, qui calcule le transport de chaleur par conduction verticale à travers la glace, la formation et la fonte de glace, ainsi que d'une composante dynamique qui détermine les mouvements horizontaux de la banquise. La thermodynamique et la dynamique de la banquise dépendent toutes les deux de l'épaisseur de glace. Dans l'objectif de pouvoir représenter les processus dépendants de l'épaisseur de glace, la plupart des modèles utilisent une fonction de distribution des épaisseurs, « Ice Thickness Distribution » (ITD) en anglais, décrite par Thorndike *et al.* (1975) :

$$\frac{\partial g}{\partial t} = -\nabla.(\mathbf{u}g) - \frac{\partial}{\partial h}(fg) + \psi \tag{1.6}$$

où h est l'épaisseur de glace, $g(h,\ \mathbf{x},\ t)$ est la densité de probabilité de l'épaisseur, f est la variation d'épaisseur liée à la thermodynamique (gel/fonte). Le premier terme du membre droit de l'équation décrit le transport horizontal, le second terme décrit le transport dans l'espace des épaisseurs h lié à la thermodynamique et le dernier terme, la fonction ψ, décrit la redistribution mécanique des épaisseurs dans ce même espace. Les processus que cette fonction représente sont complexes : lorsque la dynamique banquise est convergente, la glace fine peut se déformer pour former de la glace plus épaisse, sous forme de crêtes de compression, à l'inverse, lorsque la dynamique est divergente, des zones d'eau libre se forment au sein du *pack* de banquise (chenaux d'eau libre ou polynies). La fonction ψ est donc mal contrainte et définie de manière empirique dans les modèles, suivant les travaux de Thorndike *et al.* (1975).

La vitesse $\mathbf{u}$ est calculée à partir de l'équation de la dynamique, qui considère les différentes forces agissant sur un *floe* ainsi qu'un terme lié aux interactions entre les *floes* :

$$\frac{D(m\mathbf{u})}{Dt} = -mf_c\mathbf{k} \times \mathbf{u} + \tau_a + \tau_w - m\hat{g}\nabla\eta + \nabla.\sigma \tag{1.7}$$

Tous les termes sont exprimés en unité de force par unité de surface et t est le temps. La somme des forces du membre de droite est composée, de gauche à droite, de la force de Coriolis, de la tension exercée par le vent sur la glace, la tension exercée par l'océan, la force liée à la pente de l'océan ainsi que la force liée aux contraintes internes de la banquise, donnée par la divergence du tenseur des contraintes de la banquise, σ. Le tenseur des contraintes considéré est l'intégrale du tenseur de Cauchy sur l'épaisseur de la glace auquel le terme de contrainte isostatique $1/2\rho_{ice}h^2\hat{g}\delta_{ij}$ a été soustrait (où ρ_{ice} est la densité de la banquise, $\hat{g}$ est l'accélération gravitationnelle et h l'épaisseur de banquise). Une loi rhéologique est nécessaire pour calculer le tenseur des contraintes (paragraphe 1.3.2). Dans l'equation 1.7, D/Dt est la dérivée matérielle, $\mathbf{k}$ est un vecteur normal à la surface de la banquise dirigé vers l'atmosphère, f_c est le paramètre de Coriolis, m est la masse de glace par unité de surface et η est la hauteur dynamique de l'océan. La masse de glace est déterminée par intégration de l'ITD :

$$m = \rho_{ice} \int_0^\infty g(h) h \, \mathrm{d}h. \tag{1.8}$$

1.3.2 Du modèle AIDJEX à la rhéologie Visqueuse-Plastique (VP)

Par rhéologie de la banquise, nous entendons la relation entre le tenseur des contraintes internes de la banquise σ, le champ de vitesse de déformation $\dot{\epsilon}$, les propriétés physiques de la banquise et son état : distribution des épaisseurs, concentration (définie comme la fraction relative de glace pour une surface donnée). Si la rhéologie VP s'est concrétisée dans le modèle d'Hibler (1979), elle s'appuie fortement sur l'approche élastique-plastique du modèle AIDJEX (Coon *et al.*, 1974).

AIDJEX : la rhéologie élastique-plastique

L'hypothèse ayant motivé le choix d'un modèle plastique est basée sur le raisonnement suivant. La réponse de la banquise aux variations relativement lisses des champs de forçage atmosphérique et océanique est constituée d'évènements locaux (formation de crêtes de compression, de chenaux d'eau libre), dont l'occurrence est ponctuelle et irréversible, comme si une contrainte seuil était atteinte. D'autre part, des arguments théoriques suggèrent que, si l'on fait l'hypothèse que la forme des crêtes de compressions est indépendante du taux de déformation auquel elles se sont formées, le travail fournit pour former ces crêtes est également indépendant du taux de déformation (Parmerter & Coon, 1973; Rothrock, 1975). Un dernier arguement est lié à l'analogie visuelle qui peut être faite entre la banquise et des matériaux granulaires tels que les sols, dont le comportement a pu être représenté par des modèles plastiques (Schofield & Wroth, 1968).

Lorsque les états de contrainte n'engendrent pas de déformation plastique, le comportement de la glace est défini comme élastique dans le modèle AIDJEX. Ce choix s'explique premièrement par le fait qu'un modèle purement plastique ne permette pas d'application numérique. D'autre part, Coon *et al.* (1974) justifient ce choix sur le plan physique par le fait qu'un état de contrainte, même inférieur au seuil de déformation plastique, entraîne une déformation, si petite soit elle.

La banquise est considérée comme isotrope dans le modèle AIDJEX, ce qui permet d'exprimer la surface de seuil plastique par une courbe dans le plan des contraintes principales σ_1 et σ_2 ou, de manière équivalente, en fonction de la contrainte normale σ_n et de la contrainte cisaillante τ (eq. 1.2). Le critère de plasticité s'écrit alors,

$$F(\sigma_n, \tau; s_i) = 0 \tag{1.9}$$

où F est la fonction définissant la courbe de seuil et s_i est un scalaire lié aux propriétés de la banquise. Pour un matériau isotrope, la courbe de seuil est symétrique par rapport à la droite d'équation $\tau = 0$. Lorsque

l'état de contrainte de la banquise atteint la courbe de seuil, il est admis que la direction de la déformation plastique suit la loi d'écoulement normale :

$$\dot{\epsilon}_k^p = \lambda \frac{\partial F}{\partial k}\Big|_{F=0} \quad k = \sigma_n, \tau, \tag{1.10}$$

où $\dot{\epsilon}_k^p$ est la vitesse de déformation plastique et λ est un scalaire positif inconnu. L'équation 1.10 est une loi d'écoulement standard en plasticité, qui définit la direction de la déformation : suivant la normale extérieure à la courbe de seuil, mais dont l'amplitude est indéterminée. C'est la résolution de l'équation de la dynamique qui permet, a posteriori en quelque sorte, de déterminer l'amplitude de la déformation.

Presque tous les modèles de banquise utilisent aujourd'hui cette loi d'écoulement qui s'avère être invalidée par l'expérience. En effet, des essais mécaniques sur des échantillons de glace de mer montrent que la direction de déformation n'est pas normale à l'enveloppe de rupture (Weiss *et al.*, 2007). Dans le cas réel, la déformation permanente est accommodée par l'ouverture de fractures, elle n'est donc pas isochore, ce qui contredit une hypothèse principale de la plasticité et explique le fait que la loi d'écoulement normale ne soit pas vérifiée.

La rhéologie VP

La rhéologie visqueuse-plastique (Hibler, 1979) est basée sur le modèle isotrope, plastique de Coon *et al.* (1974) mais le comportement élastique est remplacé par un comportement visqueux. Cela permet de contourner une difficulté importante rencontrée lors de l'implémentation numérique du modèle AIDJEX, le comportement élastique nécessitant de garder en mémoire l'évolution d'une configuration de décharge pour pouvoir calculer la déformation, ou de travailler en formulation lagrangienne.

Lorsque les états de contrainte n'atteignent pas l'enveloppe plastique, le comportement de la banquise est donc défini comme visqueux dans la rhéologie VP. Ce choix semble principalement motivé par des raisons numériques, mais des arguements physiques ont également été avancés pour le justifier (Hibler, 1977). La différence essentielle avec la rhéologie élastique-plastique réside dans la manière dont est traitée la glace soumise à de faibles mouvements. Dans le cas élastique-plastique, une contrainte élevée est maintenue sans aucun mouvement relatif, tandis qu'avec la rhéologie VP, ces états engendrent un fluage lent. En utilisant des viscosités suffisamment grandes, le taux de déformation reste faible, voir négligeable tant que l'enveloppe plastique n'est pas atteinte. Le comportement visqueux et le comportement plastique peuvent être

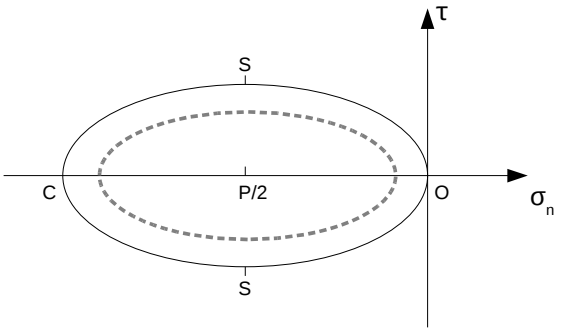

FIG. 1.8: Enveloppe de seuil plastique de la rhéologie VP. Pour un état de contrainte appartenant à l'enveloppe, la déformation est plastique (courbe continue), les états de contraintes en compression, cisaillement et traction sont représentés respectivement par C,S et O. Pour de petits taux de déformations, les états de contraintes se trouvent à l'intérieur de l'éllipse (courbe pointillée) et la déformation est visqueuse.

représentés par l'équation suivante :

$$\sigma_{ij} = 2\eta\dot{\epsilon}_{ij} + [\zeta - \eta]\,\dot{\epsilon}_{ij}\delta_{ij} - P\delta_{ij}/2, \tag{1.11}$$

où P est un terme de pression. Hibler (1979) choisit des viscosités dépendantes de $\dot{\epsilon}_{ij}$ et de P : $\zeta(\dot{\epsilon}_{ij}; P)$ et $\eta(\dot{\epsilon}_{ij}; P)$, de manière à ce que pour des taux de déformation *typiques*, les états de contraintes se situent sur la courbe de seuil plastique et la loi d'écoulement s'applique. Cela signifie que le seuil de déformation plastique est mal contraint et qu'il est donc défini de manière relativement arbitraire. La courbe de seuil plastique est définie dans le plan (σ_n, τ) par une ellipse passant par l'origine (figure 1.8). La forme générale de cette courbe correspond qualitativement au comportement mécanique de la banquise : une résistance maximale en compression, intermédiaire en cisaillement et faible en traction. Le fait que la courbe passe par l'origine (aucune résistance à la traction pure) est par contre, contredit par l'expérience puisqu'en réalité des états de contraintes en traction sont bien observés pour la banquise (Weiss *et al.*, 2007) (voir figure 1.6). La forme elliptique a été choisie par commodité, permettant d'exprimer les viscosités de la manière suivante :

$$\zeta = \frac{P}{2\Delta}, \qquad \eta = \frac{\zeta}{e^2}, \tag{1.12}$$

où

$$\Delta = \left[(\dot{\epsilon}_{11}^2 + \dot{\epsilon}_{22}^2)(1 + e^{-2}) + 4e^{-2}\dot{\epsilon}_{12}^2 + 2\dot{\epsilon}_{11}\dot{\epsilon}_{22}(1 - e^{-2})\right]^{1/2}, \tag{1.13}$$

et e est l'excentricité de l'ellipse de la courbe de seuil plastique. Hibler définit des valeurs maximales pour ζ et η, dépendantes de P, qui sont atteintes aux faibles taux de déformation. Dans ce cas, les états de contraintes se trouvent sur une ellipse concentrique à la courbe de seuil (figure 1.8). En pratique, les valeurs limites de ζ et η sont choisies suffisamment grandes pour qu'elles n'influencent pas de manière significative le calcul des mouvements de la banquise. La rhéologie VP est complétée d'une équation décrivant le terme de pression P aussi appelé résistance de la glace :

$$P = P^* h \exp\left[-C(1 - A)\right], \tag{1.14}$$

où P^* et C sont des constantes empiriques. Pour des concentration de glace A élevées, P dépend principalement de l'épaisseur h, tandis que lorsque A diminue, la résistance P décroit rapidement. Une telle paramétrisation de la résistance de la glace semble plausible mais la justification de la forme de cette paramétrisation est douteuse. En particulier la valeur de la constante P^* est régulièrement adaptée, dans une fourchette de valeurs allant de 10^4 à $10^5\,\mathrm{Nm}^{-1}$, pour obtenir des simulations correspondant mieux aux observations.

Hunke & Dukowicz (1997) ont implémenté une variante élastique-visqueuse-plastique (EVP) de la rhéologie VP. Il ne s'agit pas d'une nouvelle rhéologie mais simplement d'une modification de la méthode numérique de résolution. Un terme élastique est artificiellement introduit dans l'équation constitutive ce qui permet de calculer les contraintes de manière explicite, tandis que la rhéologie VP initiale nécessite un calcul implicite.

1.3.3 Utilisation de la rhéologie VP

L'absence de base physique de la rhéologie VP a été mentionnée dès son avènement par Nye (1973). Néanmoins, son efficacité numérique et la facilité de couplage avec un modèle d'océan qu'elle offre ont démocratisé son utilisation. Les modèles de banquise basés sur la rhéologie VP sont maintenant utilisés à différentes fins :

- Dans des modèles globaux de climat (GCM), où ils sont couplés à des modèles de circulation océanique et atmosphérique. C'est le cas de la plupart des simulations menées pour le quatrième rapport du

GIEC (Groupe d'experts Intergouvernemental sur l'Evolution du Climat) (Lemke *et al.*, 2007), avec une résolution spatiale de l'ordre de 100 km.

- Dans des modèles de circulation océanique, tel que NEMO (Nucleus for European Modelling of the Ocean) (Fichefet & Morales-Maqueda, 1997), à des résolutions spatiales de l'ordre de 10 km, voir 2 km pour certaines études récentes (Wang & Wang, 2009).

Le recul de la banquise observé durant la dernière décennie dépasse largement toutes les projections envisagées par les GCM, en terme d'étendue spatiale (Stroeve *et al.*, 2007), d'épaisseur et d'accélération de la dérive (Rampal & Weiss, 2010). Ce constat soulève plusieurs questions qui ont motivé ce travail de thèse :

- Dans quelle mesure la dynamique simulée par la rhéologie VP est-elle représentative de la dérive et de la déformation de la banquise ?
- Comment les observations de dérive et de déformation peuvent-elles être utilisées pour évaluer la dynamique simulée par les modèles ?

Les mécanismes permettant l'émergence des propriétés multifractales du champ de déformation de la banquise sont, (i) un mécanisme à seuil qui entraîne une redistribution des contraintes élastiques (le mécanisme de rupture de Coulomb), ainsi que (ii) des interactions élastiques à grande distance (section 1.2). Dans le cadre de modélisation VP, les variations de la résistance mécanique P de la glace peuvent entraîner une redistribution des contraintes : admettons qu'une cellule du modèle subisse une diminution de la contentration de glace A (représentant l'ouverture de fractures ou de chenaux d'eau libre), cela entraînera une baisse de la résistance mécanique P. L'enveloppe plastique pourra ainsi être atteinte plus facilement et la déformation sera ainsi accrue (figure 1.9). Par le biais de l'équation de la dynamique, une partie de la glace de cette cellule, pourra être advectée vers les cellules voisines, dont la résistance mécanique est renforcée. Ce mécanisme représente donc une redistribution des contraintes mais il diffère du mécanisme observé pour la banquise puisque son effet est local et limité aux cellules voisines. Cela met en évidence l'absence dans la rhéologie VP (le même raisonnement peut être appliqué au modèle AIDJEX) d'un mécanisme essentiel à l'émergence des propriétés de déformation de la banquise : les interactions élastiques à grande distance.

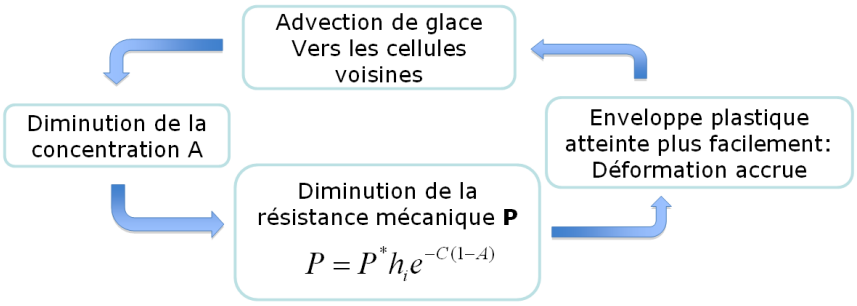

FIG. 1.9: Boucle de rétroaction mécanique pour la rhéologie VP. La paramétrisation de P permet une redistribution des contraintes locale mais pas d'interactions à grande distance.

1.4 Objectifs et organisation du mémoire

Ce chapitre d'introduction a mis en lumière la forte implication de la banquise et de sa dynamique dans le système climatique. En effet, la banquise, en isolant l'océan de l'atmosphère, contrôle par l'intermédiaire de l'épaisseur de glace et de la fraction d'eau libre, les flux d'énergie entre ces deux milieux, et ce de manière fortement non linéaire, d'où la nécessité de mieux comprendre et modéliser les processus de déformation et de fracturation associés. Les modèles de climat actuels intègrent tous une représentation relativement sophistiquée de la banquise, dans laquelle le comportement mécanique est décrit par la rhéologie VP. Toutefois, l'analyse de contraintes in-situ et des propriétés de la déformation de la banquise remet en cause ce cadre de modélisation. En effet, plusieurs études récentes montrent que la déformation de la banquise résulte principalement d'un processus de fracturation multi-échelles, qui ne peut pas être représenté par un comportement visqueux-plastique, même aux grandes échelles de temps et d'espace.

Dans la première partie de ce travail de thèse nous avons donc cherché à évaluer le cadre de modélisation actuel et à mettre en évidence les limites de la rhéologie VP. Pour ce faire, nous avons mis en oeuvre des outils statistiques pour comparer la dérive et la déformation simulées aux principaux jeux de données d'observations de la dynamique de la banquise (Chapitre 2). Les résultats de cette première étude ont confirmé la nécessité d'initier une modélisation du comportement mécanique de la banquise sur une base physique totalement différente. L'analogie entre la banquise et la croûte terrestre a guidé le développement de ce nouveau cadre de modélisation. Des modèles élasto-fragiles utilisant l'endommagement progressif ont été utilisés pour représenter les propriétés d'échelle de la déformation de la croûte et des roches (Cowie *et al.*, 1995; Amitrano *et al.*, 1999). Nous avons donc choisi d'utiliser une base similaire pour représenter le comportement mécanique de la banquise. Le développement de ce nouveau cadre de modélisation s'est fait en trois temps :

- L'analyse statistique des résultats d'un modèle élasto-fragile, dans le cadre d'un mode de chargement simple en compression uniaxiale. Au delà de l'étude de la banquise, ce travail est une contribution théorique à l'étude de la rupture. Le formalisme des transitions de phase est utilisé pour caractériser l'approche à la rupture d'un point de vue sismique (énergie dissipée) et du point de vue des champs de déformation (Chapitre 3).

- L'application du modèle élasto-fragile à la banquise Arctique en prenant en compte le forçage engendré par le vent, mais sans regel ni advection (Chapitre 4).

- L'implémentation d'une loi de cicatrisation dans le modèle élasto-fragile, qui décrit la restauration des propriétés mécaniques lors du regel. Pour cela, nous définissons un modèle physique de cicatrisation ainsi qu'une méthodologie pour le mettre en oeuvre, qui passe par la prise en compte de déformations permanentes. L'architecture complète de la rhéologie élasto-fragile pour la banquise est présentée dans le chapitre 5.

Un dernier chapitre sera consacré à la discussion des résultats obtenus ainsi qu'aux perspectives qu'ils ouvrent en termes de modélisation de la banquise ainsi que l'étude fondamentale de la rupture et de la déformation des objets géophysiques.

Chapitre 2

Evaluation des modèles rhéologiques de banquise sur une base statistique

D'après :

Girard, L., J. Weiss, J. M. Molines, B. Barnier, and S. Bouillon (2009), Evaluation of high-resolution sea ice models on the basis of statistical and scaling properties of Arctic sea ice drift and deformation, *J. Geophys. Res.*, *114*, C08015, doi :10.1029/2008JC005182.

Abstract

Sea ice drift and deformation from models are evaluated on the basis of statistical and scaling properties. These properties are derived from two observation datasets : the RADARSAT Geophysical Processor System (RGPS) and buoy trajectories from the International Arctic Buoy Program (IABP). Two simulations obtained with the Louvain-la-Neuve Ice Model (LIM) coupled to a high resolution ocean model and a simulation obtained with the Los Alamos Sea Ice Model (CICE) were analyzed. Model ice drift compares well with observations in terms of large scale velocity field and distributions of velocity fluctuations although a significant bias on the mean ice speed is noted.

On the other hand, the statistical properties of ice deformation are not well simulated by the models : (i) The distributions of strain-rates are incorrect : RGPS distributions of strain-rates are power law tailed, i.e. exhibit 'wild randomness', whereas models distributions remain in the Gaussian attraction basin, i.e. exhibit 'mild randomness'. (ii) The models are unable to reproduce the spatial and temporal correlations of the deformation fields : In the observations, ice deformation follows spatial and temporal scaling laws that express the heterogeneity and the intermittency of deformation. These relations do not appear in simulated ice deformation. Mean deformation in models is almost scale independant. The statistical properties of ice deformation are a signature of the ice mechanical behavior. The present work therefore suggests that the mechanical framework currently used by models is inappropriate. A different modeling framework based on elastic interactions could improve the representation of the statistical and scaling properties of ice deformation.

2.1 Introduction

The sea ice cover is a dynamic body, moving under the action of winds and ocean currents. The deformation rates of sea ice, determined from the spatial gradients in the velocity field, are associated with internal stresses, which, when large enough, generate an ubiquitous network of fractures and leads.

Fractures in the ice cover decrease the albedo and allow more shortwave absorption by the ocean, thereby shrinking the ice cover during summer, thus reducing its strength and possibly increasing the fracturing (Moritz *et al.*, 2002; Zhang *et al.*, 2000; Rampal *et al.*, 2009b). On the other hand, fracturing during winter enhances the thermodynamically driven production of new ice and modifies the heat and salinity budget in the Arctic (Maykut, 1982). In all seasons, an increase of sea ice fracturing and fragmentation facilitates sea ice drift and its export towards lower latitudes (Rampal *et al.*, 2009b). Accurate modelling of the ice velocities and deformation rates is therefore essential in order to get a good representation of the open water fraction, the thickness distribution, and the global sea ice mass balance in climate models.

Recent analysis of drifting buoy trajectories and fine scale sea ice kinematics produced by the RADARSAT Geophysical Processor System (RGPS) (Kwok, 1998b) expressed the heterogeneous and intermittent character of sea ice deformation by spatial and temporal scaling laws (Marsan *et al.*, 2004; Rampal *et al.*, 2008). Investigation of internal sea ice stresses and RGPS-derived strain-rates revealed the elasto-brittle behavior of the ice cover (Weiss *et al.*, 2007) : most of sea ice deformation is accommodated by active fractures and faults at various scales. This can explain the intermittency and spatial heterogeneity of sea ice deformation (Weiss *et al.*, 2009) but raises an important question : To what extent can current sea ice models simulate such a multiscale fracturing process ?

Indeed, current models stem from the work of Hibler (1979) who described the ice cover in terms of viscous-plastic (VP) mechanics and accordingly invoked the concept of a rate- and scale-independent failure envelope. This modeling framework is based on a fluid-mechanics approach which seems at odd with a scenario where sea ice deformation is accommodated by multiscale fracturing processes.

Thomas (1999) performed a comparison of model deformation fields and buoy-derived deformation estimates at large scale (400 to 600km). He found modest correlation for vorticity and shear, but the correlations of divergence were insignificant. More recently, RGPS derived strain-rates allowed a closer investigation of sea ice deformation on a wide range of spatial scales. Lindsay *et al.* (2003) and Kwok *et al.* (2008) used this new dataset to examine model deformation rates from regional (~ 300km) to small spatial scales (10km). These two studies showed that even though models are capable of reproducing the large-scale drift patterns, the simulated deformation rates show rather poor correlation with RGPS observations, especially at small scales. Moreover there is a high variability among models on these aspects.

Although a high correlation between model and observation estimates of strain-rates is desirable, it could be searched in vain. Indeed, sea ice velocity fluctuations have a stochastic component, implying that the spatial gradients of the velocity field also behave in a non deterministic manner. Using drifting buoy trajectories, Rampal *et al.* (2009a) developed a methodology based on an analogy to fluid turbulence in order to determine the spatial and temporal averaging scales at which the velocity field can be partitioned into a mean component (i.e. the predictable part of velocity), and its respective fluctuations (i.e. the stochastic component). Considering the stability of the Lagrangian statistics, these authors established that the appropriate averaging scales to define the mean velocity field are 400km spatially and 160days temporally (in winter). The stochasticity of strain-rates becomes dominant at scales below a few hundred km. With the grid size of models reaching $\sim 10km$ nowadays, it appears crucial to take this aspect into account when

investigating the performance of models in terms of ice drift and deformation.

These points have motivated an additional investigation of model ice drift and deformation using statistical comparisons with observations. In this paper, we examine probability distribution functions (PDF) of model strain-rates at different scales and analyze the dependence of strain-rates upon spatial and temporal scales. For this purpose, we use the methodologies developed by Marsan *et al.* (2004) and Rampal *et al.* (2008) to analyze buoy as well as RGPS data. This adds to the work of Lindsay *et al.* (2003) who underlined the necessity to evaluate the distribution functions of strain-rates in models, in particular divergence, which influences most the ice production estimates.

We have analyzed two simulations performed with the Louvain-La-Neuve Ice Model (LIM), coupled to a high resolution global ocean model. A third simulation obtained with the The Los Alamos sea ice model (CICE) was also examined. As this last simulation was obtained with a very different configuration, only a few features concerning ice deformation are presented. The fine grid size of these simulations (~ 12km for LIM and ~ 9km for CICE) allows the investigation of the scaling properties over a large scale range and is of the same order of magnitude as the scale of RGPS observations (~ 10km).

This paper is organized as follows. The statistical properties of sea ice deformation on which our evaluation is based are summarized in section 2.2, along with the observation datasets they concern. Section 2.3 briefly describes the models. In section 2.4 model ice drift is evaluated, while model strain-rates are considered in section 2.5. The results are discussed in section 2.6 and the conclusions are given in section 2.7.

2.2 Statistical and scaling properties of sea ice deformation : spatial heterogeneity and intermittency

It is qualitatively known from the journey of Fridtjof Nansen on the Fram along the transpolar drift, at the end of the 19^{th} century, that sea ice dynamics is characterized by tortuous drifting trajectories and intermittency, with a wide range of ice velocities and accelerations. As shown below, spatial heterogeneity and intermittency are the two main characteristics of sea ice deformation.

The fine-scale sea ice kinematics produced by RGPS have allowed the investigation of sea ice motion and deformation over an unprecedented range of spatial scales, from 10km to the scale of the Arctic Ocean as a whole (~ 1000km). RGPS is based on a cross-correlation technique applied to consecutive SAR images (Fily & Rothrock, 1990), which allows tracking in a Lagrangian fashion of more than 40000 points over the Canadian side of the Arctic during an entire season. Data from 9 winters (1997-2008) are now available (http ://www-radar.jpl.nasa.gov/rgps/), a database that has no counterpart in geophysics.

The tracked points define the corners of cells which are initially squared $(10 \times 10\text{km}^2)$. The velocities of the cell corners are computed over the period between two observations (sampled at irregular time intervals within the domain, but typically 3 days). The strain-rate tensor components $\partial u/\partial x$, $\partial v/\partial x$, $\partial u/\partial y$, $\partial v/\partial y$ are computed from an approximation of the line integral around the boundary of each of the cells (Kwok, 1998b). The 3 invariants of the strain-rate tensor, respectively divergence, shear and vorticity, are defined as follows :

$$\dot{\epsilon}_{div} = \frac{\partial u}{\partial x} + \frac{\partial v}{\partial y} \tag{2.1}$$

$$\dot{\epsilon}_{shear} = \left[\left(\frac{\partial u}{\partial x} - \frac{\partial v}{\partial y} \right)^2 + \left(\frac{\partial u}{\partial y} + \frac{\partial v}{\partial x} \right)^2 \right]^{1/2} \tag{2.2}$$

$$\dot{\epsilon}_{vor} = \frac{\partial v}{\partial x} - \frac{\partial u}{\partial y} \tag{2.3}$$

The tracking errors (~ 100m) give rise to error standard deviations of 0.5% day^{-1} in the divergence, shear, and vorticity (Lindsay & Stern, 2003).

This dataset revealed highly heterogeneous strain patterns with most of the deformations localized along so-called linear kinematics features (LKF) separating quasi-rigid plates (Kwok, 2001; Moritz & Stern, 2001). However, this distinction is somewhat arbitrary as it relies on a chosen threshold, and is scale-dependent. Marsan *et al.* (2004) performed a multifractal analysis of sea ice deformation from the RGPS database. For a 3-day interval centred around November, 5^{th}, 1997, they computed the scaling of the moments $< \dot{\epsilon}_{tot}^{q} >$, where the so-called total strain-rate is defined as : $\dot{\epsilon}_{tot} = \sqrt{\dot{\epsilon}_{div}^2 + \dot{\epsilon}_{shear}^2}$. Note that this scalar quantity $\dot{\epsilon}_{tot}$ contains information about the intensity of the strain-rate, whereas the information about the principal directions is lost. This procedure can be repeated over boxes of different sizes, from the size of the initial RGPS cell $(10$km$)$ to sizes close to the Arctic basin scale (~ 1000km). A power law decrease of the average strain-rate $< \dot{\epsilon}_{tot} >$ with increasing scale L was observed, $< \dot{\epsilon}_{tot} > \sim L^{-0.20}$. This is a signature of long-range spatial correlations present in the strain-rate field, as a random spatial reshuffling of the strain-rate values suppresses power law scaling (Marsan *et al.*, 2004). A strong curvature of the experimental moment function $b(q)$, i.e. $< \dot{\epsilon}_{tot}^{q} > \sim L^{-b(q)}$ where $b(q)$ is a non-linear function of order q, was also reported, indicating multifractality of the strain-rate. This multifractality expresses the scaling properties of sea ice deformation, and particularly the absence of characteristic scale between 10 and 1000km, and show how the strain-rate distribution evolves with the spatial scale considered. Consequently, determining threshold strain-rate values to define LKFs is a scale-dependent procedure. In addition, the multifractality of the strain-rate fields indicates that mean values carry limited information, due to the existence of extreme fluctuations, and actually depend on the spatial scale considered.

The proportion (or density) of open water within the winter ice cover also exhibits a multifractal scaling behavior (Weiss & Marsan, 2004). This similarity of the scaling properties of the strain-rate field and the open water concentration is not a coincidence : it expresses the intimate link between fracturing and deformation at all scales and suggests that brittle deformation is essential in sea ice mechanics. Sea ice concentration is thus related to the deformation field, and has been shown to be one of the most important factors influencing the surface energy budget (Sorteberg *et al.*, 2007; Lüpkes *et al.*, 2008). It appears therefore crucial to obtain a correct representation of the multifractal and scaling properties of sea ice deformation in climate models.

The main limitation of RGPS is a time resolution of about 3 days that does not allow to explore the temporal scaling in details. For this purpose, the dispersion of buoys trajectories is an alternative. The idea to estimate sea ice deformation from buoys dispersion was first applied by Thorndike (1986), then used recently by Rampal *et al.* (2008) to analyze systematically the spatial and temporal scaling of sea ice deformation, from few hours to few months, and from few hundred meters to several hundred kilometers. A set of about 500 trajectories of drifting buoys were obtained from the International Arctic Buoy Program (IABP, http ://iabp.apl.washington.edu/), deployed in the Arctic from 1979 until now. These buoys are fixed on the ice and drift according to the ice motion. Positions are obtained from GPS receivers or Argos transmitters with a position uncertainty of the order of $100m$ and $300m$, respectively (Thorndike & Colony, 1982; Heil & Hibler, 2002). Like molecules in a gas or a turbulent fluid, nearby pieces of sea ice gradually move apart as the result of deformation (Martin & Thorndike, 1985). In the case of fluid turbulence, it is customary to characterize this dispersion by the mean square change in separation r of pairs of fluid particles, $< \Delta r^2 >$. In the case of the Arctic sea ice cover, it seems more appropriate to express this dispersion in terms of a deformation rate, using the standard deviation :

$$\dot{\epsilon}_{disp} = \langle \left(\frac{\Delta r}{\tau \times L} - \langle \frac{\Delta r}{\tau \times L} \rangle \right)^2 \rangle^{1/2} \tag{2.4}$$

where L is the (initial) separation of the pair and the average is calculated over N pairs of buoys initially separated by $L \pm \delta L$ and over a time interval $\tau \pm \delta\tau$. A detailed explanation for the use of the standard deviation in the dispersion rate $\dot{\epsilon}_{disp}$, instead of the mean, is given in Rampal *et al.* (2008). These authors applied such a methodology to the IABP dataset in order to analyze the scaling properties of sea ice deformation.

With this definition, $\dot{\epsilon}_{disp}$ only depends on deformation, i.e. not on solid rotation. However, the full strain-rate tensor cannot be determined from pairs of trajectories, i.e. shear and divergence cannot be discriminated on this basis. Rampal *et al.* (2008) also demonstrated that $\dot{\epsilon}_{disp}$ is proportional to $\dot{\epsilon}_{tot}$, with a proportionality factor of about 4. Using appropriate binning of this dataset, the authors obtained the temporal and spatial scalings of the strain-rate $\dot{\epsilon}_{disp}$. The temporal scaling is characterized by :

$$\dot{\epsilon}_{disp} \sim \tau^{-\alpha(L)} \tag{2.5}$$

where the power law exponent $\alpha(L)$ decreases with increasing spatial scale (initial separation), from $\alpha = 0.89$ for $L \approx 1$km to $\alpha = 0.30$ for $L \approx 300$km in winter (respectively 0.87 and 0.25 for summer). Relation (2.5) expresses the intermittency of the process. Indeed, a non-intermittent viscous flow would be characterized by $\alpha = 0$, whereas the boundary value $\alpha = 1$ would correspond to a deformation accommodated by an isolated event, corresponding to the activation of a single fracture or fault. Although the intermittent character, i.e. α, decreases towards large spatial scales as the result of averaging an increasing number of these events, sea ice deformation does not mimic viscous flow even at scales close to the Arctic basin scale.

On the other hand, the following spatial scaling is obtained :

$$\dot{\epsilon}_{disp} \sim L^{-\beta(\tau)} \tag{2.6}$$

where the exponent $\beta(\tau)$ decreases with increasing time scale, from $\beta = 0.85$ for $\tau \approx 1$ hour to $\beta = 0.35$ for $\tau \approx 1$ month in winter (respectively 0.85 and 0.42 for summer). In this case, β expresses the degree of heterogeneity of sea ice deformation, bounded by $\beta = 2$ for a deformation localized along a single fracture, and by $\beta = 0$ for a homogeneous deformation field (e.g. elastic or viscous). Sea ice deformation appears more homogeneous as one increases the time scale and therefore the number of deformation events, but a significant heterogeneity remains even at the scale of months, in agreement with the persistence of active structures over a season (Coon *et al.*, 2007). The spatial scaling obtained from RGPS (see above) is in agreement with these results, although the dependence of β upon time scale was not explored with RGPS.

Relations (2.5) and (2.6) therefore express the strongly intermittent and heterogeneous character of sea ice deformation, as well as the complex space-time coupling illustrated by the dependence of α on L and β on τ. They are essential features of sea ice deformation and dynamics upon which sea ice models performance can be evaluated.

2.3 Models description

2.3.1 Common framework for ice dynamics

Most sea ice codes implemented in climate models are based on a continuum mechanics modeling framework following Hibler (1979), and share a common viscous-plastic (VP) rheology, assuming that sea ice has strength under convergence and shearing, but offers little or no resistance to divergence. In the original VP rheology, the momentum equation is solved implicitly over the whole ice pack. This rheology implies that for stress states inside the plastic yield curve the mechanical behavior is that of a viscous fluid, while the ice flows as a perfect plastic when the stress state reaches the yield curve.

Hunke & Dukowicz (1997) developed a new method (Elastic-Viscous-Plastic, EVP) to solve the momentum equation explicitly, by introducing a non-physical elastic term in the equation. This elastic term can be seen as a regularization of the singularity caused by small strain-rates. Beyond this solving procedure, the mechanical framework remains very similar in VP and EVP solution techniques.

The lack of physical basis of the VP/EVP framework has been underlined in the literature (Nye, 1973; Weiss *et al.*, 2007) but thanks to its numerical efficiency and suitability for coupling with ocean-atmosphere models, this framework has been widely used and is, nowadays, implemented in nearly all global coupled ocean-sea ice models.

2.3.2 LIM Simulations

LIM was used as part of the global coupled ocean model DRAKKAR (Barnier *et al.*, 2006). The configuration we used was developed for studying the evolution of the ocean variability under realistic atmospheric conditions over the last half century (1958-2004). It is based on ERA40 (until 2002), operational ECMWF analysis (after 2002), and satellite products, as detailed in Brodeau *et al.* (2008). The effective spatial grid size of the configuration is about 12km in the Arctic.

LIM is a dynamic-thermodynamic sea ice model designed for climate studies (Fichefet & Morales-Maqueda, 1997). The model dynamics are based on the two-category (consolidated ice and leads) approach of Hibler (1979), it employs the VP dynamics, but EVP dynamics was also recently implemented (Bouillon *et al.*, 2009). The rheology uses an elliptical yield curve and an ice strengh parameter $P^* = 10000Nm^{-2}$.

We present results from two simulations, using VP and EVP dynamics, with similar configurations, changing only the solution technique for ice dynamics. The simulations are referred to as LIMVP and LIMEVP. From these two simulations, 12-hourly fields of model ice drift have been analyzed from a three month winter period (January to March 1997).

For the VP simulation, different values of the creep limit parameter have been tested but this did not affect significantly the statistical and scaling properties of ice deformation. The creep limit parameter corresponding to the results presented below is $\Delta_{min} = 2 \times 10^{-8} s^{-1}$. The LIMVP hindcasts compare well with observations in terms of ice extent and concentration (Drakkar-Group, 2007).

The LIMEVP simulation was obtained as follows : (i) The model was initialized on the LIMVP simulation result on the 1-January 1995, (ii) the model ran 1995 and 1996 with EVP dynamics, as 2 years of transition, and finally the 3-month period (January-March 1997) was extracted for this study. Not surprisingly, the EVP simulation shows very similar results in terms of ice extent, thickness and concentration, but because of the growing number of coupled model using this formulation, we included this second simulation in our analysis.

2.3.3 CICE Simulation

CICE was developed by Hunke & Lipscomb (2001) for climate studies and differs from the original Hibler model in several aspects. It uses EVP dynamics, has five thickness categories and an ice thickness remapping scheme (Lipscomb, 2001) that transfers the ice between categories as it grows and melts. The grid size is 9km. The ice strength is calculated through a ridging scheme initially presented by Rothrock (1975). The ice was coupled to a simple ocean mixed layer that can absorb heat and grow ice in leads. More details about the configuration are given in Maslowski & Lipscomb (2003).

While this simulation is different from the LIM simulations, we believe it is interesting to examine sea ice deformation produced by CICE as it includes several features that could improve the representation of ice dynamics : multiple ice categories and a parameterisation of ice strength through a ridging scheme. Moreover, Maslowski & Lipscomb (2003) indicated that this simulation shows qualitatively more realistic ice strain fields, compared to other models, with stronger localisation of deformation.

The simulation years do not match the availability of RGPS observations. We used daily simulation data from January-March 1987, considered as representative of typical winter ice drift. As no direct comparaison is possible, we restricted our analysis to a few salient features of sea ice deformation.

2.3.4 Common projection and study area

All model scalar and vector fields were projected onto a common Cartesian coordinate system centered on the North Pole (polar stereographic projection), with the vertical axis following the Greenwich meridian.

Coastal regions are known to be of special character in terms of sea ice dynamics : boundary conditions and coastal geometry play an important role, the transition zone between fast ice and pack ice is characterized by particularly large sea ice strain-rates, making the tracking of sea ice deformation in these regions difficult. Consequently, we limited our analysis to the central Arctic basin, north of Bering and Fram straits and 150km away from the coastlines. In model simulations, the ice concentration over the considered region was always greater than 80% during the period analyzed.

2.4 Ice drift

This section compares ice drift from LIM simulations to observations at different scales. We first examine how the large scale ice drift is represented in the simulations. We then consider probability distribution function (PDF) of ice velocity fluctuations.

2.4.1 Mean velocity field

Before examining fluctuations and spatial gradients of ice drift, it is useful to check how well the mean velocity field is represented in the simulations.

Observations from the Special Sensor Microwave Imager (SSMI) passive-microwave satellite sensor can be used to estimate 2-daily ice velocity from cross-correlation between two images. SSMI ice motion data set was provided by the JPL Remote Sensing Group (Kwok, 1998a). The SSMI data are gridded and have better spatial coverage than the buoy data, which motivates their use to evaluate the model mean velocity field. The error standard deviation of velocity estimates is about 8 times larger than for the buoys : $0.058ms^{-1}$ vs. $0.007ms^{-1}$ (Thorndike & Colony, 1980; Kwok, 1998a).

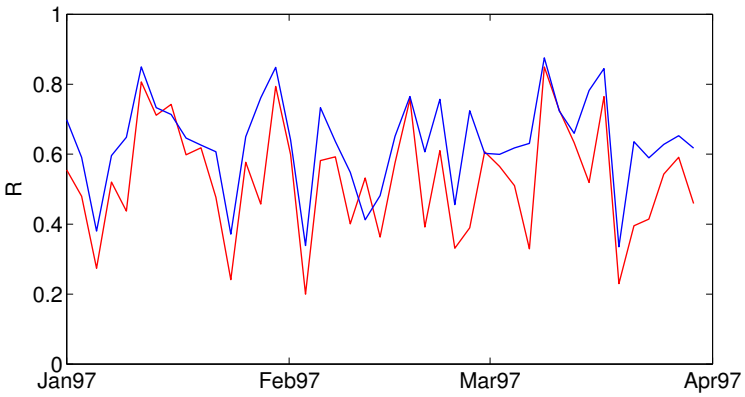

FIG. 2.1: Time series of correlation coefficient R for model (LIMVP in red, LIMEVP in blue) against SSMI velocity field (2 day average, 83km grid). R is calculated for vectors as complex numbers.

Two comparisons are performed, the first one is at the scales of SSMI observations (2-daily and 83km), while the second one concerns the whole 3-month period at the spatial scale of 400km. According to the work of Rampal *et al.* (2009a), the mean velocity at the scales of this second comparison corresponds to the predictible component of the velocity field.

For the first comparison, model ice velocities are resampled to fit SSMI data spatially and temporally (linear interpolation to 83km and 2-daily averaging), considering that SSMI estimates of ice velocity can be taken as point values at this scale. The correlation coefficient R is calculated for each pair of 2 day-velocity fields, considering vectors as complex numbers (Figure 2.1). R shows a high variability, shifting between 0.8 and 0.2. The global correlation, calculated from all velocity values, is slightly higher for LIMEVP ($R_{global} = 0.70$) than LIMVP ($R_{global} = 0.57$).

The second comparison is performed by binning the model and SSMI ice velocities on a 400km grid to average it spatially, and temporally, to 3 months. At these scales, the correlation increases to $R = 0.83$ for LIMVP and $R = 0.82$ for LIMEVP (figure 2.2).

Both comparisons show a significant bias on the speed (table 2.1). This bias is of the same order of magnitude in both simulations and does not vary significantly with scales, it also appears on figure 2.2. The ice thickness appears well represented, with a 2.2m mean thickness over the arctic with largest thicknesses along the Canadian Archipelago. Ice thickness is therefore not the cause of this speed bias. The velocity direction also shows a bias, which reduces at large scales. Tuning of parameters such as the wind drag

	83 km, 2 days			400 km, 3 months		
	SSMI	LIMVP	LIMEVP	SSMI	LIMVP	LIMEVP
$mean\ speed$	4.3	7.8	6.9	1.3	3.3	3.0
$std(speed)$	3.6	4.7	4.3	0.7	1.4	1.1
$\langle \Delta\theta \rangle$		47	32		24	23
R_{global}		0.57	0.70		0.83	0.82
N		650	650		28	28

TAB. 2.1: Model and SSMI ice drift statistics. Mean speed (km/day) and standard deviation of the speed, mean angle difference between the model and SSMI drift vectors $\langle \Delta\theta \rangle$ (degrees) and global correlation coefficient between model and SSMI velocity drift vectors considered as complex numbers R_{global}. N is the number of points used for correlations.

coefficient could perhaps help reducing these biases, but it is not in the scope of this study.

The oscillation of the correlation values at small scale (83km, 2days) suggests that the model does not capture all spatial and temporal variability of the ice velocity field. At such scales, the motion of ice is dominated by stochastic fluctuations and is therefore not predictable in a deterministic sense. At 400km and 3months, a significant correlation is obtained, suggesting that the model captures well the mean ice circulation.

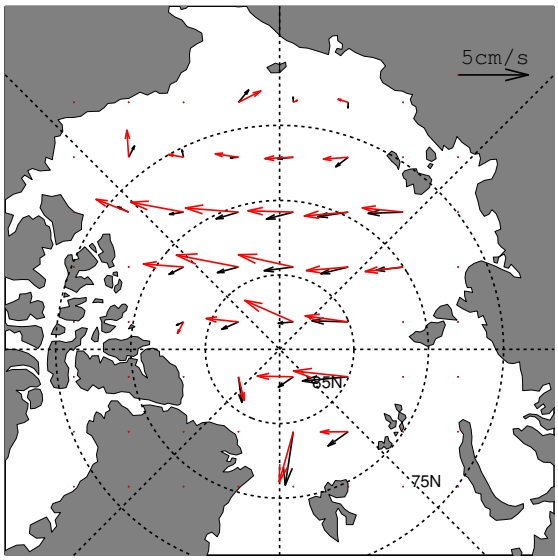

FIG. 2.2: Mean ice velocity field for January-March 1997 at 400km scale, from the LIMVP simulation (red) and SSMI observations (black)

2.4.2 Velocity fluctuations

We consider the ice velocity as the sum of two components, an average ice drift and fluctuations. We calculate ice velocity fluctuations by subtracting the 400km and 3months average ice drift from ice velocity. Fluctuations of ice velocity result from short term wind forcing, but also from the ice mechanical behavior, through the internal ice stress term of the equation of motion, which is calculated by the rheology.

With a high temporal sampling of ice velocity (up to 3h), drifting buoys provide the best observations to examine ice velocity fluctuations. Buoy measurements are of lagrangian type while model ice drift is eulerian. In order to make the comparison with buoy observations possible, model Eulerian ice velocity fields were used to reconstruct Lagrangian trajectories. Synthetic trajectories were initialized at each model grid point and obtained from a linear interpolation of the 12-hourly eulerian velocity fields, using the four nearest neighbors. We do not use an interpolation scheme of higher order to avoid an artificial smoothing of these trajectories. Examples of such reconstructed trajectories are shown on figure 2.3. Model velocity fluctuations are then calculated by subtracting the average model ice drift interpolated along the trajectories from the ice velocity. Buoy velocity fluctuations are calculated similarly by subtraction of the average buoy drift from the velocities. The two standardized components (u' and v') of the model fluctuating velocity vector are represented through their PDFs (figure 2.4), along with buoy measurements of velocity fluctuations performed between January and March from 1979 to 2001. All years of buoy measurements are considered to obtain a sufficient amount of data for the comparison, and the PDF obtained is assumed to be representative of a typical January-March period. We checked

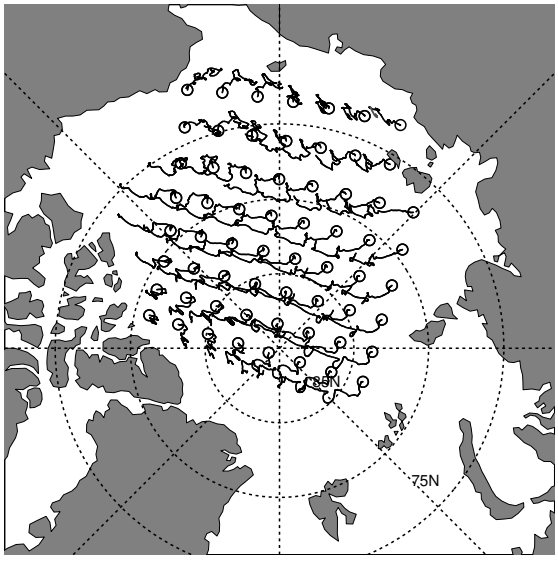

FIG. 2.3: Example of reconstructed Lagrangian trajectories from Eulerian model outputs from January to March 1997. Circles indicate the initial grid points.

the validity of this assumption by plotting PDFs of buoy velocity fluctuations from specific years, and did not find any significant deviation from the data presented on figure 2.4.

Distributions presented on figure 2.4 are standardized in order to focus the comparison on their shape. As for fluid turbulence, the shape of the PDF of velocity fluctuations, rather than its absolute standard deviation, is expected to characterize the underlying physical processes (see e.g. (Frisch, 1995) for turbulence and Rampal *et al.* (2009a) for sea ice).

The distributions of velocity fluctuations show similar shapes, suggesting that the model reproduces correctly the velocity fluctuations over the 3 months analyzed in this study, although the model slightly underestimates the tails of the PDF, i.e. the largest (relative) velocity values beyond 3 to 4 standard deviations. Both model and buoy distributions deviate from the Gaussian distribution in the tails.

In order to investigate time correlations of velocity fluctuations, the mean temporal autocorrelation function of velocity fluctuations $C(\tau)$ was calculated for the reconstructed trajectories. $C(\tau)$ decreases with increasing time lag τ as particles loose the memory of their previous displacements and crosses zero in a finite time. A measure of how fast $C(\tau)$ decreases to zero is defined by the integral time scale Γ, obtained by integrating $C(\tau)$ up to the first zero crossing (e.g. (Zhang *et al.*, 2001)). The integral time scale obtained is 2.9days in both simulations, whereas the same calculation with drifting buoy trajectories leads to an integral time scale of 1.3days (Rampal *et al.*, 2009a).

In other words, the trajectory of a sea ice particle keeps memory of its previous displacements twice as long in the model as in the observations.

If we assume that the correlation length is well represented in the model ice drift, considering the significant speed bias in the model (ice is drifting twice too fast), one would expect a smaller correlation time scale in the model. Since the correlation time scale we find is twice as long in the model as for buoys, it suggests a strong difference regarding the temporal evolution of model and observed ice drift.

Although the velocity distribution seems correctly represented in the model, the temporal evolution of velocity might not be as well simulated. This suggests that processes leading to the decorrelation of ice velocity, such as the fracturing and ridging activity of the ice cover, are perhaps not correctly simulated.

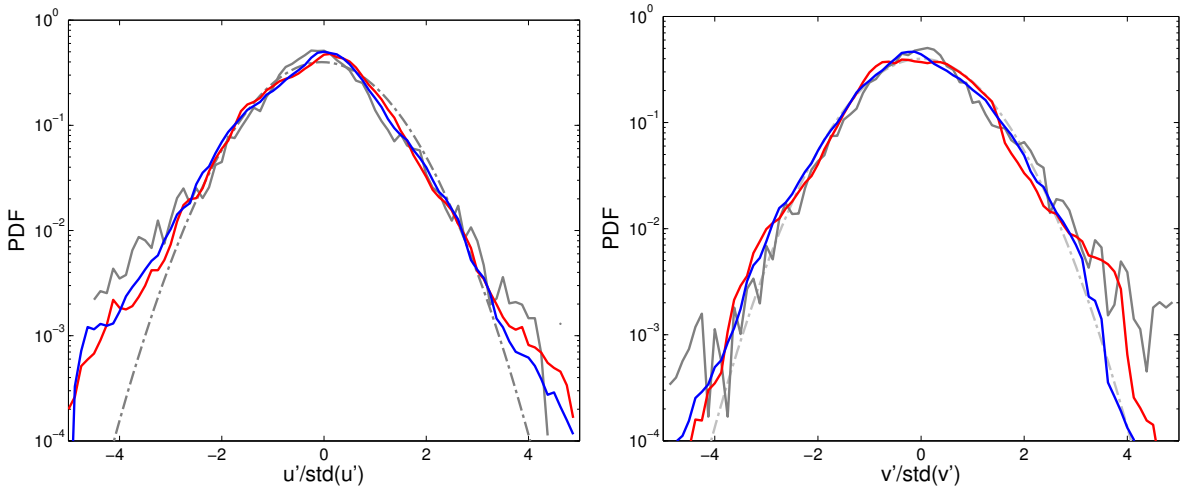

FIG. 2.4: PDFs of the two components of velocity fluctuations of 12-hourly velocity (u', left panel and v' right panel), normalized by their standard deviation (buoys measurements : grey, model, LIMVP : red, LIMEVP : blue) and the corresponding Gaussian distribution ($\mu = 0; \sigma = 1$, dashed line). The standard deviations are as follows : $std(u'_{buoys}) = 3.11$, $std(v'_{buoys}) = 3.28$, $std(u'_{LIMVP}) = 6.74$, $std(v'_{LIMVP}) = 6.05$, $std(u'_{LIMEVP}) = 6.13$, $std(v'_{LIMEVP}) = 5.53$.

2.5 Ice deformation

Sea ice deformation is examined in this section, first through a qualitative analysis of strain-rate fields, then by comparing distributions of model and RGPS strain-rates. Finally, we investigate the dependence of model strain-rates upon spatial and temporal scales using the methodologies developed by Marsan *et al.* (2004) and Rampal *et al.* (2008) to analyze RGPS and buoy data.

2.5.1 Strain-rate fields

Model Lagrangian trajectories presented in the previous subsection are used to compute the strain-rates following the same procedure as for RGPS (see section 2.2). We do this in order to ensure the best comparability of model and RGPS strain-rates, the latter being calculated within a Lagrangian framework. A coarse graining procedure is applied to obtain model strain-rates on a wide range of spatial scales, from the model grid size ($\sim$ 12km) up to 1000km. A temporal scale of 3 days is used to fit with the average sampling time interval of RGPS. The complete range of RGPS sampling intervals allowed for the analysis is 2 to 6 days.

Figure 2.5 shows an example of LIM and RGPS strain-rate fields at fine spatial scale, respectively 12km and 10km for the time period 16-18 January 1997. It makes sense to consider the model strain-rate at this scale because the rheology introduces variability at the grid scale, although it is smoothed by stability operators. It is certainly not expected that LIM should be able to reproduce the details of ice deformation at such scales. Beyond resolution problems, the importance of the stochastic component of ice velocity at such small scales needs to be accounted for. This implies that even if the model physics was perfect, the strain-rates could not be predicted in a deterministic sense. With all these considerations in mind, it is still trustworthy to analyze the general aspects of the model deformation fields from the example of figure 2.5. The LIMVP strain-rate fields appear very smooth and homogeneous, with larges patches of divergence and shear. The large regions with convergence ($\dot{\epsilon}_{div} < 0$) are surprising, considering the near 100% ice concentration over the whole area. In winter, when sea ice is confined into the Arctic basin, a pattern with large patches of convergence is incompatible with the mechanical behavior of a fractured plate for which convergence is associated with the closure of freshly opened fractures and the formation of pressure ridges, i.e. is necessarily strongly localized along narrow faults. The LIMEVP simulation shows linear-like features that can span over several hundred km, but they are not structured as clearly as the so-called Linear Kinematic Features (LKFs) seen in RGPS observations.

To further illustrate this differences, we considered the total amount of shear measured and simulated on this 3-day period. We calculated the fraction of ice surface area over which the highest values of shear were accommodated : At the scale of $10km$, in RGPS observations, 50% of all shear is accommodated by only 6% of the ice surface area, while in LIMVP and LIMEVP, it spans over respectively 23% and 18% of the surface area. The same calculation was done for shear rates at 100km spatial scale. In this case, 50% of all RGPS derived shear is accomodated by 13% of the surface area, while 50% of all simulated shear spans over 22% of the surface area for LIMVP and 18% for LIMEVP. Similar values were obtained with other snapshots. These numbers express the fact that large shear rate values are extremely localized in RGPS observations, where a few percents of the surface hold most of the deformation at 10km scale.

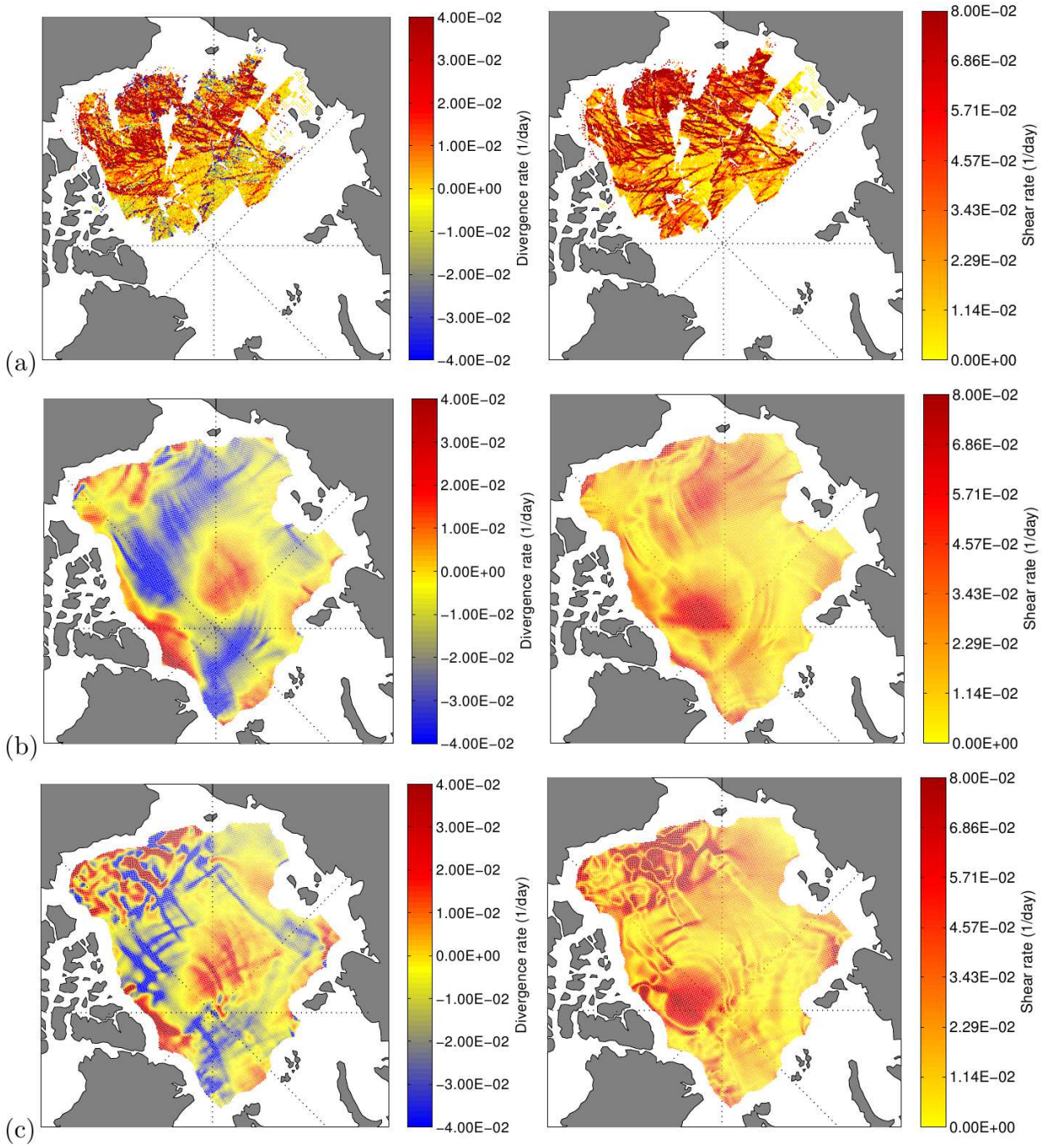

FIG. 2.5: Divergence and shear rate fields (/day), from RGPS observations (a), LIMVP (b) and LIMEVP (c), for the period 16-18 January 1997.

An interesting point is that the localization of deformation in RGPS observations is scale dependent, i.e. decreases with increasing spatial scale. Opposingly, in the simulations, the spatial scale does not seem to affect the localization of deformation. Could this result be explained by the model resolution ? or is there a physical discrepancy between the observed and simulated ice dynamics ?

The qualitative comparison presented in this subsection does not allow to differentiate these problems. The characteristics of strain-rate distributions, presented in the following subsection, provide insights towards this direction. These results are complemented by a full analysis of the scale dependence of deformation over a broad range of spatial and temporal scales in subsection 2.5.3.

2.5.2 Strain-rate distributions

Figure 2.6, 2.7 and 2.8, compare the RGPS and LIM PDFs of respectively divergence, absolute value of divergence and shear. These PDFs are obtained from the whole period (January-March 1997) with RGPS and model strain-rates at spatial scales of 10km and 100km and a temporal scale of 3 days. Table 2.2 gives the mean and standard deviations of these distributions and the ice speed statistics.

The speed bias that appears in table 2.2 is generally consistent with the results showed in section 2.4, the ice speed being faster in the model than in observations, but direct comparisions of the biases should be avoided since the observation datasets are very different in terms of accurary and spatial coverage. In both simulations, the bias in the ice speed affects the spatial velocity gradients and thus the strain-rates. This can presumably explain the difference between the mean shear rate in simulations and RGPS observations.

The RGPS PDF of divergence rates shows an asymmetry towards positive values, which is notably marked at 100km, while model PDFs are almost symmetrical with a slightly negative mean.

At 10km the standard deviations of model and RGPS strain-rates differ by an order of magnitude but this discrepancy vanishes at 100km. This does not imply that the model gets the right strain-rate distribution at this scale. Instead, the shape of the distributions should be examined.

Log-log scale plots (figure 2.7 and 2.8) show clear differences between the model and RGPS strain-rate distributions. The RGPS distributions of divergence and shear rates are fat tailed, following power law decays over two orders of magnitude ($p(\dot{\epsilon}) \sim \dot{\epsilon}^{-\eta}$), with slopes $\eta \leq 2.5$ at 10km and in the range $2.6 - 3.3$ at 100km. This is consistent with the analysis of Marsan *et al.* (2004) for RGPS derived total deformation rates. Instead, the model distributions show exponential decays and do not have such a noticable fat tail. Their slopes in a log-log scale (over the last half order of magnitude) are at least 3.5 at 10km and 5 at 100km. At 100km, model distributions are getting closer to the Gaussian distributions of same mean and standard deviation.

The difference in the shape of the distributions is fundamental. Indeed, since they are not fat tailed, model PDFs are in the Gaussian attraction basin. This means that, by addition of random variable, they would converge towards a Gaussian distribution (e.g. (Sornette, 2000)). In other words, they are associated with a 'mild randomness'.

On the other hand, RGPS distributions follow Levy's laws of stability parameter $\mu = \eta - 1$ (where η is the slope of the power law). Such distributions are characterized by 'wild randomness' and dominated by extreme values. When the distribution tail is shallow enough for $\mu \leq 2$, as for strain-rate distributions at 10km, the standard deviation is, analytically, infinity, while for $\mu \leq 1$ the mean is also undefined (Sornette, 2000). In practice, it is always possible to compute an empirical mean and standard deviation for a given set

		10 km , 3 days			100 km, 3 days		
		RGPS	LIMVP	LIMEVP	RGPS	LIMVP	LIMEVP
$\dot{\epsilon}_{div}$	mean	1.2×10^{-5}	-3.5×10^{-3}	-1.9×10^{-3}	1.2×10^{-3}	-3.1×10^{-3}	-1.7×10^{-3}
	std	0.17	0.019	0.22	0.016	0.017	0.017
$\dot{\epsilon}_{shear}$	mean	0.015	0.019	0.021	0.010	0.018	0.018
	std	0.23	0.17	0.025	0.020	0.015	0.017
$ice\ speed$	mean	3.6	8.0	7.3	2.5	3.4	3.2
	std	3.0	5.0	4.4	2.6	1.5	1.2
N		10^6	0.8×10^6	0.8×10^6	1.3×10^4	1.3×10^4	1.3×10^4

TAB. 2.2: Mean and standard deviations of divergence and shear rate (1/day) at 10 and 100km scales, and ice speed statistics (km/day). N is the number of observations or model values.

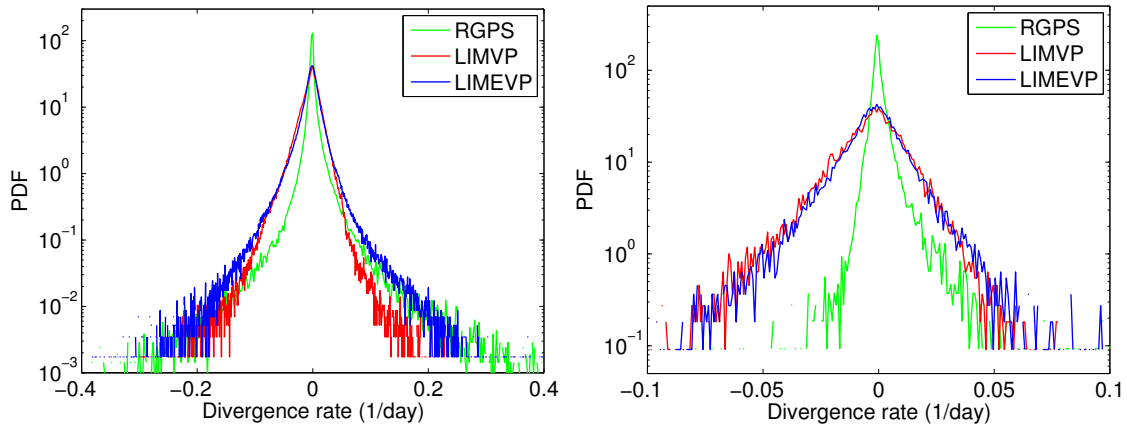

FIG. 2.6: PDF of divergence rates for the period January-March 1997, from RGPS observations (green), LIMVP experiment (red) and LIMEVP (blue), at scales of $\sim 10km$ (left panel) and $\sim 100km$ (right panel).

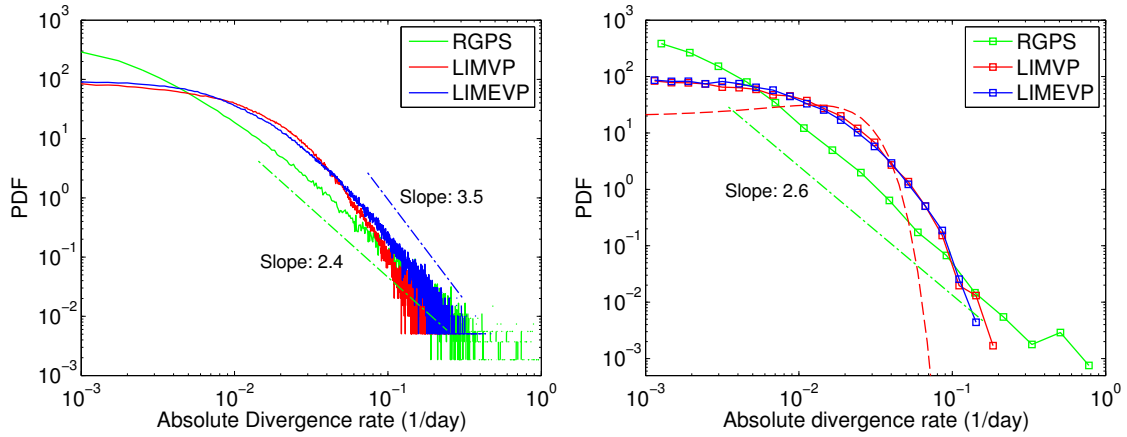

FIG. 2.7: PDF of absolute value of divergence rates for the period January-March 1997, from RGPS observations (green), LIMVP experiment (red) and LIMEVP (blue), at scales of $\sim 10km$ (left panel) and $\sim 100km$ (right panel). The green and blue dashed lines indicate, respectivelly, the slope of the RGPS and LIMEVP distributions. On the right panel, the red dashed line is the Gaussian distribution of same mean and standard deviation as the LIMVP distribution.

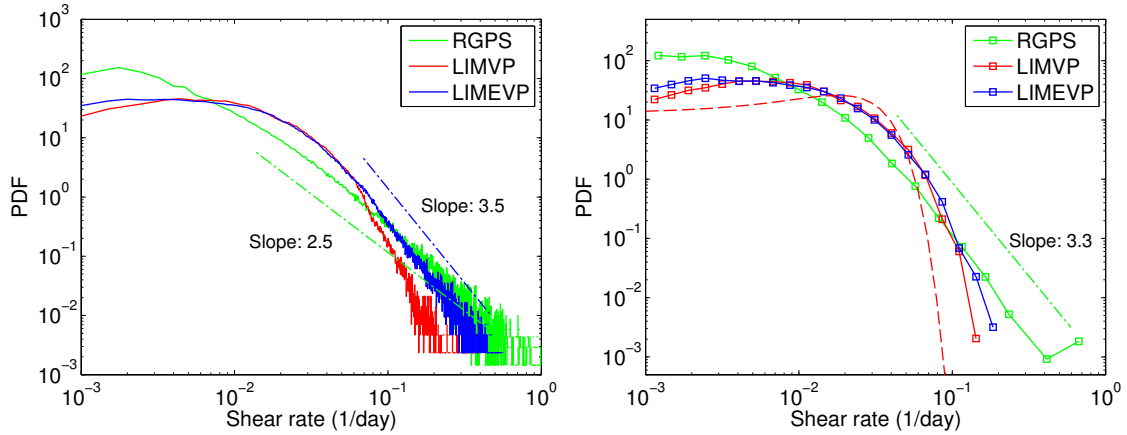

FIG. 2.8: PDF of shear rates for the period January-March 1997, from RGPS observations (green), LIMVP experiment (red) and LIMEVP (blue), at scales of $\sim 10km$ (left panel) and $\sim 100km$ (right panel). The green and blue dashed lines indicate, respectivelly, the slope of the RGPS and LIMEVP distributions. On the right panel, the red dashed line is the Gaussian distribution of same mean and standard deviation as the LIMVP distribution.

of strain-rates, but the shape of the RGPS distributions implies that the few largest values have substantial influence on these empirical mean and standard deviation. This means that distributions of strain-rates should not be compared only through their standard deviations and means, which are too volatile and dependent on the number of values considered. The comparison should instead consider the entire distributions. At 100km, even if the standard deviation of RGPS and model strain-rates are matching, the dissimilarity between the distributions actually increases : RGPS distributions are still power law tailed, whereas model distributions are getting closer to the Gaussian distribution.

If the strain-rates of the 10km cells were independent scalar variables, identically distributed following Levy's law of parameter μ, the PDF of strain-rates at any larger scale would also be a Levy's law of parameter μ. This is not exactly what is recovered here (μ tends to slightly increase with increasing scale), as strain-rates are tensorial variables and strong spatial correlations exist. To fully analyze the evolution of the PDF with scale, a multifractal analysis is necessary. This is performed in the next subsection.

As a point of comparison, figure 2.9 shows the PDF of absolute divergence rates obtained with the CICE simulation. As no RGPS observations are available for the time period of the simulation, we restrict our analysis to a few comments regarding the shape of the distributions. The PDFs simulated by CICE are rather similar to the LIMEVP distributions, without significant improvement in the shape of the PDFs. At 100km the CICE PDF has an exponential decay and approaches the Gaussian distribution.

This subsection has provided a first quantification of the strong discrepancy between simulated and observed strain-rate fields qualitatively described in subsection 2.5.1 and figure 2.5, as well as of the extreme localization of deformation within Arctic sea ice, a discrepancy that persists at scales much larger than the grid size. In the following subsection, we show that the existence of spatial and temporal correlations in the ice deformation field reinforces the discrepancy between models and observations.

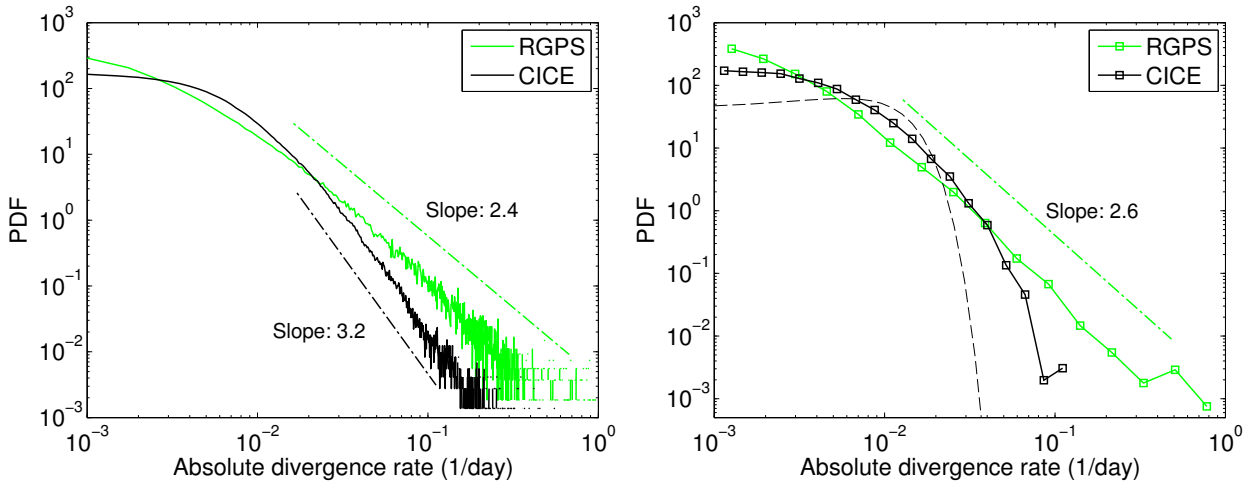

FIG. 2.9: PDF of absolute value of divergence rates from the CICE simualtion (period January-March 1987) and from RGPS observations (period January-March 1997), at scales of $\sim 10km$ (left panel) and $\sim 100km$ (right panel). On the right panel, the black dashed line is the Gaussian distribution of same mean and standard deviation as the CICE distribution.

2.5.3 Scaling properties of sea ice deformation

As shown in section 2.2, sea ice deformation patterns are characterized by spatial as well as temporal scaling laws which are the signature of long-range correlations and space-time coupling.

3-daily total deformation rates from January-March 1997 were binned with respect to their spatial scale (from 10 to ~ 1000km). The mean deformation value of each bin and associated mean scale are represented on figure 2.10, expressing the spatial scale dependence of total deformation rates, for RGPS observations and LIM simulations.

At all spatial scales and a time scale of 3days, a bias persists between the mean deformation of models and RGPS observations. This bias is consistent with the bias in the ice speed magnitude (the ice moves too fast in the model). However, this bias is not an essential criterion to test the accuracy of the simulations, as sea ice mean strain-rates strongly depend, by nature, on the spatial and temporal scales considered, whereas modelled mean strain-rates essentially do not. Consequently, one can find temporal and spatial scales at which simulations fit the observations, but this neither validates nor invalidates the model.

Instead, we focus our analysis on the scale dependence of strain-rates (i.e. the slope), which characterizes the heterogeneity of the deformation field.

The scaling $\langle \dot{\epsilon}_{tot} \rangle \sim L^{-b}$ is observed over two orders of magnitude for RGPS observations. A least squares fit to the mean values (dashed line), gives an exponent $b = 0.18$ with a squared correlation 0.99. This is consistent with the results of (Marsan *et al.*, 2004) who obtained a similar scaling with an exponent $b = 0.2$ for RGPS observations of fall 1997.

In the simulations, the power law scaling is not recovered. At small scales, the mean deformation simulated in LIMVP is nearly independent of L, then decreases for scales larger than $\sim 200km$. This decrease could be explained by a finite-size effect : due to the confinement of the Arctic basin, a box of the order of the basin scale is not free to deform significantly. We note that for the scaling analysis of RGPS strain-rate, this finite-size effect, which necessarily exists, is masked by the power law scaling. The scale dependence of LIMEVP mean deformation is slightly more pronounced than for LIMVP, but clearly not a power law.

The difference between model and observations appears even more distinctly when considering the scale dependence of the moments $\langle \dot{\epsilon}_{tot}^q \rangle^{1/q}$ of order $q = 2$ and 3 (figure 2.11). Moments of higher order give more weight to the large strain-rate values. RGPS moments follow power laws with exponents depending on the moment order q, while LIM moments do not vary significantly with the moment order, neither with the spatial scale. For RGPS observations, the dependence of the exponent with q expresses the multifractal character of the strain-rate field, in agreement with previous work (Marsan *et al.*, 2004), the fingerprint of the multifractal heterogeneity. This heterogeneity is absent for simulations.

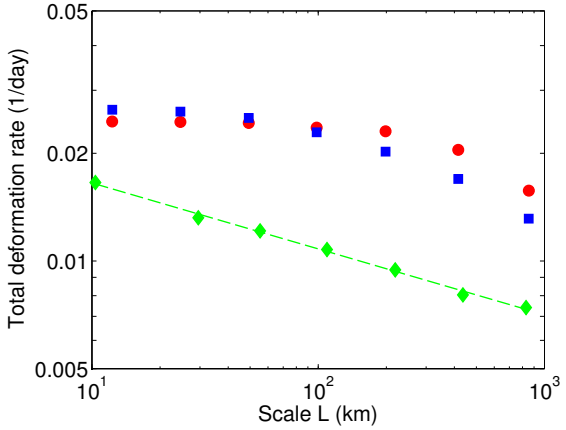

FIG. 2.10: Mean total deformation rate $\langle \dot{\epsilon}_{tot} \rangle$ as a function of spatial scale L, obtained with RGPS observations (green diamonds), LIMVP (red circles) and LIMEVP (blue squares) simulations. The dashed line is the least squares fit for RGPS data $\langle \dot{\epsilon}_{tot} \rangle \sim L^{-0.18}$.

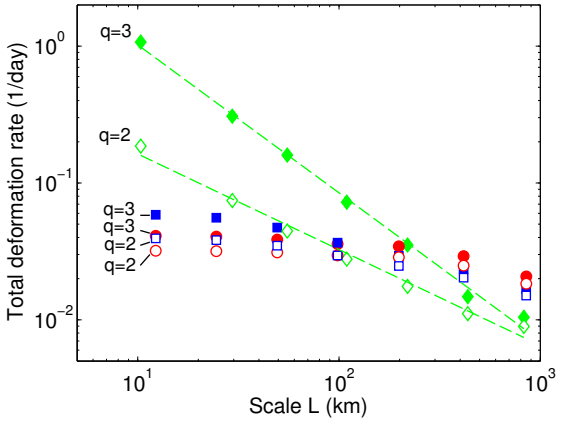

FIG. 2.11: Moments of the total deformation rate $\langle \dot{\epsilon}_{tot}^q \rangle^{1/q}$ as a function of spatial scale L, for $q = 2$ and 3, for RGPS (green diamonds), LIMVP (red circles) and LIMEVP (blue squares). The dashed lines are least squares fits for RGPS moments.

The results reported on figures 2.10 and 2.11 show that the spatial correlations of deformation patterns are not correctly reproduced in LIM. The scale dependence of strain-rates simulated by CICE was also examined (not shown here) through a similar procedure and did not match the power law decay either.

As mentioned in section 2.2, RGPS is not suited to explore in details the temporal scaling as well as the space-time coupling of sea ice deformation, which was revealed by the analysis of the dispersion of buoys trajectories (Rampal *et al.*, 2008). To evaluate the model performance on this basis, we used the reconstructed Lagrangian trajectories (see section 2.4.2) and followed the procedure presented in section 2.2 to estimate the strain-rate proxy $\dot{\epsilon}_{disp}$ from dispersion rates. This was done for a wide spatio-temporal scale range, with initial separation L varying from $\sim 10km$ to $\sim 500km$ and time interval τ varying from 12h to 45 days. Model dispersion rates were then compared to dispersion rates obtained from IABP buoys trajectories during the January-March period, covering 23 years from 1979 to 2001.

The differences between observed and modeled dispersion rates $\dot{\epsilon}_{disp}$ are striking (figure 2.12) : in both simulations, $\dot{\epsilon}_{disp}$ is nearly independent of the temporal and spatial scales considered, whereas it shows a strong decrease with scales when calculated from observations. Once again, this figure shows that, to evaluate the performance of a model, a comparison of mean strain-rates performed at specific arbitrary scales is meaningless. Although simulations can match observations at some scales, the entire scale dependence should be checked.

This discrepancy between models and observations confirms that (i) the models are unable to reproduce the spatial correlations of the deformation field and (ii) that they do not reproduce the temporal correlations either.

To illustrate the difference between simulations and observations, we calculated the ratio of the strain-rate proxy at two different time intervals and spatial scales :

$$\frac{\dot{\epsilon}_{disp}\,[10\text{km}, 1\text{day}]}{\dot{\epsilon}_{disp}\,[300\text{km}, 50\text{days}]} \tag{2.7}$$

This ratio is ~ 2 in simulations, essentially as the result of finite size effect (see above), whereas it is more than one order of magnitude higher (~ 60) for buoy data.

Moreover, the deformation rates estimated by both models agree with the observations at large spatial scales (100-300km), suggesting that all the variability regarding sea ice deformation below such scales is missing in both models, regardless of their high resolution ($\sim 10km$ grid size). This is consistent with the conclusions of Taylor *et al.* (2006) who suggested that the adoption of isotropic, continuum rheology at sub-100km resolutions is not useful for a more detailed prediction of ice dynamics.

Dispersion rates calculated with the CICE simulation were also examined and exhibit almost no temporal and spatial scale dependence compared to buoy dispersion rates.

The dependence of $\dot{\epsilon}_{disp}$ upon time and spatial scales is an expression of the intermittency and heterogeneity of sea ice deformation, fully characterized by the scaling laws (2.5) and (2.6) (see section 2.2). These scaling laws are not recovered in the models : The strain-rate proxy $\dot{\epsilon}_{disp}$ is essentially independent of time scale as well as spatial scale, i.e. $\alpha \simeq \beta \simeq 0$. In other words, modeled sea ice behaves as a viscous fluid (Rampal *et al.*, 2008), with little spatial heterogeneity and no intermittency of the deformation.

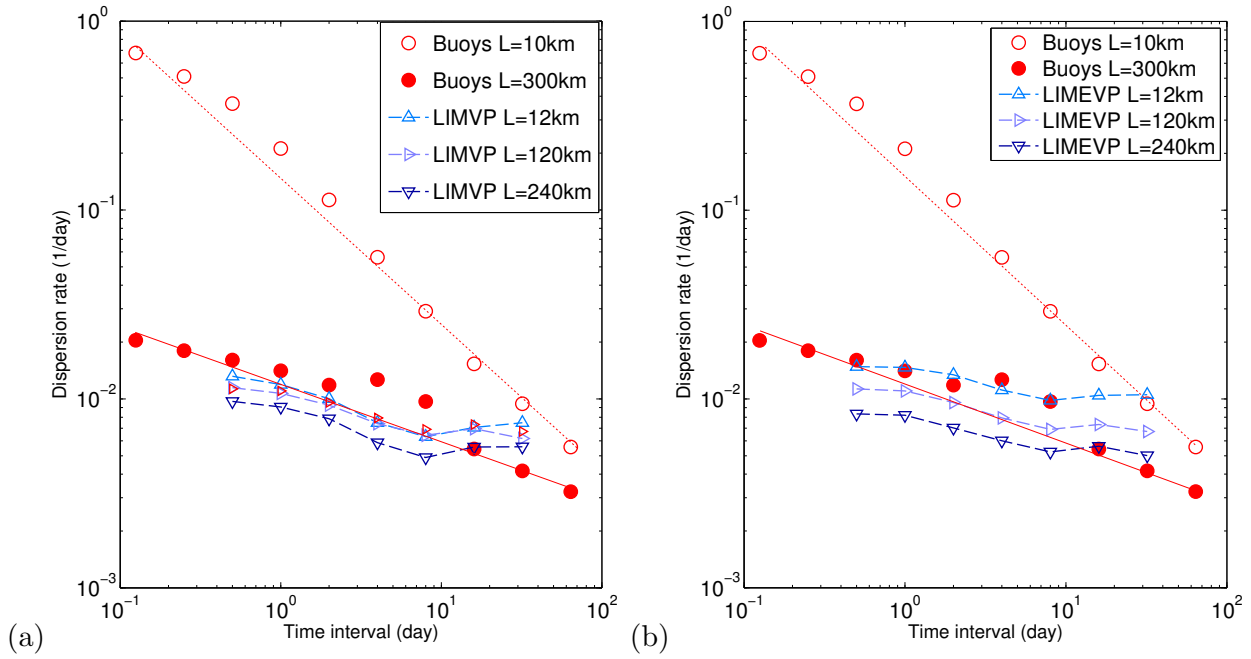

FIG. 2.12: Spatial and temporal scale dependence of the dispersion rate $\dot{\epsilon}_{disp}$ for buoys data, LIMVP (a) and LIMEVP (b). The dashes lines are power law fits to buoys dispersion rates.

2.6 Discussion

This section discusses the causes of the discrepancy between model and observations. The influence of forcing and resolution problems against a real issue with the model physics is examined.

2.6.1 Insights from the statistical analysis of ice deformation

The simulated mean ice drift field shows significant correlations with observations at large scales (400km,3months) eventhough a large bias on the mean speed is noted and taken into account throughout the paper. At smaller scales, the distributions of simulated ice velocity fluctuations compare relatively well with buoys observations. The correlation time scale of velocity fluctuations is abnormally large in the model, suggesting incorrect spatial and/or temporal correlations of the velocity fluctuating field. Major differences between model and observations appear when analyzing the strain-rates. The distributions of RGPS derived strain-rates differ from the simulated distributions on a wide range of scales. The speed bias in the simulations affects the strain-rates but only in terms of absolute values. This could explain the bias in the mean strain-rate seen in simulations but it does not have any effect on the shape of strain-rates distributions, nor on the scale dependance of strain-rates.

To exclude the influence of the model resolution on the discrepancy with the observations, the comparisons of strain-rate distributions were done at different scales. The difference in the nature of the PDFs remains at large scale (100km), with a clear power law decay in the observations, which does not appear in the simulated distributions. Therefore, the model resolution cannot be the main cause of this problem. The fact that the shape of distributions differs suggests that the model does not represent correctly the physical processes of ice deformation.

Sea ice dynamics is mainly driven by wind forcing, which is derived from re-analysis in the simulations. Thus, boundary layer turbulence and small scale variability of the wind stress on sea ice is not represented. This could partly account for the lack of large deformation rates and the smoothness of deformation fields. In

other words, the part of the stochastic component of sea ice velocity which is directly linked to the short-term wind fluctuations is not represented.

However, ice velocity fluctuations do not only result from short term wind forcing. They also emanate from the ice mechanical behavior, through the internal ice stress term of the equation of motion, which is calculated by the rheology. Rampal *et al.* (2009a) recently detailed the importance of the ice rheology on the velocity statistics. Weiss (2008) showed that the intermittency of ice stresses is not inherited from wind forcing but emerges from sea ice mechanics. This suggests that if the ice mechanics is well represented in the model, its fingerprint should appear in the ice velocity and strain-rate statistics, even if the forcing is not perfect.

Another consequence of the ice mechanical properties is the spatial and temporal scaling laws of sea ice deformation (relations 2.6 and 2.5). These relations express the strong intermittency and high heterogeneity of the deformation fields (Marsan *et al.*, 2004; Rampal *et al.*, 2008) and associated space and time correlations.

Since we have shown that the scaling laws are not reproduced in any of the models, and that strain-rate distributions differ in shape from the observations, we argue that a possible reason for the incorrect representation of the statistical properties of sea ice deformation could be mainly due to the model physics, and more specifically the mechanical framework used in the models.

2.6.2 A different mechanical framework for sea ice mechanics ?

In the classical VP framework (Hibler, 1979), the parameterization of the ice strength P depends on the ice concentration A, inducing a weakening mechanism : a decrease in A leads to a reduced ice strength and increased deformation. The goal of this parameterization is to localize the deformation, through a positive feedback loop. However, the effects of this parameterization are limited to single grid cells, as stresses are not redistributed on the other nodes of the mesh, since the VP rheology does not consider elastic interactions. The parameterization of P appears inadequate to simulate correctly the properties of the deformation fields. The tuning of different rheology parameters, such as the creep limit in our case, proved to have insignificant effects on the results. Moreover, in such a scheme, there is no direct link between deformation (and particularly divergence), and ice concentration. This analysis commensurates with the conclusions of Coon *et al.* (2007) who suggested a different view of the dynamics of pack ice and underlined the need to directly account for velocity discontinuities in order to get a good representation of deformation.

Weiss *et al.* (2007) argued that the deformation of the sea ice cover is essentially elasto-brittle, the inelastic deformation being accommodated by differential displacements along fracture and fault planes, from the scale of the ice thickness ($\sim$ m) to geophysical scales (10^3km for the Arctic basin). Considering the sea ice cover as an elastic plate, long range elastic interactions take place between fractures. Consequently, a small perturbation can trigger much larger events, and scaling laws as well as intermittency emerge naturally.

It is worth noting that, using a discontinuous Lagrangian approach to explicitly model ice floes and the interactions between them such as fracturing and the propagation of stress relaxation, Hopkins & Thorndike (2006) reproduced the power-law distribution of floe sizes in a regional model, as observed from satellite images (Weiss & Marsan, 2004).

Following these arguments, we believe that a different mechanical framework should be developed for sea-ice in global models, introducing the long-range elastic interactions that are at the root of the scaling properties described above. Elasto-brittle models introducing a progressive damage law with an associated failure criterion already proved to successfully reproduce the complexity and scaling properties of strain

fields in the Earth's crust (Cowie *et al.*, 1995), or of rocks damage (Amitrano *et al.*, 1999).

The inadequate representation of the fluctuating part of sea ice kinematics may have strong consequences in terms of ocean-atmosphere thermodynamic fluxes. These fluxes are extremely sensible to fluctuations of the open water concentration, i.e. on lead/fracture opening and closing which are themselves linked to kinematical variables (e.g. divergence). As an example, a change in the ice concentration of 1% within 48 hours induces a difference in the temperature of the atmospheric boundary layer up to 3.5K (Lüpkes *et al.*, 2008). Erroneous sea ice concentrations in models have a strong impact on simulations as ice concentration is one of the most important factor of the surface energy budget (Maykut & Untersteiner, 1971; Sorteberg *et al.*, 2007). Furthermore, the spatial repartition of leads and polynyas also control the heat budget, since narrow leads transfer heat more efficiently than larger ones (Andreas & Cash, 1999) : the relationship between lead opening and heat transfer is strongly non-linear. Consequently, average values such as average ice concentration or average strain-rates contain little information to correctly simulate thermodynamic transfers.

All these results demonstrate the need of a precise representation of the spatial distribution of open water and leads in numerical models. We believe that this can only be achieved if the strain-rate fields are well captured. By this, we mean that statistical and scaling properties should be well represented, as the small scale stochastic component of kinematics is by nature impossible to *predict* in a deterministic sense.

2.7 Conclusions

In this paper, ice motion from three different simulations is evaluated on the basis of statistical and scaling properties of sea ice drift and deformation. Two simulations were obtained with the Louvain-la-Neuve Ice Model (LIM) coupled to a high resolution ocean model (12km grid scale), one with VP ice dynamics and the other one with EVP dynamics. The third simulation was obtained with the Los Alamos Sea Ice Model (CICE), coupled to a simple ocean mixed layer (9km grid scale).

The results presented in this paper focus mainly on the two LIM simulations, which are examined in terms of mean velocity field, distributions of ice velocity fluctuations, strain-rate distributions and scale dependence of strain-rates. Only a few important results regarding the statistical properties of ice deformation are presented for the CICE simulation.

The main conclusions of this work are :

1. At large scales (400km, 3months), the mean velocity field simulated by LIM is fairly well represented, although a significant bias on the simulated ice speed is noted. At finer scales, below a few hundred km and few months, the velocity field is dominated by the stochastic component of ice velocity and direct comparisons through correlation coefficients are inappropriate. Instead, simulated velocities are evaluated at small scales through the distributions of velocity fluctuations. Model and buoy distributions of velocity fluctuations compare favorably.

2. There is a strong discrepancy between model and RGPS distributions of strain rates : strain-rates derived from RGPS observations exhibit 'wild randomness', with power law tailed distributions, whereas simulated distributions show 'mild randomness' and remain in the Gaussian attraction basin. This discrepancy persists at scales much larger than the model grid size (100km).

3. The analysis of strain-rate distributions also provided valuable information for further evaluations : the properties of RGPS distributions imply that means and standard deviations of strain-rates are volatile, their value is controlled by a few extreme strain-rate values. Evaluation of model strain-rates should therefore consider the entire distributions and not only the means and standard deviations.
4. The models are unable to reproduce the spatial and temporal correlations of the deformation fields : In the observations, ice deformation depends of scales following specific spatial and temporal scaling laws that express the heterogeneity and the intermittency of deformation. These relations do not appear in simulated ice deformation. Mean deformation in models is almost scale independent.
5. The incorrect representation of the statistical properties of ice deformation could be mainly explained by the mechanical framework used in models : the scaling laws of deformation and the shape of strain-rate distributions are properties that emanate from the ice mechanical behavior. The fact that these properties are not represented in models suggests that the modeling framework is inappropriate. A different modeling framework, including elastic interactions, could improve the representation of ice deformation in models.

Acknowledgments

The RGPS and SSMI ice motion data were provided by the Polar Remote Sensing Group at JPL, and the buoy data by the IABP at the Polar Science Center, University of Washington. We acknowledge the DRAKKAR consortium for providing the LIM model outputs, and especially the support of CNES to the distribution of the DRAKKAR simulation products. Simulations with the LIM model were carried out at the CNRS IDRIS supercomputer facility in ORSAY. We also thank W. Maslowski from the Naval Postgraduate School, California, who kindly provided CICE data. We are grateful to two anonymous reviewers for a careful review of the paper. L. Girard is supported by a BDI phD grant from CNRS.

Chapitre 3

La rupture comme point critique dans un modèle d'endommagement progressif

D'après :
Girard, L., D. Amitrano and J. Weiss (2010), Failure as a critical phenomenon in a progressive damage model, Journal of Statistical Mechanics : Theory and Experiment, (P01013).

Abstract

The critical point hypothesis for fracture is tested using a progressive damage model. The advantage of the present model, based on continuum mechanics, is the possibility to track the approach to final failure either in terms of discrete events (the avalanches) or of the resulting continuous strain field. Different but actually closely linked phenomena are reported. In terms of damage avalanches, power law distributions of avalanche sizes and energies are observed associated to a finite size scaling. The finite size scaling is also observed for the spatial correlations of damage events. A divergence of the correlation length is reported in the vicinity of final failure, from a correlation analysis of discrete events and from a scaling analysis of the continuous strain-rate field. We also show that multifractal properties of the deformation emerge from the long range elastic interactions that occur near final failure. All these results argue for a critical point interpretation of failure. Finally, we discuss the implications of our results on the criticality of fracture and deformation of geophysical objects, and on associated precursory phenomena.

3.1 Introduction

Fracture is a multiscale phenomenon, from the scale of individual crystals (μm to mm) to the scale of plate tectonics or of the Arctic sea ice cover (beyond 10^3 km). To predict the failure of a sample, a structure, or a geophysical object is a long-standing problem of fundamental importance in engineering or in geophysics (e.g. to tentatively predict earthquakes). In the classical Griffith's theory of brittle fracture in a pure crystal (Griffith, 1920), disorder is absent within the material except a single flaw which size and geometry dictate the failure strength. In this case, upon increasing the applied stress (or strain), to predict the failure in a deterministic sense is impossible, except if one knows exactly the characteristics of the flaw, as failure occurs suddenly without precursors. If one draws an analogy with phase transition, this transition to failure is of first-order (Alava *et al.*, 2006; Sornette & Andersen, 1998). However, disorder is inherent in any real material and its role on fracture and strength has been stressed for a long time (Weibull, 1939). The classical approach to deal with this problem is purely statistical, considers a population of flaws within the material with various sizes and characteristics, and assumes that the failure of the whole structure is dictated by the activation of the most dangerous (generally the largest) flaw. This weakest-link approach assumes that defects are non-interacting, and have no effect on the propagation of a crack once nucleated. This approximation seems reasonable in the case of a structure with weak disorder (i.e. the local, « microscopic » strength is narrowly distributed), under loading conditions that do not stabilize crack propagation (e.g. monotonic tension).

In case of stronger disorder and/or loading conditions under which crack propagation is more stable (e.g. compression, shear), the situation is different. For the last several years, there has been growing evidences, either experimental or from statistical models, that « macroscopic » failure can be preceded, actually foretold by several precursory phenomena. Fracture in heterogeneous media is considered to be an example of crackling noise, i.e. the system responds to slow externally applied driving through discrete, impulsive events spanning a broad range of sizes (Sethna *et al.*, 2001). Experimentally, the most powerful non-destructive technique to record this crackling noise is acoustic emission (AE). Power law distributions of AE energies, $P(E) \sim E^{-\beta}$, have been observed for various loading conditions and materials (Deschanel *et al.*, 2009; Amitrano, 2003; Amitrano *et al.*, 2005; Salminen *et al.*, 2002; Petri *et al.*, 1994; Scholz, 1968), taking into account all the events recorded throughout the test. However, fracture at the laboratory scale under monotonic loading is characterized by a lack of time invariance, i.e. the activity strongly increases as approaching final failure (defined as the maximum sustainable stress σ_c). A decreasing β has been reported to accompany this increasing activity, that is, larger events become relatively more frequent, for laboratory experiments as for collapse of rocky cliffs and more controversially for earthquakes or volcanoes (Amitrano *et al.*, 2005; Smith, 1981; Scholz, 1968).

This evolution can also be tracked by an increase of the integrated energy release rate δE. This increase can result from an increase of the average event size, as noted above, and/or from an increasing event rate (Deschanel *et al.*, 2009). Under strain-rate control, this energy release rate has been observed to increase exponentially before failure (Guarino *et al.*, 1998; Salminen *et al.*, 2002), whereas there is some evidences of a power-law divergence under stress control $\delta E \sim [(\sigma_c - \sigma)/\sigma_c]^{\kappa}$, (Guarino *et al.*, 1998) (under these conditions, this can be equivalently expressed as a function of time, $\delta E \sim (t_c - t)^{\kappa}$). Such behavior has been reported for constant load conditions, that is, creep (Amitrano *et al.*, 2005; Nechad *et al.*, 2005; Amitrano & Helmstetter, 2006). The approach to failure can as well be tracked in the spatial domain : hypocenters of AE events related to fracture precursors appear to be more and more clustered as approaching failure, and this has been quantified through a decrease of the associated fractal dimension (Guarino *et al.*, 1998; Lockner, 1993; Lockner *et al.*, 1991; Lockner & Byerlee, 1991; Hirata *et al.*, 1987). These precursory phenomena

and associated scaling laws suggest an analogy with critical phenomena, the transition to failure becoming in this case a critical « phase » transition (Sornette & Andersen, 1998). However, this interpretation is still controversial (Alava *et al.*, 2006; Picallo & Lopez, 2008).

To test these ideas, different statistical models of fracture have been developed, with increasing levels of complexity, from the equal load sharing fiber bundle (FBM) model (e.g. (Hemmer & Hansen, 1992)), to more sophisticated lattice models such as the random fuse model (RFM) (Herrmann & Roux, 1990) or the more realistic tensorial random spring model (RSM) (Alava *et al.*, 2006), which both take into account long-range interactions within the media. In all these models, macroscopic failure is preceded by avalanches of local failure events. Power law distributions of avalanche sizes S (defined as the number of broken fibers or bonds) and energies E (Picallo & Lopez, 2008) have been obtained, however with exponents depending on the model considered. Finite-size scaling has been reported for these distributions, an argument in favour of a critical interpretation of failure (Picallo & Lopez, 2008; Zapperi *et al.*, 2005).

The evolution of these distributions during the fracture process has been also interpreted as a signature of imminent failure. For the FBM and the RFM, a cross-over behavior in the avalanche distribution has been reported, defining two scaling regimes associated to two specific power law exponents and with a cross-over scale that diverges as approaching the final failure (Picallo & Lopez, 2008; Pradhan *et al.*, 2005). Zapperi *et al.* (2005) showed instead, for the RFM, truncated power laws, $P(S) \sim S^{-\beta} \exp(-S/S_0)$, with an exponential cut-off S_0 diverging towards final failure. In both cases, this divergence of the cross-over scale or of the cut-off means that the average avalanche size is increasing, in qualitative agreement with the increase of the energy release rate observed in experiments. In the spatial domain, a decrease of the correlation dimension of the broken bonds patterns has been reported for an antiplane shear loading of a RSM (Cowie *et al.*, 1995) and for a continuous damage model under compression (Amitrano *et al.*, 1999; Amitrano, 2006), indicating a progressive spatial clustering of fracture events as approaching final failure.

Fracture at the laboratory scale seems therefore preceded by several precursory phenomena that can be interpreted in terms of a critical phase transition, and might allow to predict failure to some extent (Sornette & Andersen, 1998). Is this framework still relevant at geophysical scales, as often postulated (e.g. (Bowman *et al.*, 1998; Pradhan *et al.*, 2009; Grasso & Sornette, 1998)) ? This question arises as the fracture of a geophysical object like the Earth's crust is also characterized by scaling laws, such as a power law distribution of earthquake energies (Gutenberg & Richter, 1954), or a fractal clustering of hypocenters (Kagan, 2007; Kagan & Knopoff, 1980). In the case of the Arctic sea ice cover, seismic monitoring of fracturing is scarce (see e.g. (Weiss, 2003)), but the much faster dynamics allows to track from satellite imagery directly the evolution through time and space of the deformation field resulting from the multiscale fracturing (Marsan *et al.*, 2004). These strain fields are characterized by time and space scaling laws that can be theoretically related to the scaling laws describing the space and time clustering of fracture events (Weiss *et al.*, 2009).

However, a fundamental difference exists between these geophysical situations and the fracture at the laboratory scale : the time invariance. Neither the Earth's crust nor the sea ice cover have fallen apart entirely so far. At large time and spatial scales, the system remains in a « marginally stable » state characterized by apparently stable scaling laws. This might be explained by the presence of healing mechanisms that compensate for the fracturing. Nevertheless, attempts have been done to export the critical point concept, with precursory phenomena, to the Earth's crust at a regional scale, in order to tentatively predict large earthquakes. These approaches were based on a possible divergence of the energy release rate (Bowman *et al.*, 1998; Bufe & Varnes, 1993), a divergence of the correlation length of earthquakes epicenters (Zoller *et al.*, 2001) or a modification of the power law exponent of earthquake energies (Jaume & Sykes, 1999).

Both power-law acceleration of energy release and decrease of the power-law exponent has been observed before a chalk cliff collapse (Amitrano *et al.*, 2005). Note that in this case the object failed entirely, as done at the laboratory. Despite this notable successful exception, these approaches remain however highly controversial, without convincing success so far (Hardebeck *et al.*, 2008).

In this paper, we test the critical point hypothesis for fracture from a progressive damage model. The continuum mechanics framework allows to track the approach to failure either in terms of discrete events (the avalanches), or of resulting strain fields. Different, but actually closely linked phenomena are reported, which all can be interpreted as a divergence of the correlation length as approaching final failure, therefore arguing for a critical point interpretation of failure. A relationship between the exponents characterizing the avalanche size and energy distributions and the strain-field is proposed. The paper is organised as follows, section 3.2 describes the progressive damage model and the set of simulations used in this study. Section 3.3 covers the analysis of the distributions of avalanche size and energy. Spatial correlations of damage are examined in section 3.4, while the spatial dependance of the strain-rate field is considered in section 3.5. The results are finally discussed in section 3.6.

3.2 Numerical modelling

The model we used is based on progressive isotropic damage that is represented by the reduction of the elastic modulus, reflecting the increase of cracks density (see e.g. (Kachanov, 1994) for the relationship between crack density and effective modulus). Such framework is in good agreement with progressive damage observed in brittle materials at the laboratory sample scale (Katz & Reches, 2004; Amitrano & Schmittbuhl, 2002), particularly when loaded in compression. The effective elastic modulus, Y_{eff}, is expressed as a function of the initial modulus, Y_{ini}, and the damage parameter, $d < 1$.

$$Y_{eff} = Y_{ini} d. \tag{3.1}$$

Such a relationship is valid for a domain which is large compared with the micro-defect size. This supposes that each element is large enough compared with the elementary cracks. In such a case, the damage can be associated to a crack density. The simulated material is discretized in triangular elements using a finite element method with plane-stress hypothesis. The strain and stress fields are considered explicitly as continuum. The hypothesis of elastic softening applies well under compression as elastic behaviour is observed for a wide range of materials with elastic modulus spreading over several orders of magnitude. The loading consists in uniaxial compression, applied by increasing the vertical displacement (strain controlled loading) or force (stress controlled loading) on the upper boundary of the model. The lower boundary of the model is fixed (no displacement) while the left and right boundaries can deform freely, as shown on figure 3.2a. In strain driven simulations, the loading increment is extrapolated to damage the weakest element, whereas in stress driven simulations, a constant increment stress is applied. In both cases, the loading increment ensures a very low driving rate, so that stress redistribution during an avalanche happens almost instantaneously, as expected in real materials. This defines a loading step. After each loading step, when the stress of an element, i, exceeds a given strength threshold for damage, its elastic modulus, Y_i, is multiplied by a factor d_0, d_0 being a constant slightly smaller than 1 ($d_0 = 0.9$).

$$Y_i(n+1) = Y_i(n) d_0, \tag{3.2}$$

n being the number of damage events of the element i. After n damage events, the effective modulus, $Y_i(n)$ of element i is given by

$$Y_i(n) = Y_{i,0}{d_0}^n \tag{3.3}$$

where $Y_{i,0}$ is the initial Young's modulus. Because of the elastic interactions, the stress redistribution around a damaged element can induce damage on neighboring elements and onset an avalanche of damaged elements. The avalanche stops when the damage criterion is no more fulfilled by any element. The damage threshold is calculated using the Mohr-Coulomb criterion, which applies for brittle materials under compressive stress states (Jaeger & Cook, 1983),

$$\tau = \mu\sigma_N + C \tag{3.4}$$

where τ is the shear stress, σ_N is the normal stress, C is the cohesion and μ is the internal friction coefficient. To simulate material heterogeneity, the value of the cohesion C is randomly drawn from a uniform distribution. C is only drawn once at the beginning of the simulation (quenched disorder). Redrawing a new cohesion from the initial distribution each time an element is damaged (annealed disorder) does not significantly affect the results. Randomness is necessary to obtain macroscopic behaviors differing from those of the elements and to avoid trivial behavior (failure without precursors at a prescribed strength and simultaneous damage of all elements). Compared to more classical statistical models of fracture, the modulii Y_i and the cohesion C are the equivalents of respectively the springs stiffness (RSM) and the bond breaking threshold (Zapperi *et al.*, 1997). To analyse the influence of material heterogeneity, two series of simulations are performed with different ranges of heterogeneity. For the H_1-range, C is drawn from 5×10^{-4} to $10^{-3} \times Y_{ini}$, while for the broader H_2-range, C is drawn between 2×10^{-4} and $10^{-3} \times Y_{ini}$.

A wide range of macroscopic behaviors can be simulated by the model, from brittleness to ductility. This variety of behaviors appears to be controlled by μ which influences the local interaction geometry and therefore controls the ductile-brittle transition (Amitrano *et al.*, 1999; Amitrano, 2003, 2006). In this study, we use $\mu = 0.7$ which is common to most geo-materials, such as granite, sandstone, limestone (Byerlee, 1978; Jaeger & Cook, 1983) and ice (Weiss & Schulson, 2009). The simulations are performed on rectangular meshes (height to width ratio of 2) of triangular elements. Two sets of meshes are used, "structured meshes" with similar orientation of all triangles and "random meshes" with random orientation of triangles. Meshes of linear size L varying from 4 to 128 are used, where the total number of elements is given by $N_{mesh} = 4L(L-1)$. Extensive statistical sampling was used to obtain the results presented in the following sections. The number of independant simulations performed with each system size is 5000 up to $L = 16$, 3000 for $L = 32$, 500 for $L = 64$ and 20 for $L = 128$. Simulations on structured meshes are only performed with the H_1-range.

The simulations are started with an undamaged material. In the early stage of the simulation, damage is homogeneously scattered throughout the system and the macroscopic behavior of the material is linear. As avalanche activity increases, a deviation from elasticity is observed, corresponding to a softening of the material (figure 3.1). At this stage, avalanches of all sizes can occur. In strain driven simulations, large avalanches induce a drop in the macroscopic stress and a temporary stabilization of the system. Such relaxation cannot occur in stress driven simulations as stress is continuously increased. Finally, a catastrophic avalanche occurs, spanning from one side of the system to the other (figure 3.2). In stress driven simulations, the catastrophic avalanche grows indefinitely, as the material cannot hold the imposed stress anymore. Instead, in strain driven simulations, the catastrophic avalanche is followed by a steady state with a macroscopic plastic

Symbol	
S	Avalanche size
E	Dissipated elastic energy
$\alpha,\ \beta$	Avalanche size/energy distribution exponents
δ	Avalanche size/energy cut-off exponent
γ	Avalanche size/energy critical exponent
D	Correlation dimension
$\xi,\ \lambda$	Correlation length and critical exponent related
η	cut-off exponent of the correlation length
$\dot{\epsilon}$	Deformation rate
$\rho,\ \nu$	Scaling and critical exponents of deformation

TAB. 3.1: List of main variables and exponents

behavior. In this state, the strain increments are compensated by damage in a way that the macroscopic stress remains approximately constant (Zapperi *et al.*, 1997). The structured mesh is anisotropic inducing preferential directions for damage propagation as shown on figure 3.2. This is not the case for the random mesh, which is isotropic. However, a rigorous analysis of fracture orientation is not in the scope of this study. In what follows, we focus the analysis on the pre-failure state, up to peak load, which we consider as a critical point. The main variables and exponents used in the analysis are presented in table 3.1.

3.3 Avalanches

In this section we analyze the distributions of avalanches in terms of size and dissipated energy. We define the avalanche size S as the number of damaged elements during a single loading step. In large avalanches, an element can encounter several damage events within a loading step but this is not quantified in S. However, we verified that S scales linearly with the number of damage events, i.e. the effect of multiple damage on a same element is minor. Considering elements of equal surface areas, S is proportional to the fault surface area involved in the avalanche. The dissipated elastic energy can be considered as the main contributor to AE and there is strong experimental evidence that AE is a localized phenomenon in space and time so that energy release occurs at microfracture scale (Guarino *et al.*, 1998; Lockner, 1993; Evans, 1979). We therefore define the dissipated elastic energy E as the sum of the energy losses at every element of the system that was damaged during an avalanche. The energy dissipated during the nth avalanche E_n is calculated as,

$$E_n = \sum_{damage\ events} (1-d_0)\frac{A_i}{2}\underline{\underline{\sigma}}_i : \underline{\underline{\epsilon}}_i \tag{3.5}$$

where d_0 is the damage parameter, A_i is the surface area of the ith element, $\underline{\underline{\sigma}}_i$ and $\underline{\underline{\epsilon}}_i$ are respectively the stress and strain tensors of the ith element (before damage), the sum runs over each damage event of the nth avalanche. This definition is equivalent to the *microscopic dissipated energy* defined by Picallo & Lopez (2008) for the RFM. The proximity to macroscopic failure is tracked in terms of a control parameter Δ defined as

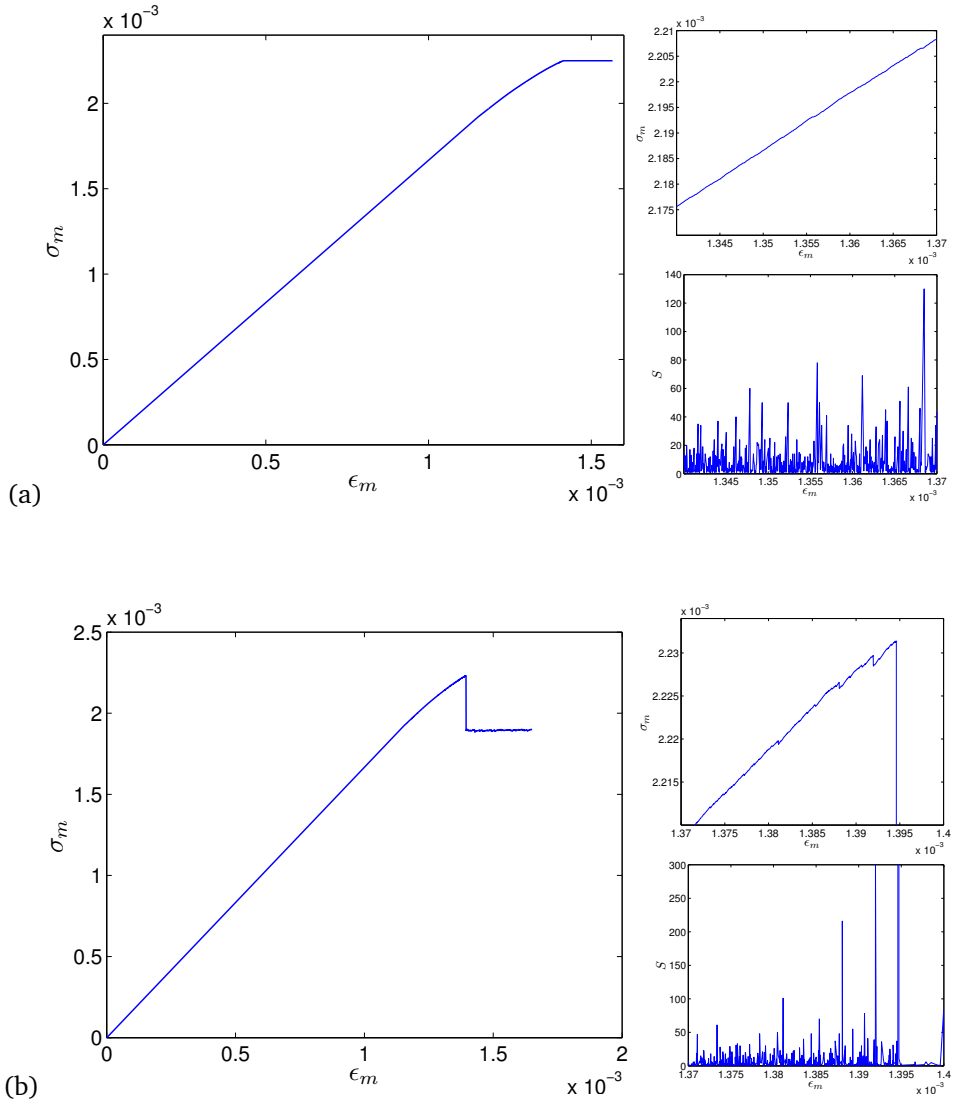

FIG. 3.1: Example of macroscopic strain σ_m versus stress ϵ_m, for (a) stress controlled simulation and (b) strain controlled simulation. The right panels are zooms of the macroscopic stress/strain curve and the avalanche size S record. σ_m is normalized by the Young's modulus.

$$\Delta = \frac{\sigma_{mp} - \sigma_m}{\sigma_{mp}}, \text{ for stress driven simulations} \tag{3.6}$$

$$\Delta = \frac{\epsilon_{mp} - \epsilon_m}{\epsilon_{mp}}, \text{ for strain driven simulations} \tag{3.7}$$

where σ_m and ϵ_m are respectively the macroscopic stress and strain, reaching values of σ_{mp} and ϵ_{mp} at peak load. The critical point is therefore identified as the peak load. As we are not interested in the linear elastic behavior that precedes the first damage event, σ_m and ϵ_m are set to zero when the first damage event occurs. The control parameter varies between $\Delta = 1$ at the first damage event and $\Delta = 0$ at the macroscopic failure.

3.3.1 Finite size scaling

Figure 3.3 shows the distributions of avalanche sizes S and dissipated energy E for various system sizes, for all damage events up to peak load ($1 \geq \Delta > 0$). The last catastrophic avalanche is out of trend and can thus be considered as an outlier. By analogy with the FBM and RFM, this last avalanche is most likely

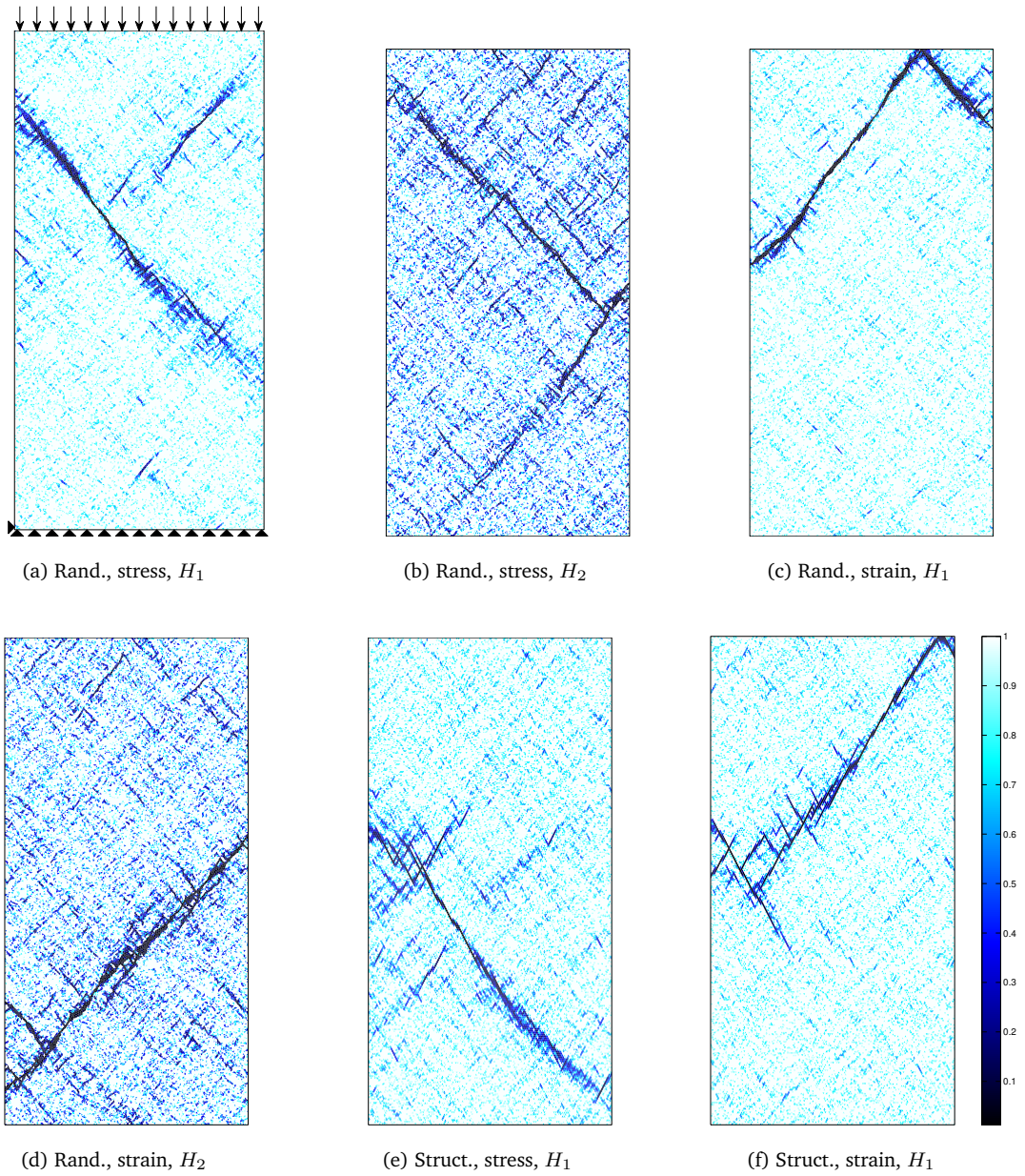

(a) Rand., stress, H_1 (b) Rand., stress, H_2 (c) Rand., strain, H_1

(d) Rand., strain, H_2 (e) Struct., stress, H_1 (f) Struct., strain, H_1

FIG. 3.2: Map of normalized Young's modulus after the catastrophic avalanche for both mesh types (random, structured), loading modes (stress and strain controlled) and heterogeneity range (H_1 and H_2-ranges).

of significantly different nature than the other avalanches (Zapperi *et al.*, 2005), and is not analyzed here. The probability density functions follow a power law with an exponential cut-off at large sizes/energies, sometimes referred to as a gamma law (Sornette & Andersen, 1998),

$$P(x) \sim x^{-\alpha_x} \exp(-x/x_0) \tag{3.8}$$

where $x = S$ or E. The cut-off size x_0 increases with the system size L. We make the hypothesis that this cut-off is the expression of a finite size scaling (FSS) and that it scales as $x_0 \sim L^{\delta_x}$. The moment analysis provides a powerful tool to test these scalings and extract the exponents α_x and δ_x (Chessa *et al.*, 1999). We define the q-moment of x on a system size L as $\langle x^q \rangle_L = \int x^q P(x) dx$. If the FSS hypothesis is valid, at least in the asymptotic limit ($x \to \infty$), we can transform $z = x/L^{\delta_x}$ and obtain

$$\langle x^q \rangle_L = L^{\delta_x(q+1-\alpha_x)} \int z^{q+\alpha_x} \exp(-z) dz. \tag{3.9}$$

For $q > \alpha_x - 1$, this can be approximated by $\langle x^q \rangle_L \sim L^{\chi_x(q)}$ where $\chi_x(q) = \delta_x(q + 1 - \alpha_x)$. The exponents $\chi_x(q)$ can be obtained as the slope of the log-log plot $\langle x^q \rangle_L$ $vs.$ L. Figure 3.4 shows the results obtained from the momentum analysis for $x = S$. As extensive statistical sampling is required to characterize the FSS, the largest system size $L = 128$ is not considered here. $\chi_S(q)$ as a function of q shows a clear linear variation starting from $q \approx 3$. For smaller q we observe deviations from the FSS because the integral of Eq. 3.9 is dominated by the lower cut-off for small q moments. The linear part of the function $\chi_x(q)$ is used to estimate the exponents δ_x and α_x from the relation $\chi_x(q) = \delta_x(q + 1 - \alpha_x)$, the results are presented in tables 3.2 and 3.3. To validate these results we perform a data collapse using the estimated value of the exponents. The representation of $P(x)L^{(\alpha_x - 1)\delta_x}$ as a function of x/L^{δ_x} shows a good collapse (figure 3.5). For a given variable (S or E), the exponents do not significantly vary with the mesh type or the loading mode. The range of material heterogeneity does not have a strong influence on the exponent values. The only significant difference concerns the value of α_E which is slightly lower for the H_2-range than for the H_1-range.

We examine the link between S and E by sorting avalanche sizes and energies in bins and averaging over all realizations of the disorder. We find a clear scaling relationship, $E \sim S^{\omega}$, with $\omega = 1.2 \pm 0.05$ which applies for both loading modes, mesh types and heterogeneity ranges (figure 3.6). From this, one would expect $\alpha_E = (\alpha_S + \omega - 1)/\omega$ and $\delta_E = \omega \times \delta_S$. These values are in slight disagreement with the energy exponents reported in table 3.2 and 3.3, especially regarding the cutoff exponent δ_E. These differences could be explained by the uncertainties.

The FSS exponent obtained with the two-dimensional RFM model is in the same range as the results we obtain for δ_S ($\delta = 1.17$ to 1.18 (Zapperi *et al.*, 2005)). The power law exponents α_S obtained with our model are also in the same range as those obtained with the RFM ($\alpha = 2.75$ with a diamond lattice, and $\alpha = 3.05$ with a triangular lattice (Zapperi *et al.*, 2005)), or the RSM ($\alpha \approx 2.6$). This is in turn very close to the mean field value $5/2$ obtained in fiber bundle models. Thus, considering the avalanche statistics, the present model (true two-dimensional) does not differ very much from the pseudo-two-dimensional RSM (one-dimensional elements connected in two dimensions) and the one-dimensional RFM.

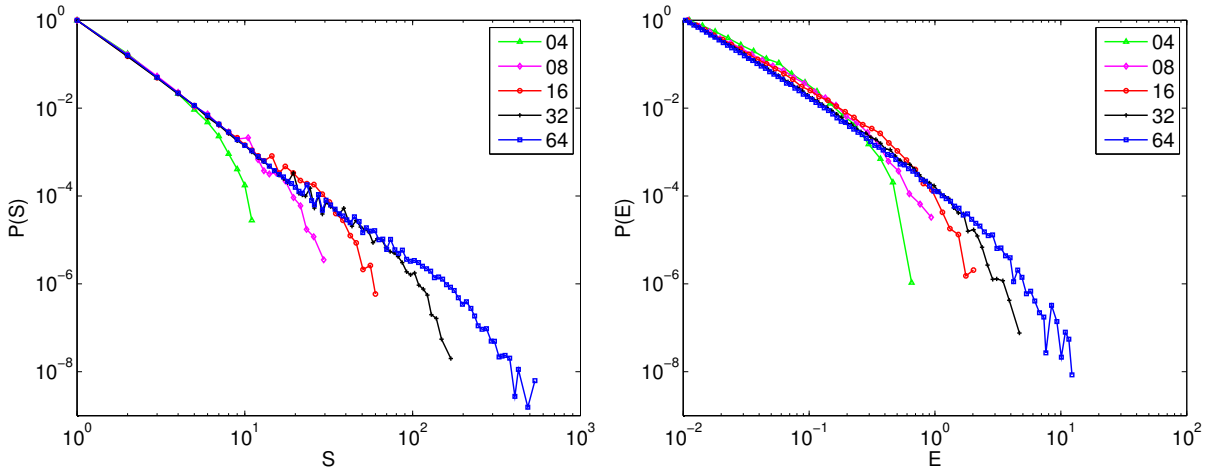

FIG. 3.3: Probability density functions of avalanche size and dissipated energy for the random mesh for strain controlled simulations (H_2-range). Distributions obtained with stress controlled conditions, a regular mesh and/or a narrower range of heterogeneity (H_1), have a similar shape. The functions are normalized by their maximum value.

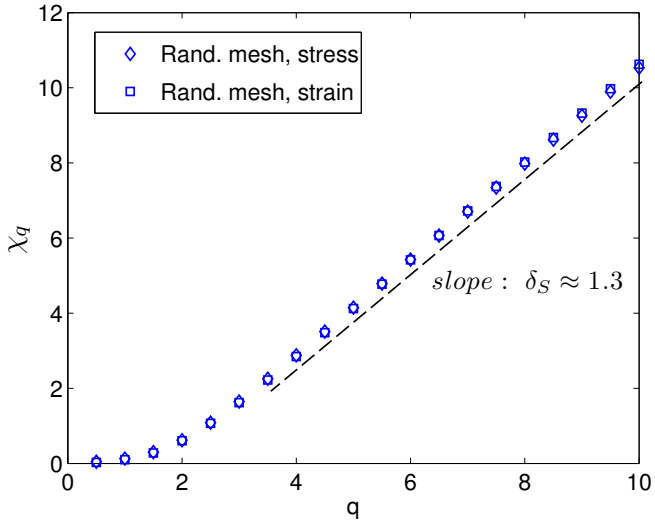

FIG. 3.4: The scaling exponent χ_q of the qth moment of the distribution of avalanche size S for the random mesh and both loading modes (H_2-range). For $q > 3$, a linear fit is applied to χ_q to estimate the values of α_S and δ_S (Eq. 3.9).

Loading	Stress		Strain		
Mesh type	Random	Structured	Random	Structured	
α_S	2.7	2.5	2.6	2.6	± 0.2
α_E	2.5	2.4	2.5	2.5	± 0.2
δ_S	1.2	1.1	1.2	1.3	± 0.2
δ_E	1.0	1.0	1.3	1.3	± 0.2
β_S	1.8	1.8	1.8	1.8	± 0.2
β_E	1.8	1.8	1.9	1.9	± 0.2
γ_S	2.0	2.0	2.0	2.0	± 0.5
γ_E	2.0	2.0	2.0	2.0	± 0.5
D	1.15	1.15	1.15	1.20	± 0.05
η	1.1	1.1	1.1	1.2	± 0.1
λ	1.0	1.0	1.0	1.0	± 0.1
$\rho(1)$	0.15	0.15	0.15	0.16	± 0.02
ν	1.0	0.9	1.0	1.0	± 0.1

TAB. 3.2: Exponent values for the avalanche distributions, the spatial correlations of damage and the spatial dependance of the strain-rate field for the H_1-range.

Loading	Stress	Strain	
α_S	2.6	2.7	± 0.2
α_E	2.1	2.1	± 0.2
δ_S	1.3	1.4	± 0.2
δ_E	1.2	1.2	± 0.2
β_S	1.9	1.9	± 0.2
β_E	1.9	1.8	± 0.2
γ_S	2.0	2.0	± 0.5
γ_E	2.0	2.0	± 0.5
D	1.3	1.4	± 0.1
η	1.1	1.1	± 0.1
λ	1.0	1.0	± 0.2
$\rho(1)$	0.15	0.15	± 0.02
ν	1.0	1.0	± 0.1

TAB. 3.3: Exponent values for the H_2-range.

3.3.2 Distributions

We now consider the distribution of avalanche sizes and energies for different values of the control parameter Δ. This analysis is done by sorting out avalanches from several realizations of the disorder in log-spaced bins of Δ. We then compute the distribution of each bin (figure 3.7). The distribution follows a gamma law,

$$P(x, \Delta) \sim x^{-\beta_x} \exp(-x/x^*) \tag{3.10}$$

where $x = S$ or E. The cut-off sizes x^* increases with Δ and with the system size L. β_x is estimated so that Eq. 3.10 fits the distribution of the bin closest to macroscopic failure (table 3.2 and 3.3). Using the methodology of Eq. 3.9, we show that the second moment of the distribution scales as $\langle x^2 \rangle \approx (x^*)^{3-\beta_x}$. Following Zapperi *et al.* (2005), we assume that for infinitely large systems $x^* \sim \Delta^{-\gamma_x}$ so that we can expect

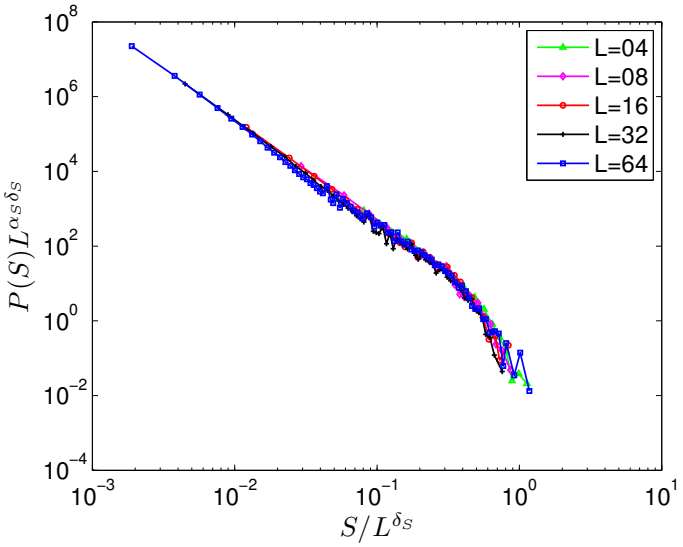

FIG. 3.5: Data collapse of the distributions of avalanche size S for the random mesh under strain control, $\alpha_S = 2.8$ and $\delta_S = 1.3$ (H_2-range).

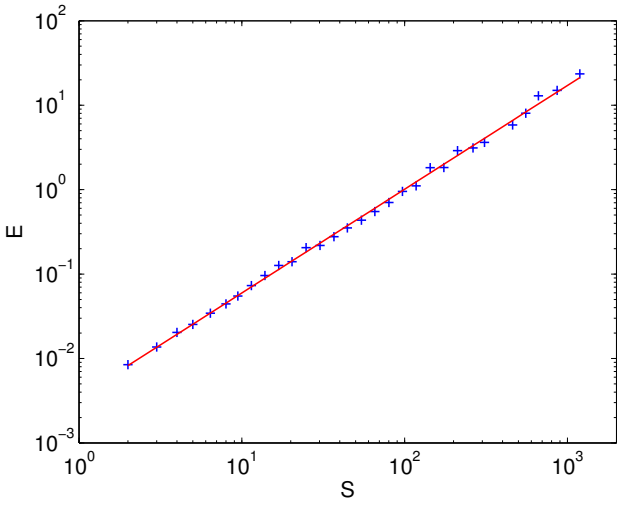

FIG. 3.6: Scaling relationship between the avalanche size S and the dissipated energy E (Random mesh under strain control, $L = 64$, H_2-range), the red line is a power law fit $E \sim S^{1.2}$.

the singularity to be rounded at small L as

$$x^* \sim \frac{L^{\delta_x}}{\Delta^{\gamma_x} L^{\delta_x} + c} \tag{3.11}$$

where c is a constant. The value of γ_x is estimated in order to allow the collapse of $\langle x^2 \rangle$ (figure 3.8).

The exponents for S and E are within the same range. As for α_x and δ_x one would have expected instead slight differences, owing to the $E \sim S^{\omega}$ scaling. The exponents β and γ do not vary with the type of mesh or the loading mode. The divergence of the maximum avalanche size towards the critical point is the same under stress and strain control. The range of material heterogeneity does not significantly affect this divergence, as the value of γ remains similar for H_1 and H_2-ranges. A detailed comparaison of avalanche size and energy distributions shows that the divergence of the largest avalanche is actually slightly less abrupt for the H_2-range. This expresses that a broader heterogeneity range increases the number of precursors. Nevertheless the effect is to small to significantly impact the value of the critical exponent γ_S. In comparison, simulations with the RFM indicated a similar β but a smaller value of γ ($\gamma \approx 1.4$, (Zapperi *et al.*, 2005)). This means that the divergence of the maximum avalanche size as approaching final failure is more abrupt in our case.

Integrating Eq. 3.10 over Δ, described as sweeping the control parameter towards an instability (Sornette & Andersen, 1998), we obtain the theoretical relation : $\alpha_x = \beta_x + 1/\gamma_x$. This relation is compared to the estimated data. The worst comparison is for the random mesh under stress control (H_1-range), where $\beta_S + 1/\gamma_S = 2.3 \pm 0.5$ while $\alpha_S = 2.7 \pm 0.3$. The comparison improves for the other cases.

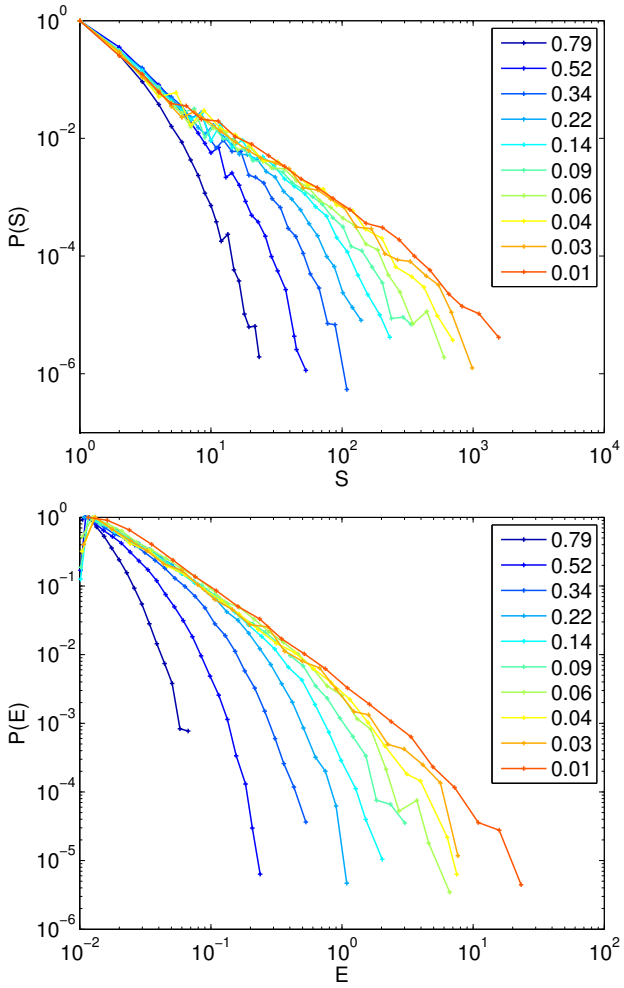

FIG. 3.7: Probability density functions of avalanche size and dissipated energy for different bins of the control parameter, for the random mesh ($L = 128$) under strain control (H_2-range). Distributions obtained with stress controlled conditions, a regular mesh and/or a narrower range of heterogeneity (H_1), have a similar shape. The functions are normalized by their maximum value.

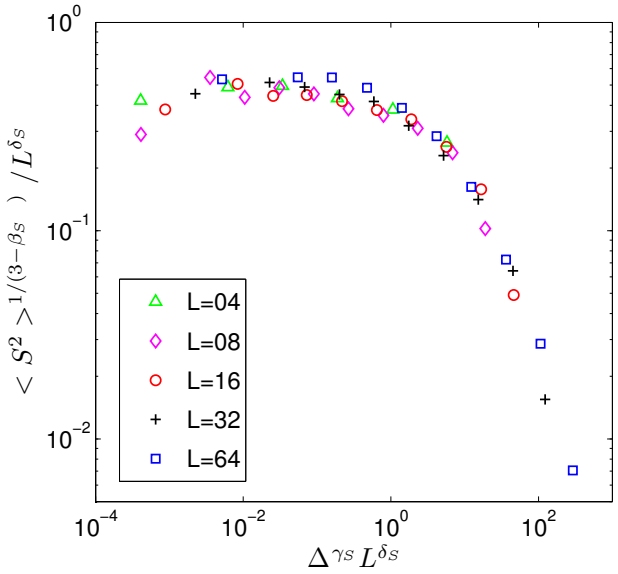

FIG. 3.8: The second moment of the distribution of avalanche size S as a function of the control parameter for the random mesh under strain control can be collapsed using the exponents $\beta_S = 1.9$, $\delta_S = 1.4$ and $\gamma_S = 2.0$ (H_2-range).

3.3.3 Rate of dissipated energy

Avalanche activity can alternatively be tracked by the evolution of the energy release rate. We define the energy release rate $dE/d\Delta$ as the energy dissipated by damage over windows of Δ, normalized by the window width and averaged over different realizations of the disorder. $dE/d\Delta$ shows a steep increase at the start of the simulation bending towards a shallower slope in the vicinity of the macroscopic failure (figure 3.9). Below $\Delta = 10^{-2}$ the evolution becomes very fluctuating due to a lack of data.

As $dE/d\Delta$ simply scales as the mean dissipated energy $\langle E \rangle$ in our case, we relate its evolution to the distribution of E. This relation owes to the fact that an avalanche is triggered at every loading step, so that the number of avalanches per window of Δ, normalized by the window width, is constant. The spatial discretisation of the numerical model imposes the existence of a lower bound in the distribution of dissipated energy. In the early stage of the simulation, the cutoff term E^* is close to this lower bound. This introduces an artefact in the estimation of $\langle E \rangle$, and can explain the steep increase of $dE/d\Delta$ at the begining of the simulation, which has therefore no physical significance. In the vicinity of the macroscopic failure, an estimation of the mean dissipated energy $\langle E \rangle$ can be obtained from the probability density function of E, assuming a brutal truncation at E^* :

$$\langle E \rangle_{(\Delta \to 0)} \sim \int_0^{E^*} E^{1-\beta} dE \sim {E^*}^{2-\beta}. \tag{3.12}$$

Neglecting the finite size effect, we can therefore approximate the evolution of the mean dissipated energy by $\langle E \rangle_{(\Delta \to 0)} \sim \Delta^{-\gamma(2-\beta)}$ (a similar relation was obtained for the average avalanche size in ferromagnets (Zapperi *et al.*, 1998)). Typical values of the exponents (table 3.2) suggest generally a very shallow evolution of $\langle E \rangle$ near the macroscopic failure. For example, considering the random mesh under stress control (H_2-range of heterogeneity), $\gamma_E(2 - \beta_E) \simeq 0.2 \pm 0.7$. This estimation commensurates with the shallow increase of $dE/d\Delta$ near the macroscopic failure (figure 3.9). For $\Delta < 10^{-2}$ the slope can be roughly approximated to 0.4. However, despite extensive statistical sampling, the power law behavior and the slope expected to characterize the evolution of $dE/d\Delta$ in the vicinity of the macroscopic failure cannot be clearly assessed. The range of material heterogeneity does not affect the evolution of $dE/d\Delta$. No significant difference was observed between stress and strain control modes.

3.4 Spatial correlations of damage events

In this section we analyze the spatial distribution of damage using the two point correlation function. For a population of $\mathcal{N}$ damage events, the correlation integral is defined as $C_2(r) = 2.\mathcal{N}_p(r)/\left[\mathcal{N}(\mathcal{N}-1)\right]$,where $\mathcal{N}_p(r)$ is the number of pair of points whose distance is less than r (Hentschel & Proccacia, 1984). For a fractal population of elements, $C_2(r)$ is expected to scale with r such as r^D, where D is the correlation dimension of the system. The distance r is expressed with the same units as the system size L.

3.4.1 Finite size scaling

We first analyze the correlation function in the vicinity of the macroscopic failure ($0 < \Delta < 10^{-2}$). We calculate the correlation integral of damage events corresponding to this criterion and average it over all realizations of the disorder for system sizes $L \geq 8$. The form of the correlation function obtained is a power law with a cross-over at large r values (figure 3.10),

$$C_2(r) \sim r^D \mathcal{F}(r/r_0) \tag{3.13}$$

where D is the correlation dimension of damage events and the function $\mathcal{F}$ describes the cross-over occuring at r_0 so that $\mathcal{F}(r/r_0) \sim const$ for $r \ll r_0$ and $\mathcal{F}(r/r_0) \sim r^{-D}$ for $r \gg r_0$. The cross-over length r_0 increases with the system size L. We assume that it expresses a finite size effect and scales as $r_0 \sim L^\eta$. To test this scaling and estimate the value of η we perform a data collapse (figure 3.10). The estimated values for the exponents are given in table 3.2. The values of D and η are not significantly affected by the loading mode or the mesh type. Both values are very close to 1 for the H_1-range of heterogeneity, arguing for a spatial distribution of damage over quasi-linear structures, the faults. On the other hand, the H_2-range leads to slightly larger values of the correlation dimension D (table 3.3). This suggests that increasing the heterogeneity leads to a more isotropic interaction of damage events and more branchy fault geometries (see fig. 3.2).

3.4.2 Evolution of the correlation length

We analyze the evolution of spatial correlations of damage with the control parameter Δ. In order to do so, we divide each simulation in intervals containing a similar number of damage events. For each interval, the mean control parameter and the correlation integral corresponding to the population of damage events are calculated. The correlation integrals are sorted in bins of the mean control parameter and averaged over disorder. In the early stages of the simulation, there appear to be two different scaling regimes (figure 3.11). For small values of r, the correlation integrals scale as r^D. This scaling extends up to a cross-over length, which we refer to as the correlation length ξ. Beyond the correlation length, the scaling exponent of integrals raises to 2, which corresponds to an homogenous unclustered damage pattern. Finally, a second cross-over occurs and the integrals bend down due to the finite size scaling described in the previous subsection. This evolution is best seen when renormalizing the integrals by the integral closest to the peak load (figure 3.12).

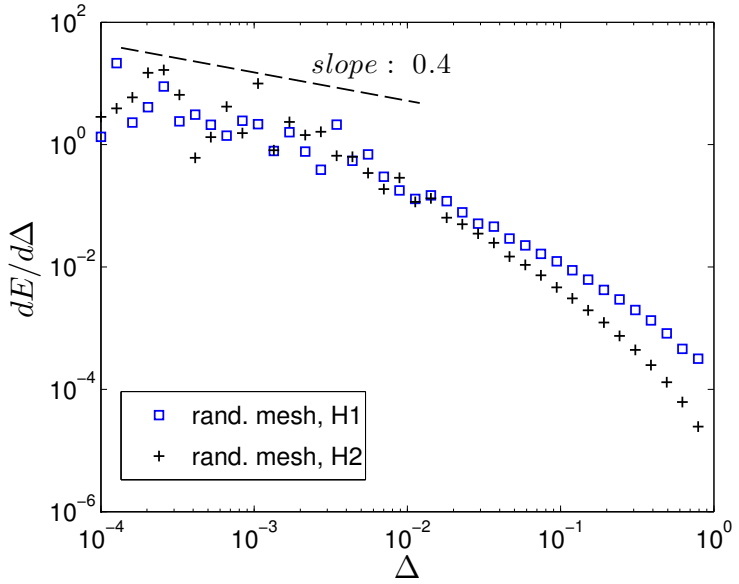

FIG. 3.9: Rate of dissipated energy as a function of the control parameter for the random mesh under strain control, $L = 64$, for H_1 and H_2 ranges of heterogeneity. The slope is given as guideline to support the explanations, it was obtained by fitting a power law to the data for $\Delta < 10^{-2}$.

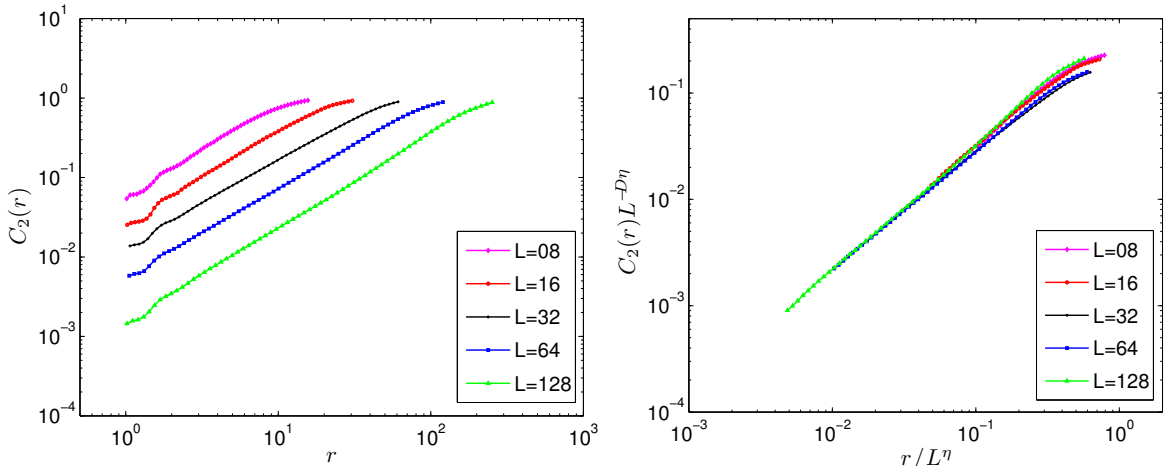

(a) (b)

FIG. 3.10: (a) The correlation integral $C_2(r)$ of damage events near peak load ($\Delta < 10^{-2}$) for different system sizes, for the random mesh under strain control (H_1-range). (b) Data collapse analysis of the correlation integrals, the values used for the exponents are $D = 1.15$ and $\eta = 1.1$.

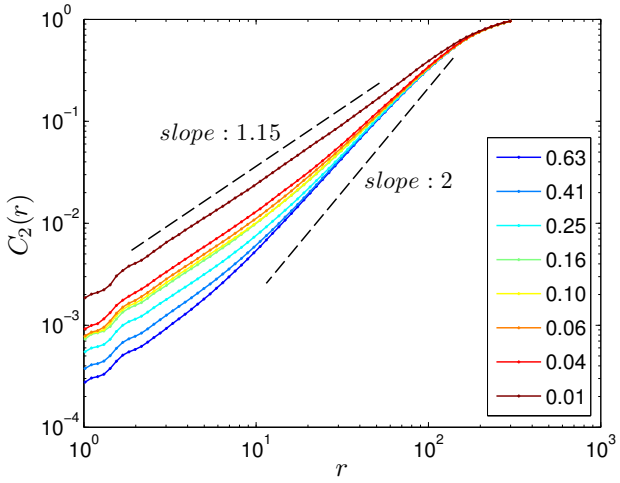

FIG. 3.11: Correlation integrals of damage events for the random mesh under strain control, $L = 128$ (H_1-range), for different values of the control parameter Δ.

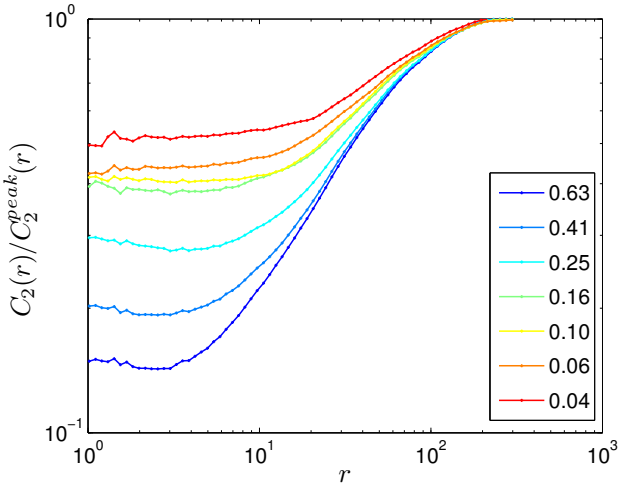

FIG. 3.12: Correlation integrals normalized by the peak load integral (random mesh under strain control, $L = 128$, H_1-range).

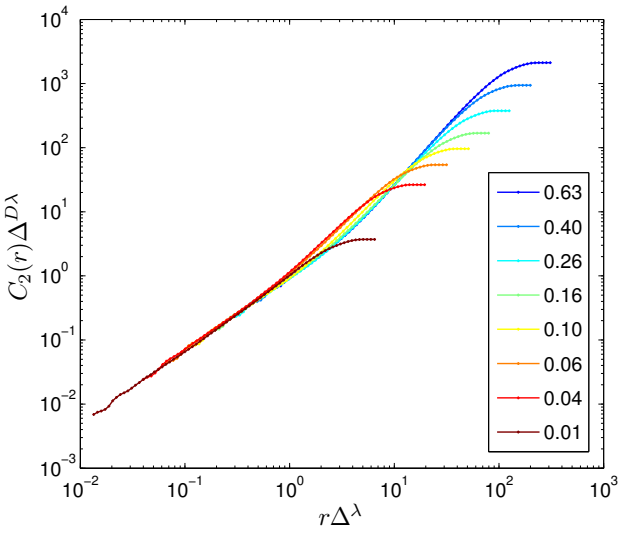

FIG. 3.13: Data collapse analysis of the correlation integral $C_2(r)$ for the random mesh under strain control ($L = 128$, H_1-range). The values used for the exponents are $D = 1.15$ and $\lambda = 1.0$.

The evolution of spatial correlations of damage can thus be seen as a divergence of the correlation length ξ as approaching $\Delta = 0$.

$$C_2(r, \Delta) \sim r^D \mathcal{G}(r/\xi) \tag{3.14}$$

where ξ is expected to grow as $\xi \sim \Delta^{-\lambda}$. The function $\mathcal{G}$ describes the first cross-over, occuring at ξ, so that $\mathcal{G}(r/\xi) \sim const$ for $r \ll \xi$ and $\mathcal{G}(r/\xi) \sim r^{2-D}$ for $r \gg \xi$. The second cross-over, due to the FSS is not accounted for here. We test this hypothesis and estimate the value of λ with a data collapse analysis (figure 3.13). As the FSS is neglected in Eq. 3.14, only the part of the integrals that are not affected by the FSS can be expected to collapse. A good collapse is obtained for $\lambda = 1.0$ (table 3.2,3.3). As for avalanches, the critical exponent λ is found to be similar for the stress and strain loading modes and does neither vary significantly with the mesh type nor with the heterogeneity. Therefore, the correlation length diverges as $1/\Delta$ as approaching the peak load. This value of the critical exponent is slightly smaller than the corresponding value obtained for two-dimensional geometrical percolation $(4/3)$ (e.g. (Stauffer & Aharony, 1994)), meaning that the elastic interactions imply a less abrupt divergence of the correlation length near the critical point.

3.5 Spatial dependance of the strain-rate field

Strain rates are computed over a broad range of spatial scales for different values of the control parameter Δ through the following procedure. Each simulation is divided in intervals containing a similar number of damage events. We compute the rate of displacement (u, v) as the difference between displacement at the beginning and the end of each interval. The spatial gradients of the displacement-rate (or strain-rate tensor components) $\partial u/\partial x$, $\partial v/\partial x$, $\partial u/\partial y$, $\partial v/\partial y$ are calculated. We then consider the invariants of the strain-rate tensor,

$$\dot{\epsilon}_{div} = \frac{\partial u}{\partial x} + \frac{\partial v}{\partial y} \tag{3.15}$$

$$\dot{\epsilon}_{shear} = \left[\left(\frac{\partial u}{\partial x} - \frac{\partial v}{\partial y} \right)^2 + \left(\frac{\partial u}{\partial y} + \frac{\partial v}{\partial x} \right)^2 \right]^{1/2} \tag{3.16}$$

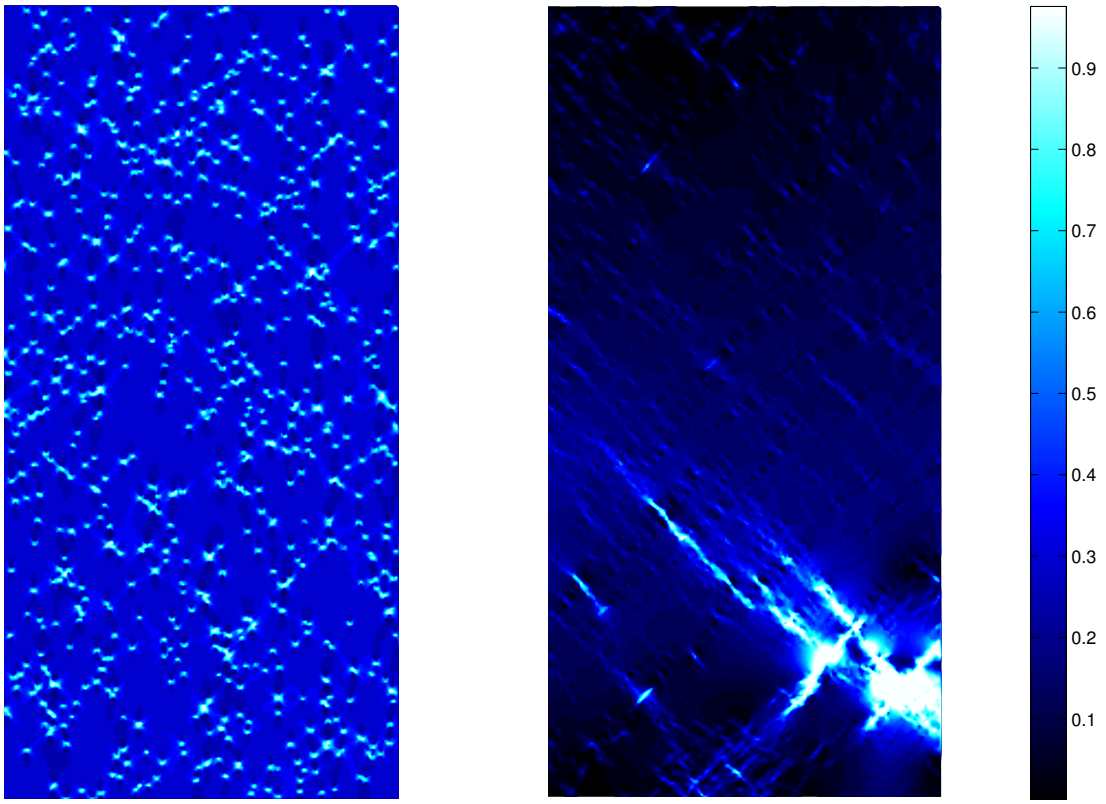

FIG. 3.14: Examples of total deformation rate fields $\dot{\epsilon}$ for $\Delta \simeq 0.9$ (left panel) and $\Delta \simeq 0.01$ (right panel), for the random mesh under strain control (H_1-range, $L = 128$). $\dot{\epsilon}$ is normalized by its maximum value.

where $\dot{\epsilon}_{div}$ and $\dot{\epsilon}_{shear}$ are respectively the divergence and shear rates. Henceforth the term deformation means the quantity $\dot{\epsilon} = \sqrt{\dot{\epsilon}^2_{shear} + \dot{\epsilon}^2_{div}}$, also known as the total deformation rate. Deformation at the finite element scale, the smallest scale, is first computed. At larger spatial scales deformation is obtained by a coarse graining procedure. Consider a square box of with W centered at a certain location within the mesh. We find all the element centers that lie inside the box and compute the average displacement-rate gradients over all the corresponding elements, where the contribution of each element is weighted by its area. From these large-scale gradients we compute the deformation rates $\dot{\epsilon}$. Assuming scaling isotropy, we define the spatial scale l as the square root of the actual area covered by the elements (which is close to W^2). By changing the size of the box we obtain samples of the deformation at different scales. Deformation is binned with respect to spatial scale and control parameter and averaged over different realizations of the disorder. This procedure can only be applied to large systems ($L \geq 32$) where a wide range of scales can be covered.

In the early stages of the simulation, deformation is homogeneously scattered throughout the system, while near macroscopic failure, it is extremely heterogeneous and localized along linear features (figure 3.14). The mean total deformation $\langle\dot{\epsilon}\rangle$ is plotted as a function of the spatial scale l and the control parameter Δ (figure 3.15). $\langle\dot{\epsilon}\rangle$ shows a power law decrease with increasing l up to a given cross-over scale.

$$\langle\dot{\epsilon}\rangle(l, \Delta) \sim l^{-\rho}\mathcal{H}(l/l^*), \tag{3.17}$$

where l^* is the cross-over scale that increases as approaching the macroscopic failure. The function $\mathcal{H}$ describes the cross-over, it is thus constrained by $\mathcal{H}(l/l^*) \sim const$ for $l \ll l^*$ and $\mathcal{H}(l/l^*) \sim l^{\rho}$ for $l \gg l^*$. In order to investigate the possible influence of a finite size effect on the cross-over, we analyzed deformation near peak load ($\Delta \leq 10^{-2}$) for various system sizes. No dependance of the cross-over on the system size

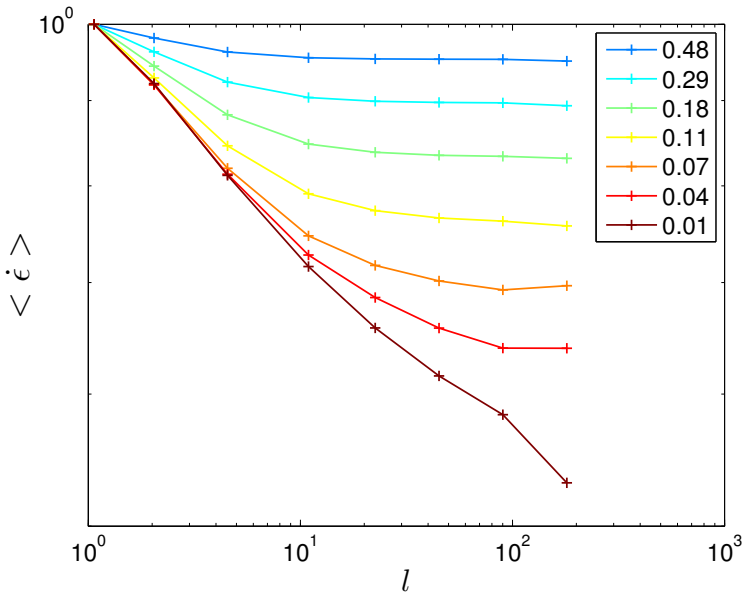

FIG. 3.15: Mean total deformation rate as a function of the spatial scale l and of the control parameter Δ, for the random mesh under strain control (H_1-range, $L = 128$). Deformation rates are normalized at scale $l = 1$.

was found, we are therefore unable to characterize properly a finite size effect. The fact that the finite size effect is not noticeable might be related to the boundary conditions applied to the model, since the lateral boundaries of the model can deform freely.

To test the scaling of Eq. 3.17, we thus neglect the finite size effect and hypothesize that l^* grows as $l^* \sim \Delta^{-\nu}$. The exponent values are estimated through a data collapse analysis (figure 3.16). $\rho = 0.15 \pm 0.02$ and $\nu = 1.0 \pm 0.1$ allow the best collapse independently of the loading mode, the mesh type or the range of material heterogeneity (table 3.2 and 3.3). Small deviations of the data collapse are found in the vicinity of the final failure. These deviations might be due to a finite size effect which was neglected. The striking agreement between the values of λ and ν argues for the interpretation of l^* as a correlation length, $l^* \sim \xi$. This results bridges the two different ways to analyze the deformation resulting from damage and fracturing, from the discrete approach (through correlation analysis of individual events) to the continuous one (the scaling analysis of the resulting strain field).

As done for an analysis of Arctic sea ice deformation (Marsan *et al.*, 2004), the scale-dependant heterogeneity of deformation is examined more thoroughly by use of a multifractal analysis which characterizes the scaling of the moments $\langle \dot{\epsilon}^q \rangle$ for $0 < q < 3$. This moment analysis is a way to investigate the scale dependance of the entire distribution of $\dot{\epsilon}$. Generalizing Eq. 3.17, we estimate the scaling exponents $\rho(q)$ and the critical exponents $\nu(q)$ by data collapse analysis (figure 3.17). $\nu = 1$ is found to be constant, independently of the moment order, as one would expect for a correlation length, while $\rho(q)$ shows a curvature indicating the multifractality of the deformation (figure 3.18). The multifractality is a well-known property of turbulent flow of fluids (e.g. (Frisch, 1995)). It is observed here to also arise from long-range elastic interactions in a deforming solid. It means that deformation becomes more and more localized as one decreases the scale of observation.

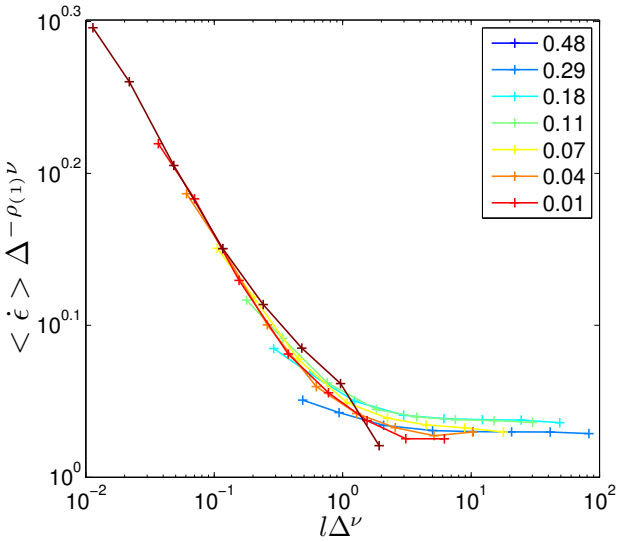

FIG. 3.16: Data collapse analysis of the mean total deformation rate for the random mesh under strain control (H_1-range, $L = 128$). The values used for the exponents are $\rho = 0.15$ and $\nu = 1.0$.

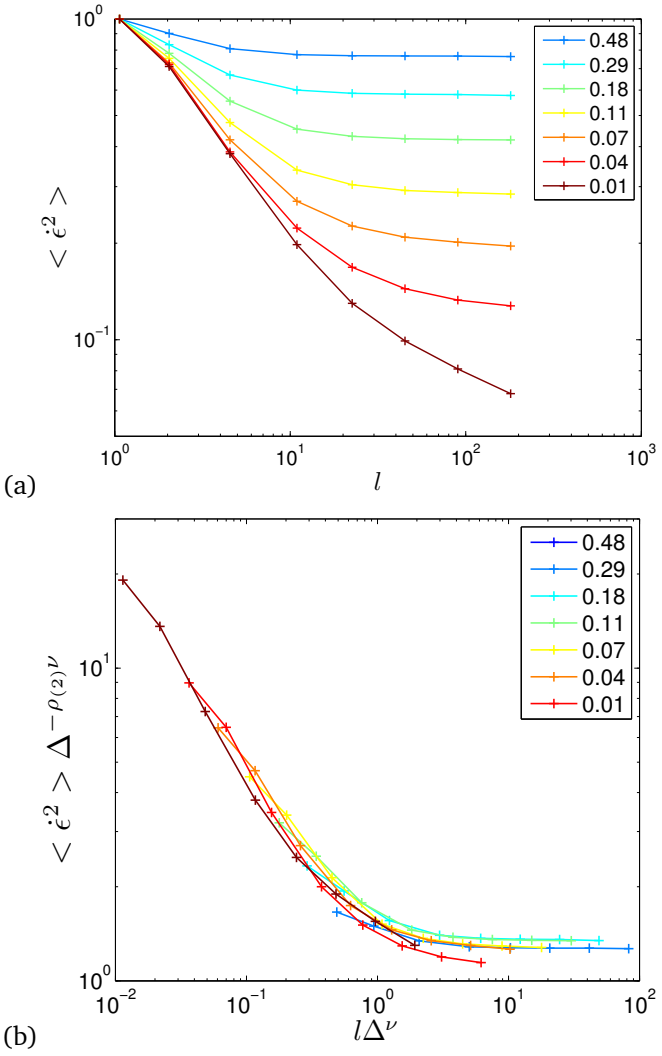

FIG. 3.17: (a) Second moment of deformation $\langle \epsilon^2 \rangle$ as a function of the spatial scale l and of the control parameter Δ. (b) The second moment can be collapsed with the exponents $\rho = 0.65$, $\nu = 1.0$. (random mesh under strain control, H_1-range, $L = 128$)

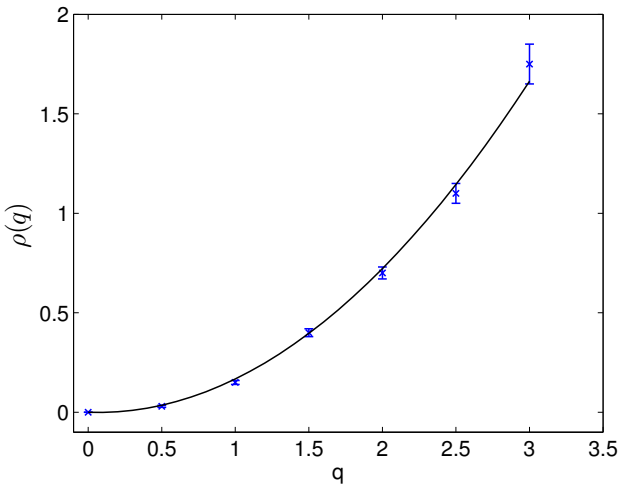

FIG. 3.18: The function $\rho(q)$ versus moment order q (random mesh under strain control, H_1-range, $L = 128$). The exponents $\rho(q)$ are determined by datacollapse analysis. The black line is a quadratic fit $\rho(q) = aq^2 + bq$ where $a = 0.19$ and $b = -0.026$.

3.6 Discussion

3.6.1 Failure as a critical phenomenon

As noted in the introduction, the interpretation of failure as a critical phenomenon (Sornette & Andersen, 1998) is still partly controversial (Alava *et al.*, 2006; Picallo & Lopez, 2008). Following on from discrete statistical models of fracture, such as the RFM, our continuum progressive damage model argues for such critical point interpretation of failure. The advantage of the present model based on a continuum mechanics framework is the possibility to track criticality from the evolution of the strain field. In terms of damage avalanches, power law distributions of avalanche sizes and energies are observed, associated to a finite size scaling. This finite size scaling, which is also observed for the spatial correlations of the damage events, argues for this critical point interpretation.

Another strong argument is the divergence of the correlation length as approaching macroscopic failure, $\xi \sim 1/\Delta$, which can be seen from a correlation analysis of discrete events (section 3.4.2) or from a scaling analysis of the continuous strain-rate field (section 3.5). Qualitatively, this is also in agreement with the divergence of the avalanche cut-off (section 3.3.2). However, one would expect this correlation length to be related to the avalanche cut-off size through the geometrical relation $S^* \sim \xi^D$. This is not really consistent with the value found for the critical exponent γ_S as it yields $\xi \sim \Delta^{-\gamma_S/\delta_S}$, with $\gamma_S/D = 1.7$ for the H_1-range, significantly larger than $\lambda = \nu = 1.0$. This comparison slightly improves for the H_2-range. This divergence of the correlation length can be interpreted as follows. At the early stages of deformation, when the spatial distribution of damage is imposed by the disorder, events are spread uniformly throughout the medium and are uncorrelated. As approaching the macroscopic failure (the critical point), i.e. as decreasing Δ, damage clusters appear as the result of elastic interactions, associated to a correlation length ξ. Within these clusters, damage is organized following a fractal pattern characterized by a fractal dimension D, which is independent of Δ, whereas there is no correlation between clusters. This means that damage and deformation can be homogenized for scales significantly larger than ξ, as shown by the scaling analysis of the strain-rate (figure 3.15). Consequently, homogenization is impossible at the critical point, as no characteristic scale can be defined.

An analysis of cluster size evolution was performed to complement this interpretation. We define the

cluster size C_S as the number of adjacent elements (i.e. elements with two common nodes) encountering one or more damage events over a given bin of Δ. The distribution function of cluster sizes follows a power law with an exponential cutoff at large sizes that diverges as approaching peak load,

$$P(C_S) \sim {C_S}^{-\Gamma} \exp(-C_S/C_S^*). \tag{3.18}$$

For example, with the random mesh ($L = 128$) under strain control and H_1-range of heterogeneity, we find $\Gamma = 1.8 \pm 0.1$ and $C_S^* \sim \Delta^{-\Theta}$ with $\Theta = 0.9 \pm 0.1$ by data collapse analysis. As the surface area of clusters is proportional to their size C_S, we obtain the geometrical relation $C_S^* \sim \xi^D$. In terms of exponents, this relation reads $\Theta = \lambda \times D$, which commensurates approximately with the exponent values. Moreover, we verified that cluster barycenters are not spatially correlated : the associated correlation dimension is close to 2, except in the vicinity of macroscopic failure where it slightly decreases due to the finite size effect.

This interpretation, based on the divergence of the correlation length, differs from previous studies, which proposed instead a decrease of the correlation dimension of damage patterns as approaching final failure (Hirata *et al.*, 1987; Cowie *et al.*, 1995; Amitrano, 2006). Similarly, it has been argued that a decrease of the power law exponent β of the avalanche sizes or energies could be a precursory phenomenon of failure (Amitrano *et al.*, 2005). From our results and previous work (Zapperi *et al.*, 2005), we argue instead for a β-value independent of Δ but a diverging cut-off. For poorly statistically constrained distributions, this can lead to an artificial decrease of the « apparent » power law exponent as raised by Amitrano *et al.* (2005).

As approaching the critical point, the damage clusters length approaches the system size, and finite size scaling ensues. The close agreement between the values of the finite size exponents δ_S and η, and the correlation dimension D, is in agreement with the fact that damage avalanches (faults) are characterized by the same fractal structure whatever their size, the vicinity to final failure, or the size of the system. Finally, we stress that none of the exponents shows significant variation with the type of mesh or the loading mode, considering the level of uncertainty. Regarding the influence of the loading mode, our results contradict some of the conclusions of Guarino *et al.* (1998). Changing the range of material heterogeneity slightly affected the value the correlation dimention D but it did not have a significant effect on the other exponents.

3.6.2 Criticality of fracture and deformation of geophysical objects, and precursory phenomena

The scaling properties characterizing damage and deformation near the critical point resembles those reported for the deformation and fracturing of geophysical objects such as the Earth's crust or the sea ice cover. The possible critical character of Earth's crust deformation and fracturing is a long-standing problem (e.g. (Sornette & Sornette, 1989)), and still an active field of research. A thorough review of this problem is out of the scope of this paper. In light of the results presented in previous sections, we discuss here only several specific aspects.

The power law distribution of earthquake sizes or energies is well known (Gutenberg & Richter, 1954), generally without cut-off, although truncated distributions have been reported (Burroughs & Tebbens, 2002) and interpreted as a sub-critical state of the crust at a regional scale (e.g. (Main, 1996)). Fractal clustering of hypocenters has been reported from correlation analyses similar to that discussed in section 3.4 (Kagan & Knopoff, 1980; Kagan, 2007), however without a cross-over scale as shown on Figure 3.11. The strain localisation of the Arctic sea ice cover, characterized from a continuous approach (strain-rate fields), closely resembles the behavior detailed in section 3.5 near the critical point : the mean total strain rate scales as $\langle \dot{\epsilon} \rangle \sim l^{-\rho}$ with $\rho = 0.20 \pm 0.05$, and is associated with a multifractal scaling (Stern & Lindsay, 2009; Marsan

et al., 2004). At the time scale of the analysis (3 days), no cut-off scale was detected.

The agreement between the scaling properties of the present model near the critical point and those associated to the deformation and fracturing of geophysical objects, as well as the absence of obvious cut-off or cross-over scales in this last case, suggest that these objects remain most of the time near criticality, in a « marginally stable state » (Main, 1996). However, as stressed in the introduction, attempts have been done to export the critical point concept and the associated precursory phenomena to crustal deformation in order to predict « large » earthquakes. The underlying hypothesis is that, instead of remaining near criticality, crustal deformation is characterized at the regional scale by successive « large » earthquakes (failures), each of them being considered as a critical point with associated precursory phenomena. These large earthquakes are assumed to release the stresses in their surrounding region, moving it away from criticality until tectonic loading progressively re-establish the route towards the next critical point (Jaume & Sykes, 1999). One difficulty with such approaches is the definition of the appropriate space and time windows over which the analysis should be performed, and what « large » earthquake means as the system never falls apart.

The critical behavior of the model presented in this study is not affected by the loading mode, as long as the control parameter is correctly defined. In the case of geophysical objects, the loading conditions may be hard to identify and depend on the situation. Cliff collapses or landslides are driven by constant stress loadings, while for volcanoes the pressure increase in the magma chamber causes the stress to increase. Regarding geological faults, the loading is generally a complex mixture between strain and stress depending on the tectonic conditions, strain being the only parameter reachable by field measurements. In such cases the control parameter is usually from a time scale.

The most discussed precursory phenomenon is a divergence of the so-called Benioff strain ϵ_B as approaching a large earthquake (Bufe & Varnes, 1993; Bowman *et al.*, 1998; Jaume & Sykes, 1999; Hardebeck *et al.*, 2008) :

$$\epsilon_B(t) = \sum_{i=1}^{N(t)} \sqrt{E_i(t)} = A - B(t_c - t)^m \tag{3.19}$$

where E_i is the seismic energy of the ith event, $N(t)$ the cumulative number of events since an initial time (to be defined), t_c the arrival time of the large earthquake, $A = \epsilon_B(t = t_c)$, $B = A/{t_c}^m$, and m a critical exponent generally considered to be close to 0.3. Recast in terms of strain-rate and control parameter $\Delta = (t_c - t)/t_c$, this reads $d\epsilon_B/d\Delta \sim \Delta^{m-1} \approx \Delta^{-0.7}$. This increase of the Benioff strain-rate (or of energy release rate) before the critical point can result from (i) an increase of the earthquake occurrence rate and/or (ii) from an increase of the mean energy $\langle E \rangle$, as in section 3.3.3. Analyzing regional seismicity before several large earthquakes in California and Alaska, Jaume & Sykes (1999) argued that factor (i) is generally not observed, whereas factor (ii) is more likely and is associated to a diverging cut-off size (or energy) as approaching the large earthquake. Using a methodology similar to that detailed in section 3.3.3, a possible link between a diverging cut-off strain ϵ_B^* (or energy E^*) and a diverging Benioff strain-rate can be discussed. If the earthquake occurrence rate remains constant, we have :

$$\frac{d\epsilon_B}{dt}_{(\Delta \to 0)} \sim \left\langle E^{1/2} \right\rangle_{(\Delta \to 0)} \sim \int_0^{E^*} P(E) E^{1/2} dE \sim {E^*}^{\frac{3}{2}-\beta} \sim {\epsilon_B^*}^{3-2\beta}, \tag{3.20}$$

the above integral being only defined if the power law exponent of the seismic energy $\beta < 3/2$. In such case, Eq. 3.20 would lead to the scaling relation $d\epsilon_B/d\Delta \sim \Delta^{-\frac{\gamma}{2}(3-2\beta)}$. For $\beta > 3/2$, the integral of Eq. 3.20 is no longer defined. In this case the Benioff strain-rate is controlled by the smallest earthquakes and by a lower cut-off in the distribution of seismic energy. A b-value (power law exponent of the cumulative distribution

of earthquake magnitudes) around 1, as generally reported, yields $\beta \approx 5/3$ (Kanamori, 1978). This means that the evolution of the Benioff strain-rate towards $\Delta = 0$ is either extremely shallow, or very difficult to estimate. This might explain why a possible divergence of the Benioff strain-rate before large earthquakes remains highly controversial (Hardebeck *et al.*, 2008).

Zoller *et al.* (2001) have proposed another precursory phenomenon, the divergence of the correlation length ξ. To estimate ξ from a seismic catalog, they did not performed a correlation analysis such as the one described in section 3.4, but instead used a more complex iterative procedure, the single-link cluster analysis (Frohlich & Davis, 1990). They claimed that at least some large Californian earthquakes were preceded by a divergence of ξ, with an exponent λ varying from 0.24 to 0.57, i.e. a divergence much less abrupt than the one observed with the present model ($\lambda = 1$). However, within a critical point framework, critical exponents should be robust and not vary from one case to another.

In conclusion, although the scaling laws describing the deformation of geophysical objects share obvious features with what is observed near the critical point in statistical models of fracture (including the present one), we wonder to what extent such models based on irreversible damage are relevant for crustal or sea ice deformation. One important lacking ingredient is, we believe, the presence of recovery (healing) mechanisms that would compensate for increasing damage.

Acknowledgments

All (or most of) the computations presented in this paper were performed at the Service Commun de Calcul Intensif de l'Observatoire de Grenoble (SCCI-CIMENT). L. Girard is supported by a BDI phD grant from CNRS. D. Amitrano thanks French program INSU-Catell and EU program Trigs for support.

Chapitre 4

Première application d'une rhéologie elasto-fragile à la banquise Arctique

D'après :
Girard, L., S. Bouillon, J. Weiss, D. Amitrano, T. Fichefet, V. Legat (2010), A new modeling framework for sea ice models based on elasto-brittle rheology, *Annals of Glaciology*, *57*, 57A034.

Abstract

We present a new modeling framework for sea ice mechanics based on elasto-brittle (EB) behavior. The EB framework considers sea ice as a continuous elastic plate encountering progressive damage, simulating the opening of cracks and leads. As a result of long-range elastic interactions, the stress relaxation following a damage event can induce an avalanche of damage. Damage propagates in narrow linear features, resulting in a very heterogeneous strain field. Idealized simulations of the Arctic sea ice cover are analyzed in terms of ice strain-rates and contrasted to observations and simulations performed with the classical Viscous Plastic (VP) rheology. The statistical and scaling properties of ice strain-rates are used as the evaluation metric. We show that the EB simulations give a good representation of the shear faulting mechanism that accommodates most of sea ice deformation. The distributions of strain-rates and the scaling laws of ice deformation are well captured by the EB framework, which is not the case for VP simulations. These results argue that the properties of ice deformation emerge from the elasto-brittle ice mechanical behavior and motivate the implementation of the EB framework in a global sea ice model.

4.1 Introduction

Sea ice deformation is a fascinating component of the Arctic geophysical environnement which is of critical importance in climate modeling. The deformation of dense pack ice is accommodated by a network of quasi-linear fractures and faults, occuring over a wide range of scales, up to several hundred kilometers, resulting in an heterogenous and intermittent strain field (Weiss *et al.*, 2007; Marsan *et al.*, 2004; Rampal *et al.*, 2008; Stern & Lindsay, 2009). Opening of new leads in the sea ice cover is a source of rapid heat exchanges between the ocean and the atmosphere, new ice growth and brine rejection to the ocean. Seasonal ice growth in fractures accounts for 25 to 40% of the total ice production of the Arctic Ocean (Kwok, 2006). For these reasons, global climate models all include a relatively sophisticated description of the dynamics and thermodynamics of the sea ice cover. It appears therefore important that these models capture the properties of sea ice fracturing and deformation.

Sea ice rheology describes the relationship between the ice stress (or internal ice forces), the deformation of the ice cover and the material properties of sea ice. The determination of suitable constitutive continuous relations to describe sea ice rheology has guided sea ice-dynamics research since it began, and it remains an outstanding problem that limits the success of sea ice models (Feltham, 2008). Most sea ice models currently used in climate models stem from the seminal work of Hibler (1979) who described the ice cover in terms of viscous-plastic (VP) mechanics associated with a rate- and scale-independent failure envelope. This modeling framework, based on a fluid-like mechanics approach, where ice flows as a Newtonian fluid for small deformation rates and plastically for high deformation rates, is not suited to describe the multiscale fracturing processes that accommodate sea ice deformation. As shown below, the main drawback of this framework is that it does not consider long-range elastic interactions which are at the root of strain localization, intermittency and scaling.

In the Arctic, two major datasets can be used to evaluate sea ice models in terms of ice deformation. Strain-rates can be derived from drifting buoy trajectories (Rampal *et al.*, 2008) or from the sea ice kinematics produced by the RADARSAT Geophysical Processor System (RGPS) (Kwok, 1998b) which provides strain-rate estimates down to 10km resolution. Based on comparisons with these two datasets, poor correlations between the strain-rates simulated by the VP rheology and observations have been reported from regional scales (~ 300km) to small scales (~ 10km) (Thomas, 1999; Lindsay *et al.*, 2003; Kwok *et al.*, 2008).

However, the main difficulty for the evaluation of sea ice rheological models is the definition of an appropriate metric. A high correlation between model and observed ice strain-rates is desirable, but it cannot be expected at small spatial and temporal scales (e.g. < 100km and < 1 month), since sea ice velocity is mostly stochastic at such scales (Rampal *et al.*, 2009a). Correlation coefficients are thus not the best metric to evaluate models. On the other hand, sea ice deformation exhibits specific statistical and scaling properties that provide an alternative validation metric as they are the signature of the underlying fracturing and faulting processes.

These properties are expressed by a power law scaling of ice strain-rate, a relationship of the form $\langle \dot{\epsilon} \rangle = aL^{-b}$, that relates the mean deformation rate to the spatial scale L over which it is measured, a and b being constants. The scaling relationship has been extensively analyzed from buoy observations (Rampal *et al.*, 2008) and RGPS observations (Marsan *et al.*, 2004; Stern & Lindsay, 2009). It also extends to the other moments of the strain-rate, $\langle \dot{\epsilon}^q \rangle \sim L^{-b(q)}$, expressing the dependance of the strain-rate distribution upon the spatial scale of observation (Marsan *et al.*, 2004).

Girard *et al.* (2009) applied this validation metric to high resolution coupled ocean/sea ice simulations performed with the VP rheology or its elastic-viscous-plastic (EVP) derivative. These authors showed that

the statistical properties characterizing sea ice deformation were not reproduced by the simulations, even at large spatial scales. As these properties emanate from the ice mechanical behavior (Weiss, 2008; Rampal *et al.*, 2009a), this suggests that the mechanical framework of the VP rheology is inappropriate.

The aim of this paper is to introduce a new mechanical framework for sea ice modeling based on an elasto-brittle (EB) constitutive law. This framework is intended to be able to reproduce the statistical and scaling properties that characterize sea ice deformation. It is based on continuum mechanics and is simple enough to be implemented in climate models. The main characteristics of the rheology are progressive damage, which models how cracks and faults affect the ice mechanical properties, and long range elastic interactions. Basin-scale simulations over short time scales (72 h) are performed with an idealized finite element application of the model at 10 km resolution. The simulations presented are forced by the wind stress and the drag exerted by an ocean at rest, the thermodynamics and the advection of ice are not considered here. These simplified simulations aim at investigating the ice response to the main forcing terms over short time periods. We show that heterogeneous deformation fields are obtained with the EB rheology and that complexity arises from elastic interactions on a wide range of scales.

For comparison purposes, simulations with similar setup and forcing are performed with the VP rheology. Observations of sea ice deformation from the RGPS database are also considered. The statistical and scaling properties of ice deformation are used as the validation metric. We show that the EB rheology gives a much better representation of these properties than the VP rheology.

4.2 Models and observations

4.2.1 EB mechanical framework

The EB framework is built on continuum mechanics in order to be suitable for inclusion within a regional or global climate model. Sea ice is considered as a continuous $2D$ elastic plate. The ice thickness is not considered explicitly. It is however taken into account in the formulation of the elastic stiffness (see eq. 4.6). The model physics accounts for the elastic interactions that can propagate over long distances in the ice cover, as well as for fracturing processes (Weiss *et al.*, 2007). Fracturing processes are considered to play an essential role for sea ice deformation and dynamics (Weiss *et al.*, 2009; Marsan *et al.*, 2004; Schulson, 2004; Schulson & Hibler, 1991). In the EB model, the effect of fracturing is represented through progressive damage, expressed by a reduction of the local/grid-scale elastic stiffness :

$$K = K_0 d \tag{4.1}$$

where K and K_0 are, respectively, the effective and initial elastic stiffnesses, expressed in units of force per meter as detailed below, and $d \leq 1$ is a scalar indicating the damage level (Kachanov, 1986). This formulation implies that the effect of sub-grid scale fracturing is represented by a scalar damage parameter at the grid scale. The damage parameter thus represent the density of cracks and leads within the ice cover. A similar framework was used in theoretical studies investigating the statistical properties of fracture in brittle materials (Girard *et al.*, 2010a; Amitrano *et al.*, 1999).

The model considers a quasi-static ice cover (no advection) driven by the wind and ocean stress terms as well as the internal ice stress term computed by the mechanical framework presented in this section. The model is applied to the Arctic sea ice cover using a finite element method with a continuous and linear discretization. This simplified application aims at investigating the ice response, in terms of deformation, to the main forcing terms on short time scales (3 days). The other terms of the momentum balance are

neglected in this study as they are less significant on short time scales (Hibler, 1986). For the time scale considered here, ice advection and thickness variations are thus assumed negligible. With these assumptions, the momentum balance simply reads (forces per unit area) :

$$\nabla.\underline{\underline{\sigma}} + \underline{\tau_a} + \underline{\tau_w} = 0 \tag{4.2}$$

where $\underline{\underline{\sigma}}$ is the ice internal stress tensor, $\underline{\tau_a}$ is the wind stress and $\underline{\tau_w}$ is the water drag. The wind stress is calculated with an air turning angle of zero as we use 10-m wind fields (McPhee, 1975) :

$$\underline{\tau_a} = \rho_a C_a \left\|\underline{u_a}\right\| \underline{u_a} \tag{4.3}$$

where ρ_a is the air density, C_a the air drag coefficient and $\underline{u_a}$ the wind velocity. The water drag term is calculated considering an ocean at rest, using the following equation :

$$\underline{\tau_w} = -\rho_w C_w \left\|\underline{u}\right\| \underline{u} \tag{4.4}$$

where ρ_w is the water density, C_w the water drag coefficient and $\underline{u}$ the ice velocity. Sea ice is treated as an isotropic elastic material and the constitutive equation considered is Hooke's law under plane-stress hypothesis,

$$\sigma_{ij} = K\underline{\underline{D}}\,\epsilon_{ij}, \quad \text{with } \sigma_{ij} = \begin{bmatrix} \sigma_{xx} \\ \sigma_{yy} \\ \sigma_{xy} \end{bmatrix}, \ \underline{\underline{D}} = \frac{1}{1-\nu^2}\begin{bmatrix} 1 & \nu & 0 \\ \nu & 1 & 0 \\ 0 & 0 & \frac{1-\nu}{2} \end{bmatrix}, \quad \text{and } \epsilon_{ij} = \begin{bmatrix} \epsilon_{xx} \\ \epsilon_{yy} \\ \epsilon_{xy} \end{bmatrix} \tag{4.5}$$

where K is the elastic stiffness defined below, $\underline{\underline{D}}$ is the unit elasticity tensor, ϵ_{ij} is the strain tensor and ν is the Poisson's ratio. The use of an elastic constitutive law requires to compute the elastic strains from a distinguished stress-free configuration. For the idealized simulations presented in this paper, the quasi-static approximation of the state equilibrium is considered (eq. 4.2), therefore the displacement and the strain fields can be easily computed. In Eulerian models, e.g. with a fixed grid, considering the full momentum equation, computing the elastic strains is more problematic (Coon *et al.*, 1974).

The undamaged elastic stiffness of the ice K_0 is expressed as a function of a constant Young modulus Y, the ice thickness h, the ice concentration c and a constant υ. The expression of K_0 is inspired from the parameterization of the ice strength used in VP models (see eq. 4.14) :

$$K_0 = Yh\ exp^{-\upsilon(1-c)}. \tag{4.6}$$

The Young modulus Y refers to an intrinsic sea ice material property, in units of pressure, while what we define as the stiffness, in units of force per meter, accounts for the ice concentration and thickness over an element. The ice thickness h and concentration c which determine the initial elastic properties are initialized at the beginning of simulations and considered to be constant throughout the simulations. The factor $exp^{-\upsilon(1-c)}$ can be interpreted as the local contact fraction between floes as suggested by Gray & Morland (1994). At each model step, when the stress of an element, i, exceeds a given strength threshold for damage, its elastic stiffness K_i is multiplied by a constant damage factor d_0 :

$$K_i(n+1) = K_i(n)d_0 \tag{4.7}$$

n being the number of damage events of the element i. The constant d_0 is empirical and should be close enough to one to simulate the small steps of crack growth, but within a given range (e.g. $0.85 \leq d_0 \leq 0.95$), its value does not significantly affect the simulations (Amitrano *et al.*, 1999). After n damage events, the effective stiffness, $K_i(n)$ is then given by :

$$K_i(n) = K_{i,0}d_0^n \tag{4.8}$$

where $K_{i,0}$ is the undamaged elastic stiffness.

After each damage event, the state equilibrium (eq. 4.2) is calculated. Since equation 4.7 induces locally a decrease of the elastic stiffness of the element i, the stress held by this damaged element decreases as well. This results in a stress redistribution around the damaged element, which mostly affect its nearest neighbors. Because of the stress redistribution, the strength threshold for damage can be exceeded by other elements and this can onset an avalanche of damage events. An avalanche consists of several cycles of damaging (eq. 4.7) and stress redistribution (eq. 4.2) which may propagate on long distances across the ice cover. The avalanche stops when the damage criterion is no more fulfilled by any element. Stress redistribution and the induced damage propagation are key ingredients of this new EB framework and constitute a major difference with former fluid-like frameworks. The time scale associated with damage propagation and avalanches is considered to be smaller than the duration of a time step. This means that we consider time as 'frozen', i.e. constant, during damage avalanches. Damage avalanches are therefore accounted as sub-iterations during which the external forcing is held constant.

In-situ stress measurements (Weiss *et al.*, 2007) and laboratory experiments (Schulson *et al.*, 2006b) both argue in favor of Coulombic faulting within the sea ice cover. We therefore choose the Coulomb criterion to define the damage threshold :

$$\tau = \mu\sigma_N + C \tag{4.9}$$

where τ and σ_N are the shear and the normal stress at the scale of the element, respectively, C is the cohesion and μ is the internal friction coefficient. The internal friction coefficient is set to $\mu = 0.7$. This is within the range of values measured by Fortt & Schulson (2007) from sliding experiments along Coulombic shear faults in laboratory-grown freshwater ice. It is also relevant at geophysical scales for sea ice with a similar internal friction coefficient (Weiss & Schulson, 2009). To simulate material heterogeneity, which consists in defaults and cracks in the ice at sub-grid scales, the value of the cohesion C is randomly drawn from a uniform distribution. In the simulations, we arbitrarily set the C-range between 10 to 20 kPa. This range is close to the values estimated from in-situ stress measurements with values of about 40 kPa for the cohesion (Weiss *et al.*, 2007). As suggested by observations, we apply a tensile strength threshold to the criterion for $\sigma_N = -20$ kPa (the sign convention chosen is negative for tension).

Field measurements of the sea ice Young modulus report values between 7 and 10 GPa depending on the volume fraction of brines and the porosity (Schulson & Duval, 2009). Such values apply for the bulk material, they are related to the measurement scale (cm to m) and performed on crack-free samples. Our model application requires an apparent Young modulus Y associated with the grid scale, 10 km in this study. This apparent Young modulus will be much smaller than the bulk modulus due to the existence of cracks and faults at sub-grid scales. A decrease in apparent Young modulus leads to larger mean ice deformation.

We perform sensitivity tests to determine the apparent Young modulus which leads to a simulated mean total deformation at the grid scale comparable to the value estimated by RGPS observations. At 10 km and a temporal scale of 3 days, in March, this value is typically $\langle\dot{\epsilon}_{tot}\rangle = 0.014$/day (Stern & Lindsay, 2009). The methodology is applied to all simulations and the results are averaged over the different time periods simulated, leading to $Y = 0.35$ GPa. This value should only be taken as an order of magnitude as the simulations only cover short periods of time. The physical parameter and constants used in this study are summarized in table 4.1.

Symbol	Meaning	Value
h	Ice thickness	
c	Ice concentration	
K	Effective elastic Modulus	
Y	Young Modulus	350 MPa
ν	Poisson's ratio	0.3
υ	Stiffness / Ice strength constant	20
d_0	Damage parameter	0.85
τ	Shear stress	
σ_N	Normal stress	
μ	Internal friction coefficient	0.7
C	Cohesion	10 to 20 kPa
$\sigma_{tension}$	Tensile strength	-20 kPa
ρ_a	air density	$1.3\,\mathrm{kg.m^{-3}}$
C_a	air drag coefficient	0.0012
u_{10}, v_{10}	10m wind speed	
ρ_w	water density	$1025\,\mathrm{kg.m^{-3}}$
C_w	water drag coefficient	0.0055
e	Ellipse aspect ratio (VP)	2
γ_{min}	Minimum plastic deformation rate (VP)	$2 \times 10^{-8} s^{-1}$
P^*	Ice strength parameter (VP)	$2.10^4\,\mathrm{Nm^{-2}}$

TAB. 4.1: Physical parameters and constants

4.2.2 VP simulations

The VP model used for the comparison with EB is based on the work of Lietaer *et al.* (2008). The ice momentum equation for VP simulations is similar to eq. 4.2, as well as the formulation of the wind forcing and ocean drag terms (eq. 4.3 and 4.4). The $\underline{\underline{\sigma}}$ tensor is defined as a function of the strain-rate tensor $\underline{\underline{\dot{\epsilon}}}$ and two of its invariants, the divergence rate $\dot{\epsilon}_{div}$ and the shear rate $\dot{\epsilon}_{shear}$:

$$\begin{aligned} &\underline{\underline{\dot{\epsilon}}} = \tfrac{1}{2}\left(\nabla \underline{u} + \nabla \underline{u}^T\right), \\ &\dot{\epsilon}_{div} = \dot{\epsilon}_{xx} + \dot{\epsilon}_{yy}, \\ &\dot{\epsilon}_{shear} = \sqrt{\left(\dot{\epsilon}_{xx} - \dot{\epsilon}_{yy}\right)^2 + \left(2\dot{\epsilon}_{xy}\right)^2}. \end{aligned} \tag{4.10}$$

The VP rheology simulates the viscous-plastic behavior with the following constitutive equations :

$$\underline{\underline{\sigma}} = 2\eta\underline{\underline{\dot{\epsilon}}} + \left((\zeta - \eta) tr\left(\underline{\underline{\dot{\epsilon}}}\right) - \frac{P}{2}\right)\underline{\underline{I}}, \tag{4.11}$$

$$\zeta = \frac{P}{2\gamma},\ \eta = \frac{\zeta}{e^2}, \tag{4.12}$$

$$\gamma = max\left(\sqrt{\dot{\epsilon}_{div}^2 + \frac{1}{e^2}\dot{\epsilon}_{shear}^2}, \gamma_{min}\right), \tag{4.13}$$

where $tr\left(\underline{\underline{\dot{\epsilon}}}\right)$ is the trace of the strain-rate rate tensor and $\underline{\underline{I}}$ the identity tensor.

Those equations ensure that, if the strain-rate rate is greater than γ_{min}, the normal and shear stresses, respectively σ_N and τ, will define an elliptical yield curve of size P and with an aspect ratio equals to $\frac{1}{e}$.

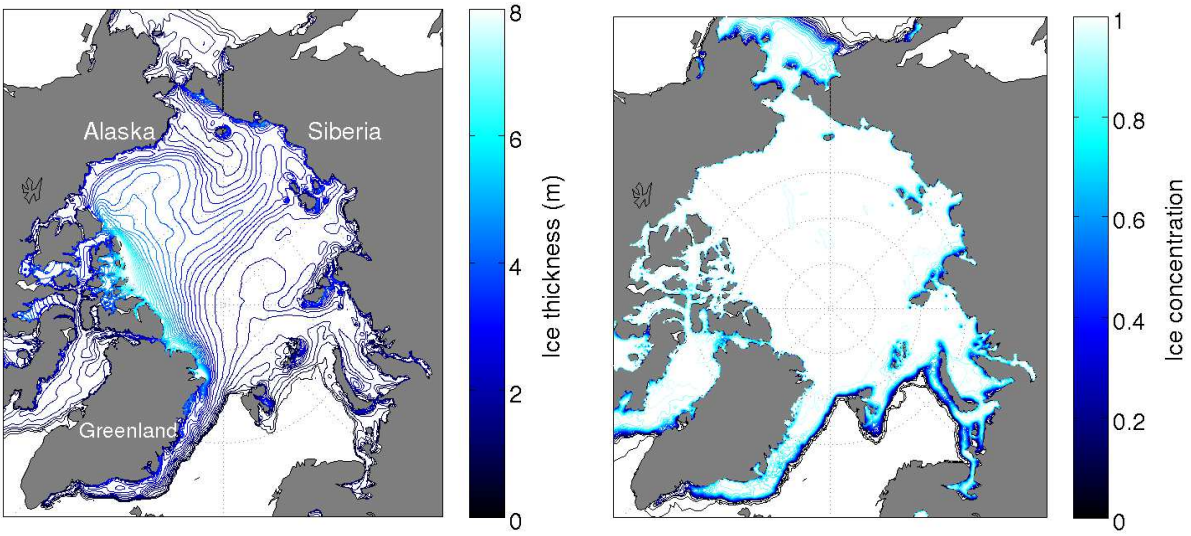

FIG. 4.1: Initial conditions of ice thickness and concentration for the simulations, extracted from the Drakkar ORCA025-G70 simulation.

When the strain-rate rate is smaller than γ_{min}, the ice behaves as a viscous fluid. The ice strength P is parametrized by :

$$P = P^* h \; exp^{-v(1-c)} \tag{4.14}$$

where P^* is the ice strength parameter while the other terms are the same as in equation 4.6.

The VP simulations are performed on the same mesh as the EB simulations but for technical reasons the computation for VP is made on the sphere (Comblen *et al.*, 2008), whereas it is done on a plane projection for EB. This difference does not however significantly influence the results. Ice initial conditions and wind forcings are interpolated from the same datasets. The same parametrisations of the wind and ocean stress terms are used. To ensure the convergence of the nonlinear system of equations we use the Newton iterative method until the residual norm has been divided by 5 at each time-step (one hour) as in Lemieux *et al.* (2010). The finite element discretization is continuous and linear, and a no-slip boundary condition is imposed on the coast.

4.2.3 Simulations setup

The simulations are performed on a mesh composed of triangular elements covering the oceans from $50°$N up to the North Pole. The effective resolution of the mesh is 10 km, below $65°$N the resolution coarsens to 150 km.

The ice thickness and concentration are initialized from the outputs of a global ocean/sea-ice numerical model simulation, referred to as ORCA025-G70. This simulation was carried out as part of DRAKKAR, a multi-scale ocean modelling project (Barnier *et al.*, 2006; Drakkar-Group, 2007). The simulation hindcast compares rather well with observations in term of sea ice extent and concentration in the Arctic (Drakkar-Group, 2007; Lique *et al.*, 2009). The ice thickness and concentration obtained from ORCA025-G70 for 2007-March-15 are interpolated to the mesh and used as the initial conditions of our simulations (figure 4.1). The simulations are started with an undamaged ice cover. No-slip boundary condition is imposed on the coast.

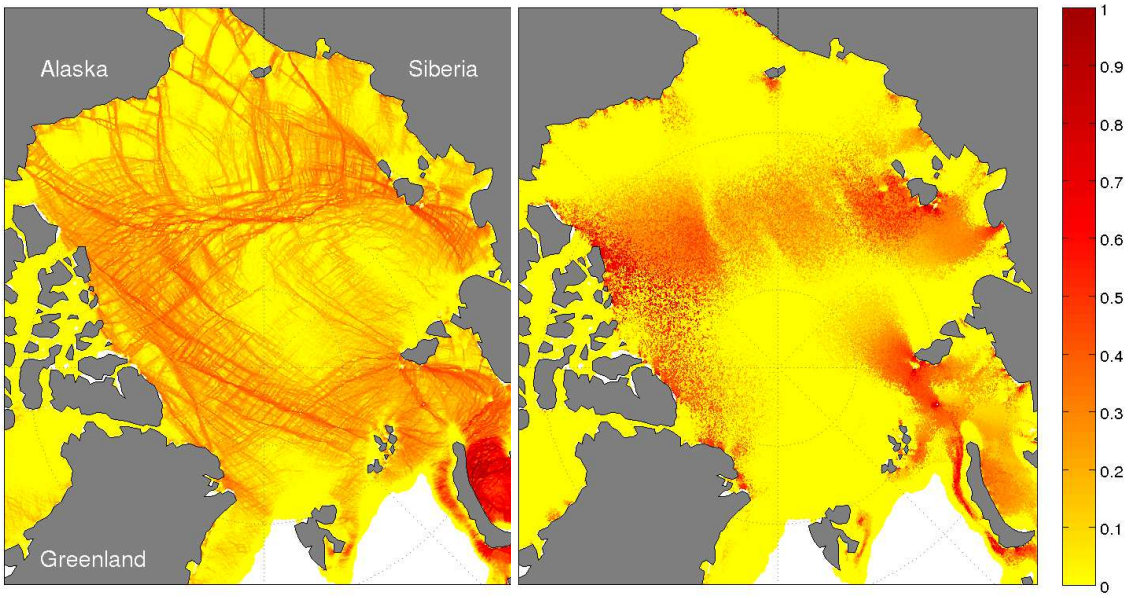

FIG. 4.2: Normalized number of damage events at the end of an EB-simulation. The left panel shows the normal result, where damage events induce a progressive reduction of the elastic modulus. On the right panel the reduction of elastic modulus has been disabled ($d_0 = 1$), damage events are thus not followed by stress relaxation. The difference between the two fields illustrates the importance of elastic interactions (simulation start date is 2007-March-27).

The wind speed used to drive the simulations is obtained from the 6-hourly ECMWF operational analyses (10-m wind speed), with an effective resolution of ~ 80 km in the central Arctic. The wind speed is linearly interpolated in space and time at every model step. The total duration of the simulations is 96 hours. During the first 24 h, considered as a spin-up, the wind stress is progressively increased up to its nominal value, which is then applied during the rest of the simulation (72 h). The time step used in all simulations is 20 seconds. Simulations are performed over three time periods starting on March 15^{th},19^{th} and 27^{th} 2007.

4.2.4 RGPS Observations

RGPS observations of ice deformation from March 2007 are used in this study for statistical comparisons with the simulations presented. RGPS is based on a cross-correlation technique applied to consecutive SAR images (Fily & Rothrock, 1990), which allows tracking in a Lagrangian fashion of points on the sea ice cover (http ://www-radar.jpl.nasa.gov/rgps/). The tracked points define the corners of cells which are initially squared ($10 \times 10\,\mathrm{km}^2$). The spatial gradients of the velocity field $\partial u/\partial x$, $\partial v/\partial x$, $\partial u/\partial y$, $\partial v/\partial y$ are computed for each cell over the period between two observations (sampled at irregular time intervals within the domain, but typically 3 days) (Kwok, 1998b). Recast in terms of strain-rate tensor components,

$$\begin{aligned} \dot{e}_{xx} &= \partial u/\partial x, \\ \dot{e}_{yy} &= \partial v/\partial y, \\ \dot{e}_{xy} &= \left(\partial u/\partial y + \partial v/\partial x\right)/2, \end{aligned} \tag{4.15}$$

the shear and divergence rates can finally be calculated (eq. 4.10) along with the total deformation rate $\dot{\epsilon_{tot}} = \sqrt{\dot{\epsilon}^2_{shear} + \dot{\epsilon}^2_{div}}$. Henceforth, the term deformation refers to the total deformation rate $\dot{\epsilon}_{tot}$. Further details on RGPS observations and their accuracy are presented in Lindsay & Stern (2003).

4.3 Damage localization in EB simulations

In the early stages of EB simulations, the elastic stiffness of the ice cover, set by ice thickness and concentration fields (figure 4.1), varies smoothly over the ocean. During spinup, the wind stress is progressively increased and damage events start to occur. These damage events are first homogeneously scattered throughout the Arctic Ocean. The reduction of elastic stiffness occuring when an element is damaged induces a stress redistribution, which can trigger other damage events in the vicinity and onset an avalanche of damage. Further on in the simulations, large avalanches occur corresponding to the propagation of the stress relaxation over long distances. This results in linear damage bands, which are the expression of long range elastic interactions that take place within the ice cover (figure 4.2). These linear features represent active faults that concentrate shear deformation and divergence (see below). Most of them are very narrow, as observed for real faults (Schulson, 2004), with a width set by the spatial resolution (i.e. one element wide).

Note that this heterogeneity in the elastic stiffness and damage field is not originally set as an initial condition in the simulations, instead it emerges from elastic interactions between the elements. This can be illustrated by performing a simulation without reduction of elastic stiffness ($d_0 = 1$). In this case, damage events occur only locally, in places where the wind stress is sufficiently large. Damage remains scattered without localization and linear faults do not appear (figure 4.2).

4.4 Strain-rate fields and linear kinematic features

Figure 4.3 shows an example of the shear and divergence rates from EB and VP simulations, calculated for the 3-day period of the simulation. The RGPS observations available for this time period are also plotted. Similar results are obtained for the other time periods considered. The simulated strain-rates are calculated at the grid scale, $10\,$km, which is also the length scale of the RGPS Lagrangian cells. Considering the high resolution and the idealized settings and forcing, the simulations are definitely not expected to predict the observed ice strain field. Faults in the ice cover are initiated at stress concentrators. In EB simulations the stress field is initially nearly homogeneous, as there is no initial damage, but heterogeneities can emerge from the random distribution of the damage thresholds (the cohesion C). Our simulations are started with an undeformed ice cover, while the deformation of the central Arctic ice pack is known to keep 'memory' of large deformation events during the course of a winter season and major faults can be activated several times (Coon *et al.*, 2007).

Nevertheless, EB and VP results can be contrasted with each other and with the available observations. The comparison is focused on the central Arctic Ocean (150km away from coastlines and straits), since we have simplified the ice momentum equation. The strain-rate fields obtained with the EB rheology show strong localization of the high strain-rate values, in agreement with observations. As an illustration, in RGPS observations the largest 50% of all shear is accommodated by only 6% of the surface area, a value close to that obtained with the EB simulation, 4%. In contrast, the VP strain field is much less localized, with the largest 50% of all shear accommodated by more than 20% of the ice surface.

Insights on mechanisms driving the ice deformation can be obtained by analysing the correlations between shear and divergence fields. RGPS observations show a strong correlation between the shear and divergence fields ($R^2 = 0.83$) that argues for a shear faulting mechanism associated with dilatancy (Weiss & Schulson, 2009) : shearing along rough faults is necessarily accompagnied by fault opening, i.e. divergence. A strong correlation between shear and divergence could also result from opening followed by sliding but this is less likely to occur in the winter ice pack which is confined in the Arctic basin with concentrations close to one.

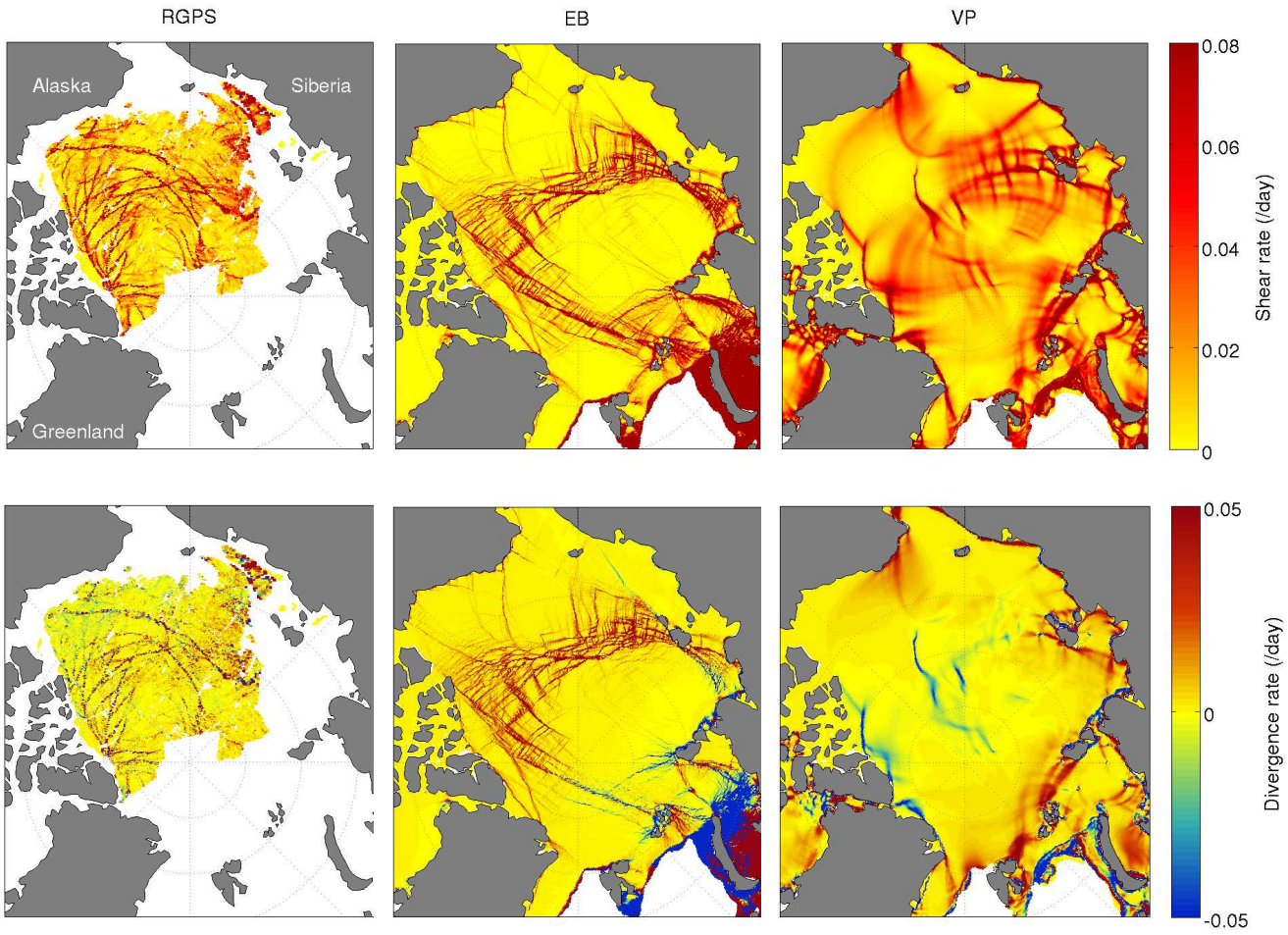

FIG. 4.3: Shear and divergence rate (/day) from RGPS observations (1^{st} column), EB simulation (2^{nd} column) and VP simulation (3^{rd} column). The RGPS observations represented were obtained between March-26^{th} and April-1^{st} 2007. Strain-rates from EB and VP simulations were computed between March-28^{th} and March-30^{th} 2007, for a temporal scale of 3 days.

The correlation between shear and divergence is also high in the EB simulation ($R^2 = 0.77$) but lower in the VP simulation ($R^2 = 0.58$). Another argument is that regions of strong shear and divergence rates show conjugates failure lines in EB simulations, such as seen in satellite images of failure (Schulson, 2004) and predicted by the Coulomb theory. This shows that the EB modeling framework captures well the physics of shear faulting that accommodates most of sea ice deformation. The mechanical framework is thus able to generate the so-called linear kinematic features (Kwok, 2001).

4.5 Strain-rate distributions

For many climate applications, it is more important to get a good estimate of the ice strain-rate distributions in models than to obtain a good correlation with strain-rate observations, since the strain-rate statistics and the shape of their distribution functions impacts winter ice growth rates (Lindsay *et al.*, 2003). Hutchings *et al.* (2010) have shown that a poor representation of small scale sea ice deformation can have an important impact on ice growth estimates. Furthermore, at small spatial and temporal scales, to predict in a deterministic sense the ice strain-rate field is impossible considering the stochastic behavior of ice velocity fluctuations at such scales. Simulated strain-rates are thus evaluated against observations through their

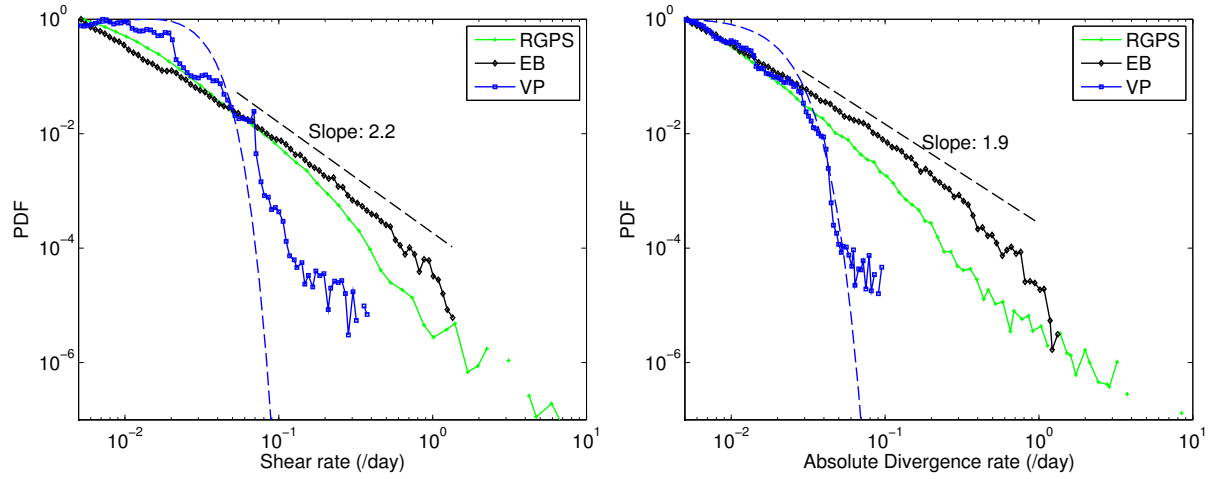

FIG. 4.4: PDFs of shear and absolute divergence rate (/day) for EB simulations, VP simulations and RGPS observations. The strain-rate are calculated at the spatial scale of 10 km and temporal scale of 3 days. PDFs are normalized by their maximal value. For RGPS and EB, dashed lines indicate the exponents of power law tails, the blue dashed line is the gaussian distribution of same mean and standard deviation as the VP distribution.

probability density functions (PDFs). The PDF of RGPS strain-rates is known to exhibit a power law decay, $p(\dot{\epsilon}) \sim \dot{\epsilon}^{-\alpha}$, where α depends on the spatial scale considered (Marsan *et al.*, 2004). Such distributions with $\alpha \leq 3$ are characterized by 'wild randomness' and dominated by extreme values. The PDF of strain-rates simulated by the VP rheology were showed to have a very different shape, without power law behavior. Instead, they are in the Gaussian attraction basin and are associated with 'mild randomness', the extreme values are not captured (Girard *et al.*, 2009).

Figure 4.4 shows the PDF of shear and absolute divergence rates for EB and VP simulations and RGPS observations. Simulated strain-rates are extracted from all simulations, from the central Arctic Ocean (150 km away from the coastlines, the Fram and Bering Straits). In order to get a statistically representative amount of observations, all RGPS measurements of March 2007 were considered. The PDF obtained with the observations does not vary significantly if only a part of these data is considered.

The PDF of shear rates obtained with EB simulations compares very well with the RGPS observations, with a clear power law behavior over two orders of magnitude with an exponent of $\alpha = 2.2$. The fact that these statistical properties are well captured by the EB simulations is a strong argument in favor of the new mechanical framework. Regarding the PDF of divergence rates, the agreement between RGPS observations and the EB rheology is also good since both the EB and RGPS PDFs show a power law decay. The PDFs exponents show small differences, with an exponent of 2.5 for the RGPS while an exponent of 1.9 is obtained for EB simulations. Our results also confirm the strong discrepancy with the PDFs of VP strain-rates, which are close to Gaussian distributions, and the RGPS PDFs. The EB framework successfully captures the statistical properties of strain-rates and the power law tail of the PDFs, while the VP rheology does not.

4.6 Scaling properties of ice deformation

The total deformation rate of sea ice is characterized by spatial as well as temporal scaling laws which are the signature of long-range elastic interactions and space-time coupling (Weiss *et al.*, 2009; Rampal *et al.*, 2008; Marsan *et al.*, 2004). These scaling laws are not inherited from the wind-forcing but instead they are believed to emanate from the ice mechanical behavior and thus consitute an interesting metric to evaluate

the physics of sea ice models. The spatial scaling of simulated total deformation rate is analyzed in this study and compared with the scaling law obtained from observations. Seasonal variations of the spatial scaling have been explored (Stern & Lindsay, 2009), the analysis we perform is intended to be representative of March 2007. Three daily strain-rates obtained from the 3 different time periods of the simulations are thus merged and all RGPS observations from March 2007 are considered for the analysis (a dataset similar to the previous section). A coarse graining procedure is applied to the strain-rates in order to compute the total deformation rates on a wide range of scales (10 km to 1000 km) following the methodology presented by Marsan *et al.* (2004). Figure 4.5 shows the mean total deformation rate as a function of the spatial scale.

The observations show a power law scaling of the mean total deformation rate, $\langle \dot{\epsilon}_{tot} \rangle \sim L^{-b}$, with $b = 0.17$. The last bin shows a small deviation from this power law behavior and could be due to a finite size effect, as the scale reaches the order of magnitude of the width of the Arctic basin. A similar exponent of the scaling law has been reported before for March (Stern & Lindsay, 2009). Regarding the models, the EB simulated total deformation rate also show a power law scaling which is characterized by a slightly shallower exponent, $b = 0.1$. The last bin also appears to be affected by a finite size effect. If single EB simulations are considered, the scaling exponent shows variations between $b = 0.09$ and 0.15. This is slightly lower than the range expected for observations in March (roughly $b = 0.12$ to 0.20). On the other hand, the VP simulated strain-rate does not vary significantly with the scale, except towards very large scales, once again, a likely expression of a finite size effect.

The power law scaling obtained for EB simulations is another argument in favor of the new mechanical framework. It expresses the heterogeneity of the simulated deformation field that emerges from elastic interactions between elements over a wide range of scales. The limit of this scaling at small scales is only fixed by the model resolution. This means that running simulations at higher resolution would result in increased localization of the deformation and would involve even more extreme strain-rate values.

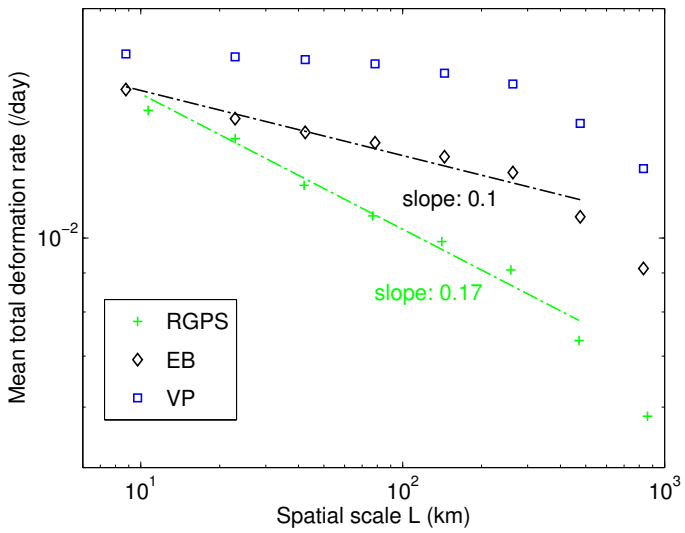

FIG. 4.5: Mean total deformation rate (/day) as a function of the spatial scale L. The dashed lines are power law fits to the data.

4.7 Discussion and conclusions

An elasto-brittle mechanical framework for sea ice models has been presented. This framework is intended to describe the mechanical behavior of dense pack ice, for ice concentrations typically above 95%. In this case, stresses can be transmitted on long distances across the ice cover resulting in heterogeneous strain-rate fields characterized by specific statistical and scaling properties. These mechanisms are described in the EB framework by progressive damage and long range elastic interactions. The results presented in this study demonstrate that such physics allows the emergence of heterogeneity in the simulated ice deformation. The statistics of ice strain-rates are well represented by the EB rheology although the simulations considered here are rather crude and consider only short winter time periods. This is a noteworthy point since no other model of sea ice mechanics had succeeded in capturing these properties so far. In particular, the VP rheology, currently used in most sea ice models, has been shown to be unable to capture the properties of ice strain-rates (Lindsay *et al.*, 2003; Girard *et al.*, 2009). When ice concentrations are lower, stresses cannot be transmitted as well as in a more continuous ice cover. In this case, the ice cover consists of floes drifting as a granular flow (Feltham, 2005), or almost freely when ice concentrations are even lower. Physically, the use of the EB rheology at low ice concentrations might appear inappropriate. In a global model, it might be necessary to disable the rheology beyond a given concentration threshold (i.e. to switch to free drift).

Our results support the scenario proposed by Weiss *et al.* (2007) considering that fracture and frictional sliding govern the inelastic deformation over a wide range of spatial scales, a viewpoint which was also shared in the granular sea ice model of Hopkins & Thorndike (2006). A similar approach was recently used by Wilchinsky *et al.* (2010a,b) to show the importance of shear failure associated with dilatancy for sea ice deformation. Among the other approaches followed to account for the brittle behavior of sea ice, the elasto-decohesive model considers many of the same issues adressed in this paper (Schreyer *et al.*, 2006; Sulsky *et al.*, 2007). This model accounts for failure by a loss of cohesion rather than damage and the leads/fractures are represented explicitely, instead of using a continuum damage formulation. The EB rheology offers the advantage of using continuum mechanics which is more suitable for the implementation in a global coupled ocean-sea ice model. At time scales longer than a few days, the effect of refreezing, or 'healing', of damaged areas on ice mechanics needs to be accounted for. By opposition to damage, healing tends to restore the initial ice mechanical properties, when temperature conditions allow refreezing. We are currently working on the implementation of healing in the EB framework, which is a necessary step before the rheology can be used in global sea ice models on longer time periods.

A frequently put forward justification of the poor quality of the VP simulated ice deformation is the resolution and the quality of the forcing fields (including winds) used to drive sea ice models. The simulations presented in this study are driven by wind fields derived from reanalysis, similarly to global sea ice models, with an effective resolution of about $80\,$km. In such products, boundary layer turbulence and small scale variability of the wind velocity are indeed not captured. Albeit this smooth forcing, EB simulated deformation is heterogeneous and the localization of deformation occurs down to the grid scale, $10\,$km. This provides an interesting insight on the origin of the statistical and scaling properties of the EB sea ice deformation : they cannot be inherited from the wind forcing since the deformation fields obtained show scaling down to the grid scale, which is much smaller than the wind forcing resolution. This supports the conclusions of Rampal *et al.* (2009a) drawn from statistical analysis buoy-derived ice deformation. Our results argue that the statistics of sea ice deformation arise from the elasto-brittle mechanical behavior of the ice. In other words, the limitation of classical sea ice models is unlikely due to the resolution and the quality of the forcing, but to the model physics itself. Increasing the resolution of these models or of the forcing fields will not suffice to

capture the properties of ice deformation.

Acknowledgements

The RGPS data were provided by the Polar Remote Sensing Group at JPL. ECMWF analyses were provided in the framework of the Drakkar cooperation on global ocean/sea-ice modeling. We are grateful to the MEOM-LEGI team and especially J.M. Molines and B. Barnier for providing the Drakkar OGCM simulation. The EB simulations presented in this paper were performed at the Service Commun de Calcul Intensif de l'Observatoire de Grenoble (SCCI-CIMENT). The ice model used for VP simulations is a component of the SLIM project (http ://www.climate.be/SLIM), which is funded by the Communauté Française de Belgique, as Actions de Recherche Concertées, under contract ARC 04/09-316. D. Amitrano thanks French program INSU-Catell and EU program Trigs for support. L. Girard is supported by a BDI Ph.D. grant from CNRS. P. Rampal is warmly acknowledged for thrilling discussions and encouragements. We also acknowledge the work of the scientific editor and the reviewers in improving the paper.

Chapitre 5

Architecture d'une rhéologie elasto-fragile pour la banquise

Abstract

This chapter presents the architecture of an elasto-brittle (EB) rheological model for sea ice mechanics. The main goal of the mechanical framework we present is to capture the statistical and scaling properties of sea ice deformation, which can be considered as a characteristic of the ice mechanical behavior and play an important role regarding ice growth estimates. The model considers sea ice as a continuous elastic plate that can transmit stresses over long distances. The brittle behavior of the ice is represented using a local scalar damage parameter, which affects the ice elastic properties. As the rheology is based on continuum mechanics, fracturing and faulting are therefore not explicitely represented, but the local damage parameter can be seen as the density of fractures and leads within the ice at the local scale (i.e. element/grid scale). Long range elastic interactions and progressive damage are the core of the EB rheology. When the temperature conditions allow, sea ice can recover its mechanical properties through refreezing of faults and leads. In the present model this mechanism is accounted through a 'healing law' that strengthens the ice in freezing conditions. Preliminary results from simulations including healing are presented. The implementation of the EB rheology within a global sea ice model is discussed.

5.1 Introduction

This study is a contribution to the development of numerical models describing the mechanical behavior of the sea ice cover. In dense pack ice, internal stresses are important and the mechanical behavior of the ice has a marked influence upon ice drift, deformation and dynamics. The distribution of sea ice strain rates and especially divergence rates, which quantify openings in the ice cover, has a strong impact on air-sea exchanges of heat as well as on the ice production. The statistics of sea ice deformation should therefore be well captured by models used in climate studies. A positive trend in the mean strain-rate of sea ice has recently been reported and could play a significant role in the 'Polar Amplification' through positive feedbacks on the ice decline (Rampal *et al.*, 2009b). Stronger ice deformation means (1) more lead openings, resulting in a lower average surface albedo, which increases the ice melt in spring/summer and (2) a more fragmented ice cover that can drift faster and possibly increase the ice export through Fram Strait. Current sea ice models do not adequately represent ice deformation (Girard *et al.*, 2009; Kwok *et al.*, 2008; Lindsay *et al.*, 2003; Thomas, 1999), and a poor representation of small scale ice deformation can have an important impact on ice growth estimates (Hutchings *et al.*, 2010). Improving the description of sea ice deformation in climate models is therefore a crucial step towards reliable simulations of the rapidly declining Arctic sea ice cover.

Many factors influence the model estimates of ice deformation : wind forcing fields, ocean currents, the ice thickness distribution, the formulation of the ice mechanical thickness redistribution (Rothrock, 1975) and the model constitutive law relating deformation to stress (Lindsay *et al.*, 2003). Rampal *et al.* (2009a) recently showed that the statistical properties of ice drift and deformation present important differences with the properties that could be expected in the case of free drift, without sea ice internal stresses. This means that spatio-temporal patterns of ice deformation are not directly inherited from the forcing (i.e. essentially the winds) but instead mainly arise from the ice mechanical behavior itself. In other words, this indicates that capturing the properties of sea ice deformation in models is, to a large extent, a matter of having an appropriated ice rheology. The limitation of current sea ice models regarding ice deformation could therefore result from their formulation of the ice rheology, namely, for most global models, the Viscous Plastic (VP) rheology (Hibler, 1979). Increasing the resolution of these models or of the forcing fields will not be sufficient to capture the properties of ice deformation (Girard *et al.*, 2010b). This has motivated the development of a new mechanical framework for sea ice modelling based on a completely different viewpoint.

Recent analysis of drifting buoy trajectories and fine scale sea ice kinematics produced by the RADARSAT Geophysical Processor System (RGPS) (Kwok, 1998b) expressed the heterogeneous and intermittent character of sea ice deformation by spatial and temporal scaling laws (Marsan *et al.*, 2004; Rampal *et al.*, 2008). These relations imply that sea ice deformation has no characteristic spatial or temporal scale. In other words, it shows very large correlation lengths. For example, in the Arctic, the spatial correlation length of ice deformation fields is only limited in space by the size of the Arctic basin. Investigation of internal sea ice stresses at the local scale (Richter-Menge *et al.*, 2002) revealed the importance of the Coulombic faulting mechanism for sea ice deformation and as well as an associated brittle behavior (Weiss *et al.*, 2007). A scenario that can explain the origin of these properties is that sea ice deformation is mostly accomodated by the interplay of multiple active fractures and faults of all sizes/scales. In this case, the deformation process is characterised by critical dynamics where a small, local perturbation can trigger events of sizes spreading over several orders of magnitude (Weiss *et al.*, 2007).

The limitations of the historical VP model to properly represent sea ice deformation processes, although stressed for a long time (Nye, 1973), became more apparent lately in the light of recent observations (e.g. RGPS) and increasing resolution of climate models. Consequently, different approaches have been proposed recently to account for the brittle behavior of sea ice in models. Using a discrete element approach describing the failure and refreezing of floes, Hopkins & Thorndike (2006) captured the power law distribution of floe sizes. A similar approach was recently used by Wilchinsky *et al.* (2010a) to show the importance of shear failure associated with dilatancy for sea ice deformation. These studies gave a better insight into the mechanisms that accommodate sea ice deformation but the discrete element approach is unadapted for coupling with an ocean model. Consequently, Wilchinsky & Feltham (2006b) presented a continuous model treating the ice cover as diamond-shaped floe aggregates formed in brittle compressive shear failure. Another approach considered an elastic-decohesive constitutive model giving a specific representation of leads as discontinuities, describing their orientations and modes of failure (Schreyer *et al.*, 2006). However, the explicit representation of leads as discontinuities requires an adapted numerical scheme to track their evolution (Sulsky *et al.*, 2007) and the implementation of such a rheology in a global model is not straightforward.

The approach we have chosen describes the long-range elastic interactions that take place within the ice cover and that have an essential role on brittle deformation. Using a progressive damage model, Girard *et al.* (2010a) showed that multifractal properties of the deformation, similar to that observed for sea ice, can emerge from such long-range elastic interactions. Following on from this work, the main assumptions of the rheological model detailed below is that sea ice is a continous elastic material that can transmit stresses over long distances, i.e. long range elastic interactions can take place within the ice cover. Its main goal is to capture the statistical and scaling properties of sea ice deformation, which can be considered as a characteristic of the ice mechanical behavior (Rampal *et al.*, 2009a) and play an important role regarding ice growth estimates (Hutchings *et al.*, 2010). The brittle behavior of the ice is represented using a local scalar damage parameter, which affects the ice elastic properties. As the rheology is based on continuum mechanics, fracturing and faulting are therefore not explicitely represented, but the local damage parameter can be seen as the density of fractures and leads within the ice at the local scale (i.e. element/grid scale). Long range elastic interactions and progressive damage are the core of the elasto-brittle (EB) rheology. When the temperature conditions allow, sea ice can recover its mechanical properties through refreezing of faults and leads. In the present model this mechanism is accounted through a 'healing law' that impacts the damage parameter (ice strengthening in freezing conditions).

The structure of this chapter is as follows, section 5.2 presents a detailed description of the model. Section 5.3 presents results from simulations carried out with the EB rheology under idealised conditions. The focus is on the impact of healing on the statistical properties of the simulated deformation, as the evolution of damage has already been reported in previous studies related to the EB rheology (Girard *et al.*, 2010a,b). In section 5.4 we present how this rheological framework can be implemented within a global sea ice model. Finally the results and perspectives of this work are discussed in section 5.5. The descriptions given in sections 5.2 and 5.3 are based on the finite element method, hence the use of the term 'element', rather than 'grid-cell', to describe local properties. However, the mechanical framework presented can be applied to other numerical methods, such as finite differences.

Symbol	Meaning	Value
h	Ice thickness	
c	Ice concentration	
ρ	Ice density	
K	Elastic stiffness	
d	Local damage parameter	$0 < d \leq 1$
Y	Young Modulus	
α	Stiffness constant	20
d_0	Damage parameter	0.9
τ	Shear stress	
σ_N	Normal stress	
μ	Internal friction coefficient	0.7
C	Cohesion	10 to 20 kPa
σ_{Nmin}	Tensile strength	-20 kPa
σ_{Nmax}	Compressive strength	100 kPa
t_h	Characteristic time for healing	
β	Healing parameter	
T_a	Surface air temperature	
T_f	Sea water freezing temperature	

TAB. 5.1: Main physical parameters and constants

5.2 The mechanical framework

The sea ice cover is described here as a bidimensional elastic plate that can encounter progressive isotropic damage at the element scale. Following the framework of damage mechanics (Kachanov, 1986), we consider that the ice has an effective elastic stiffness K, related to an initial/undamaged stiffness K_0 through a scalar damage parameter d,

$$K = d\,K_0, \quad \text{with } 0 < d \leq 1, \tag{5.1}$$

where $(1 - d)$ represents the density of cracks and leads within the ice cover at the local scale. This formulation implies that the effect of sub-element scale fracturing is represented by a scalar damage parameter at the element scale. Note, however, that this could be extended to a tensorial formulation in order to take into account an anisotropic character of fracturing at the sub-element scale. At the laboratory sample scale, the elastic properties can be related to crack density (Kachanov, 1994). Moreover, at such scale, this framework shows good agreement with progressive damage observed in brittle materials (Katz & Reches, 2004; Amitrano & Schmittbuhl, 2002), particularly when loaded in compression. By analogy, equation 5.1 is used here to describe the evolution of the sea ice elastic stiffness on larger scales, the scales of interest for sea ice models ranging from ~ 1 to 100 km. An argument that can be invoked to use such framework at scales larger than the laboratory sample scale is that brittle deformation of sea ice is mostly accomodated by Coulombic faulting, which is a multiscale mechanism occuring over a wide range of scales with a scale-independant physics (Weiss & Schulson, 2009). The damage parameter is indeed controlled by fracturing and faulting processes, inducing a softening (decreasing d), but also by refreezing, which causes hardening of the ice (increasing d). This section first presents the complete definition of the ice elastic stiffness and then des-

cribes the mechanisms controlling the evolution of the damage parameter through fracturing and faulting processes on one hand, and healing (refreezing) on the other hand. The main model physical parameters and constants are presented in table 5.1.

5.2.1 Elastic stiffness and main equations

As we are working with 2D dynamics, the ice thickness h and concentration c (the fraction of ice on the element) should be accounted for in the definition of the ice elastic properties. This is the reason for defining the ice elastic stiffness K at the element scale as

$$K = d\,Y\,h\,\exp^{-\alpha(1-c)}, \tag{5.2}$$

where d is a scalar damage parameter as previously introduced, Y is the ice Young modulus and α is a constant empirical parameter. The Young modulus refers to an intrinsic sea ice material property, in units of pressure, while what we define as the stiffness K, in units of force per meter, accounts for the ice concentration and thickness over an element. The parameterisation of K is inspired from the parameterisation of the ice strength in the VP rheology (see e.g. Fichefet & Morales-Maqueda (1997), eq. 19). The linear dependance of K on h is patent and allows to describe the effect of ice growth and thawing in a 2D framework. Besides, the parameterization of K with the ice concentration c is such that K decreases very quickly when c is below 1. For example, with $\alpha = 20$, a decrease of c from 1 to 0.9 induces a change in elastic stiffness from K to $0.13K$. Measurements of Young modulus from sea ice samples report values between 7 and 10 GPa depending on the volume fraction of brines and the porosity (Schulson & Duval, 2009). Such values apply for the bulk material, they are related to the measurement scale (cm to m) and performed on crack-free samples. Our model application requires an apparent Young modulus Y associated with the element scale, i.e. the km scale and above. The apparent Young modulus of equation 5.2 should be much smaller than the bulk modulus due to the existence of cracks and faults at sub-element scales. Its value should decrease as the element scale increases. In a first application of the EB rheology, we obtained a value of $Y = 0.5$ GPa from sensitivity tests at the scale of 10 km (Girard *et al.*, 2010b).

The 2D momentum equation considered can be written schematically in Cartesian coordinates (x, y) as

$$m\frac{\partial \underline{u}}{\partial t} = \underline{F_{ext}} + \nabla.\sigma_{ij} - \underline{F_p}, \tag{5.3}$$

where $m = \rho h$ is the ice mass per unit area, ρ being the ice density, $\underline{u} = (u, v)$ is the ice velocity, σ_{ij} is the ice internal stress tensor (defined in eq. 5.4) and $\underline{F_{ext}}$ denote external forcing due to wind stress, ocean stress, sea surface tilt, and the Coriolis effect. $\underline{F_p}$ is a stress term associated with healing, defined in section 5.2.3. Sea ice is considered as an isotropic material and the constitutive equation considered is Hooke's law under plane stress hypothesis,

$$\sigma_{ij} = K\underline{\underline{D}}\,\epsilon_{ij}, \quad \text{with } \sigma_{ij} = \begin{bmatrix} \sigma_{xx} \\ \sigma_{yy} \\ \sigma_{xy} \end{bmatrix}, \ \underline{\underline{D}} = \frac{1}{1-\nu^2}\begin{bmatrix} 1 & \nu & 0 \\ \nu & 1 & 0 \\ 0 & 0 & \frac{1-\nu}{2} \end{bmatrix}, \quad \text{and } \epsilon_{ij} = \begin{bmatrix} \epsilon_{xx} \\ \epsilon_{yy} \\ \epsilon_{xy} \end{bmatrix} \tag{5.4}$$

where $\underline{\underline{D}}$ is the unit elasticity tensor, ϵ_{ij} is the strain tensor and ν is the Poisson's ratio. The scheme presented on figure 5.1 gives the sequence of operations followed by the EB rheology for each model step and provides a guideline for the following paragraphs describing damaging and healing processes.

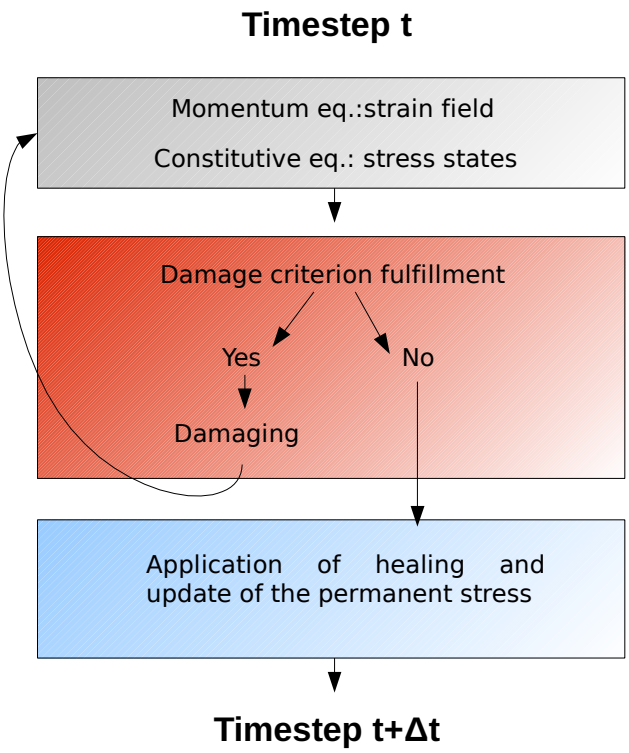

FIG. 5.1: Sequence of operations of the EB rheology

5.2.2 Damaging

When the stress state of an element, i, exceeds a given strength threshold for damage, its damage parameter d_i decreases following a progressive law :

$$d_i(t + \Delta t) = d_i(t)\, d_0, \tag{5.5}$$

where $d_i(t + \Delta t)$ is the updated damage parameter. The constant parameter d_0 is empirical and should be chosen close enough to one to simulate the small steps of crack growth, but within a given range, its value does not significantly affect the simulations (Amitrano *et al.*, 1999). After each damage event, the momentum balance (eq. 5.3) is calculated. Since equation 5.5 induces locally a decrease of the elastic stiffness of element i, the stress held by this damaged element decreases as well. This results in a stress redistribution around the damaged element, which mostly affects its nearest neighbours. Because of the stress redistribution, the strength threshold for damage can be exceeded by other elements and this can onset an avalanche of damage events. An avalanche consits of several cycles of damaging (eq. 5.5) and stress redistributions (eq. 5.3) which may propagate on long distances across the ice cover. The avalanche stops when the damage criterion is no more fulfilled by any element (figure 5.2). Stress redistribution and the induced damage propagation are the key components of the EB rheology and constitute a major difference with former fluid-like frameworks such as the VP rheology.

All preliminary results obtained with the EB rheology (section 5.3 and chapter 4) were based on a quasi-static assumption, where the acceleration term of the momentum equation (eq. 5.3) was neglected. As this section is intended to give a general description of the rheological model, the full momentum equation was presented. The numerical methods used to solve the dynamic equation are more complicated than for the quasi-static approximation, but this case has not been tested so far.

The time scale associated to damage propagation and avalanches is considered to be smaller than the duration of a time step. This means that we consider time as 'frozen', i.e. constant, during damage avalanches.

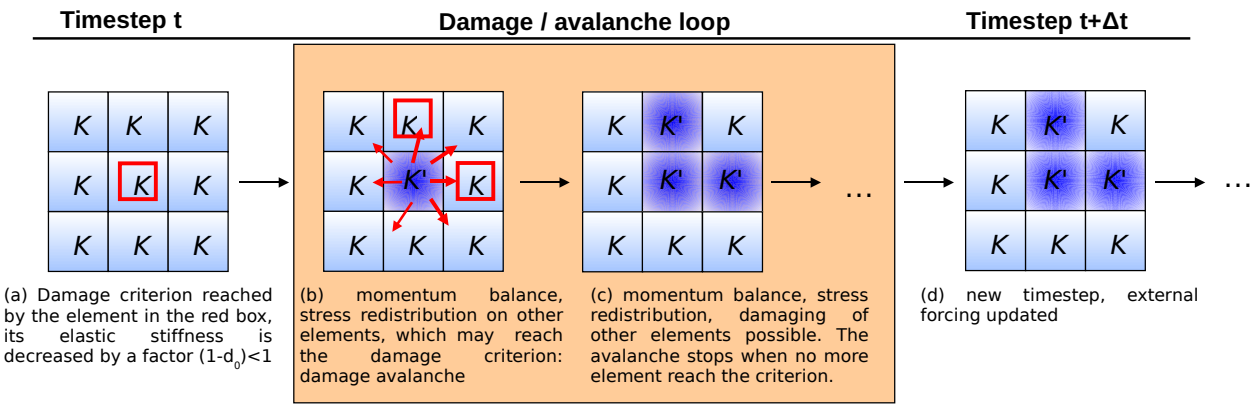

FIG. 5.2: Schematic view of damage propagation in the EB rheology. This simplified illustration considers a model of 9 elements, all having a similar elastic stiffness K at timestep i. $K' = Kd_0$ is the updated elastic stiffness after a damage event.

Damage avalanches are therefore regarded as sub-iterations where the external forcing is constant. This hypothesis implies that the model time step should be at least equal to the time needed for the propagation of elastic waves across the domain of interest. For example, if we consider the Arctic basin, ~ 2000 km, and a wave propagation speed of 1 km/s, then a time step of 2000 s or larger could be used.

In-situ stress measurements (Weiss *et al.*, 2007) and laboratory experiments (Schulson *et al.*, 2006b) both argue in favor of Coulombic faulting within the sea ice cover. We therefore choose the Coulomb criterion to define the damage threshold :

$$\tau = \mu\sigma_N + C \tag{5.6}$$

where τ and σ_N are the shear and the normal stress at the scale of the element, respectively, C is the cohesion and μ is the internal friction coefficient (figure 5.3). The internal friction coefficient is set to $\mu = 0.7$. This is within the range of values measured by Fortt & Schulson (2007) from sliding experiments along Coulombic shear faults in laboratory-grown freshwater ice. It is also relevant at geophysical scales for sea ice with a similar internal friction coefficient (Weiss & Schulson, 2009). In-situ stress measurements indicate maximal values of about 40 kPa for the cohesion (Weiss *et al.*, 2007). In the model, the material heterogeneity consisting in defaults and cracks in the ice at sub-grid scales is accounted by randomly drawing the value of the cohesion C from a uniform distribution. Moreover, after each damage event, a new cohesion is redrawn from the initial distribution to simulate the material heterogeneous strength during damage increase. In a first application of the EB rheology, C was drawn between 10 and 20 kPa. Motivated by observations of ice internal stress states, a truncature of the criterion was applied in tension for a tensile strength $\sigma_{Nmin} = -20$ kPa (the sign convention chosen is negative for tension) (Girard *et al.*, 2010b).

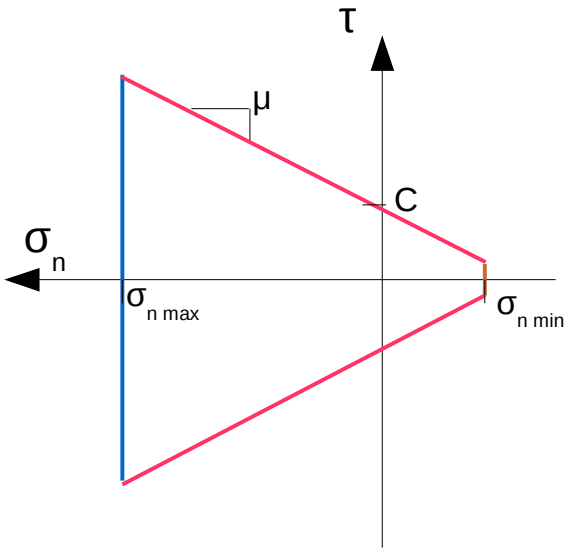

FIG. 5.3: The Coulomb criterion is used as a damage criterion (red line), truncated in tension at σ_{Nmin} (orange line). The blue line is a suggested ridging criterion if the EB rheology is used as a standalone framework.

For high degrees of confinement, when $\sigma_N \gg (\tau - C)/\mu$, failure cannot occur through the Coulomb criterion. This corresponds to the 'open end' of the Coulomb criterion, which is not physically correct as the ice cannot withstand infinitely large normal stresses. Instead, the ice fails through a different mechanism, which corresponds to ridging. Measurements of in-situ sea ice stress states are bounded by a compressive strength $\sigma_{Nmax} \simeq 100\,\text{kPa}$. If the EB framework is considered as 'standalone', the concept of compressive strength could be used as a very simple model of ridging, where the criterion for ridging would be $\sigma_N = \sigma_{Nmax}$ (figure 5.3). As a first approximation, we assume that ridging is followed by refreezing of the ice rubble, so that the overall process strengthens the ice cover. Then, if an element i reaches the ridging criterion, the effect of ridging could be represented as an increase of d :

$$d_i(t + \Delta t) = d_i(t)\, d_r \tag{5.7}$$

where d_r is an empirical parameter slightly larger than one. In a global sea ice model, where ridging is accounted through a dedicated scheme (Rothrock, 1975), the ice thickness can increase when ridging occurs, which increases as well the ice stiffness K (eq. 5.2). In this case, modifying the damage parameter d as described by equation 5.7 does not appear relevant.

5.2.3 Healing

When the temperature conditions allow freezing, fractures and leads in the sea ice cover can heal. This process, which strengthens the ice stiffness, is refered to as healing, by opposition to damage. Healing is therefore strongly coupled to the ice thermodynamics. Ice growth in fractures is a complex non-linear problem (Petrich *et al.*, 2007; Alexandrov *et al.*, 2006; Wettlaufer *et al.*, 2000) ; moreover the fractures are not represented explicitely in the EB model. An accurate description of such a complex process is out of scope here. Instead, a parameterization of the healing function was considered using a simple analogy with ice growth. The simplest approximation of ice growth, for a given constant air temperature T_a below the water freezing point T_f, is roughly a square-root function of the freezing degree-days (Maykut, 1986), i.e. the product of time and degrees below the freezing point. We make the hypothesis that healing acts similarly on the damage parameter d following,

$$d(t) = k\sqrt{t\,(T_f - T_a)}, \quad \text{with } 0 < d \leq 1, \tag{5.8}$$

where t is time and k is a constant. If we consider T_a constant, the incremental evolution of d is given by :

$$\frac{\partial d}{\partial t} = \frac{k\sqrt{(T_f - T_a)}}{2\sqrt{t}}. \tag{5.9}$$

$d(t)$ can be substituted in the right member of the equation,

$$\frac{\partial d}{\partial t} = \frac{k^2\,(T_f - T_a)}{2d(t)} = \frac{1}{t_h d(t)} \tag{5.10}$$

where t_h is a characteristic time varying as the inverse of the temperature difference that can be written as $t_h = \beta/\,(T_f - T_a)$ for $T_a < T_f$ and $t_h = \infty$ for $T_a \geq T_f$. β is an empirical constant of dimension time times Kelvin, which can be estimated from sensitivity tests. Finally, integrated over a time step Δt, the evolution of damage parameter due to healing is given by,

$$d(t + \Delta t) = d(t) + \frac{\Delta t}{t_h d(t)}, \quad \text{with } 0 < d \leq 1. \tag{5.11}$$

Note that t_h represents a characteristic time for healing which can be compared, in terms of order of magnitude, to observations of ice growth at a given temperature difference $(T_f - T_a)$. Figures 5.4 and 5.5 illustrate the evolution of the healing rate and the associated increase of d as a function of time and temperature. By opposition to damage, healing is not a threshold mechanism but a continuous process. Equation 5.11 is therefore applied to all elements at each time step. Healing is assumed to contribute only to recover the decrease of elastic stiffness due to damaging, i.e. the maximal value of d is one. Once $d = 1$ is reached, the elastic stiffness can only increase through an increase of ice thickness h or concentration c. The parameterization of healing is such that its effect nearly vanishes on undamaged elements or when temperature conditions do not allow freezing. On the other hand the effect of healing is large for strongly damaged elements. Note that in a global dynamic-thermodynamic sea ice model, the heat fluxes computed by the thermodynamic component could be used to provide a more accurate parameterization of the healing function. The effect of thermodynamics on the ice elastic stiffness is twofold, since K depends on the ice thickness h (eq. 5.2) but also on d which can heal through a process analogous to ice growth. However, these two effects correspond to different scales, since the ice thickness h is a rather smooth field as it is represented in models, whereas d is local and can show strongly heterogenous patterns.

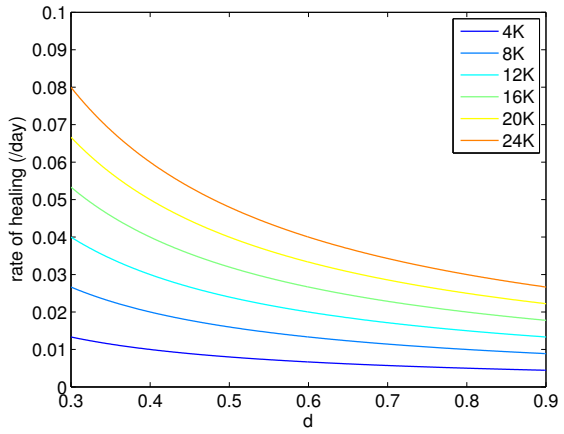

FIG. 5.4: Daily rate of healing $\frac{\partial d}{\partial t}$ as a function of the damage parameter d for different temperatures $T_f - T_a$ (K). For this example, the constant parameter β was arbitrarily set to $\beta = 10^3$ day.K^{-1}.

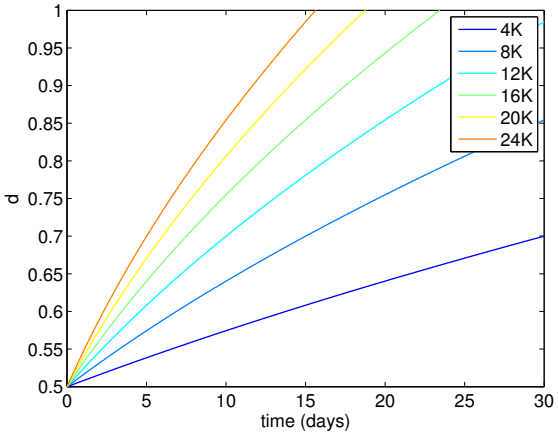

FIG. 5.5: Evolution of d due to healing as a function of time for different temperatures $T_f - T_a$ (K) and an initial value of $d(0) = 0.5$ ($\beta = 10^3$ day.K^{-1}).

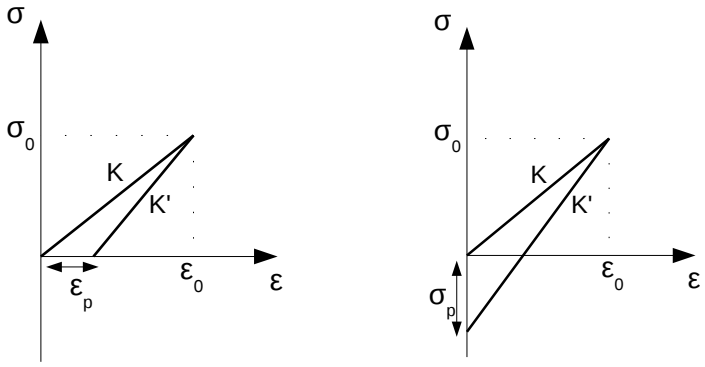

FIG. 5.6: When healing increases the stiffness from K to K', permanent deformation (ϵ_p, left panel) or permanent stress (σ_p, right panel) can be applied to maintain the strain and stress in a similar state (illustration for a 1D case).

In the field, refreezing can only occur on stress free surfaces, i.e. on open water areas such as leads and fractures. These stress free surfaces are not represented explicitely in the EB rheology where the ice cover is considered as a continuum and stresses are accounted at the element scale. This means that the increase of elastic stiffness associated with healing can induce an increase of stress or strain at the element scale. Such variation is unphysical and it is due to the model formulation. A way to avoid this artifact is to apply permanent deformations or permanent stresses in order to maintain the element mechanical state identical before and after healing. Figure 5.6 provides a schematic explanation of the role of such permanent deformation or stress in a 1D case. A physical basis for such permanent deformation/stress can also be formulated. As healing consists in filling fractures with a solid material, i.e. new ice, it fixes/immobilizes the current state of deformation. The application of the permanent deformation or stress describes this process. In the finite element application of the EB rheology, we have chosen to use permanent stresses. The computation is illustrated using the 1D analogy. With the notations of figure 5.6 we can write :

$$\sigma_0 + \sigma_p = K'\epsilon_0 \text{ , with } \sigma_0 = K\epsilon_0, \tag{5.12}$$

so that σ_p can be expressed as,

$$\sigma_p = (K' - K)\,\epsilon_0, \tag{5.13}$$

where K and K' are the elastic stiffnesses before and after healing respectively. In the 2D case, the permanent stress at the element scale $\left[\underline{f_p}\right]_{el}$ is obtained by multiplying the stiffness tensor $\left[(K' - K)\,\underline{\underline{D}}\right]_{el}$ with the element strain tensor $[\epsilon_{ij}]_{el}$,

$$\left[\underline{f_p}\right]_{el} = \left[(K' - K)\,\underline{\underline{D}}\,\epsilon_{ij}\right]_{el} \tag{5.14}$$

The stresses are calculated individually for each element and then assembled in a global vector $\underline{f_p}$. Finally, the permanent stresses are cumulated over all timesteps,

$$\underline{F_p} = \sum_{n=t_0}^{t} \underline{f_p}(n), \tag{5.15}$$

where the resulting term F_p is applied to the momentum equation (eq. 5.3).

5.3 Preliminary results from standalone simulations

A first application of the EB rheology considered short term simulations of the Arctic sea ice cover to investigate the development and propagation of damage, and associated strain fields (Girard *et al.*, 2010b). This study considered 3-day simulations driven by wind stress fields. The simulations only included the damage part of the EB rheology, considering that healing does not have a significant effect on such a short time period, the ice acceleration was also neglected using a 'quasi-static' approximation. This first application of the rheology gave an estimate of the model mechanical parameters : the Young modulus Y and the range of the cohesion C. Moreover, the results showed a good representation of the shear faulting mechanism that accomodates most of sea ice deformation. The distributions of strain-rates and spatial scaling law of sea ice deformation were also well captured by the EB rheology. Overall, the results argued that the properties of sea ice deformation emerge from the elasto-brittle ice mechanical behavior.

In this section, preliminary results from simulations including the effect of healing are reported and suggestions for further analyses are provided. The results presented below were obtained with idealised simulations in quasi-static conditions (acceleration neglected), considering a rectangular mesh forced in uniaxial compression. The simulation settings are close to those described in chapter 3 where only damage was considered. Unfortunately, the current state of development has not allowed us to performed a robust statistical analysis such as presented in chapter 3.

5.3.1 Numerical methods

The simulations were obtained with a finite element application based on a continuous and linear discretisation. A rectangular mesh, with height to width ratio of 2, made of triangular elements is used. The orientation of the triangles is chosen randomly in order to avoid preferential directions in the mesh. The lower boundary of the mesh is fixed (no displacement), while the left and right boundaries can deform freely. The loading consists in uniaxial compression, applied by increasing the macroscopic strain on the upper boundary of the model at a fixed rate of $\dot{\epsilon}_{macro} = 10^{-7}$ per timestep (figure 5.7). The acceleration is neglected and the momentum balance simply reads (in force per unit area),

$$\underline{F_{ext}} + \nabla.\sigma_{ij} - \underline{F_p} = 0. \tag{5.16}$$

where the external force $\underline{F_{ext}}$ (per unit area) is applied to the upper boundary of the model in the vertical direction, with a magnitude determined so that the macroscopic deformation increases at the prescribed rate. The ice thickness and concentration are considered to be constant and equal to unity, $h = 1$ and $c = 1$ for all elements. The range of cohesion C is defined relatively to the Young modulus, with C ranging from 5.10^{-4} to $10^{-3}Y$. Every time a damage event occurs, a new cohesion is redrawn from the distribution to simulate an evolving disorder. All elements are initialised as undamaged, $d = 0$, and a damage parameter $d_0 = 0.1$ is applied. The set of model parameters is similar to the one used in chapter 3.

For this preliminary test, a constant characteristic time for healing t_h was used, which is equivalent to consider a constant temperature below freezing. A first set of simulations, based on a coarse mesh (960 elements), was performed to investigate the behavior of healing over a wide range of characteristic healing times $t_h/\Delta t$, from 5.10^2 to 10^9. This series also includes a simulation where healing has been desactivated for comparison. Two other simulations, based on a fine mesh (65058 elements), were performed to analyse the evolution of the deformation fields, using respectively $t_h/\Delta t = 3.10^4$ and no healing. To simplify the following explanations, the timestep is considered as $\Delta t = 1$.

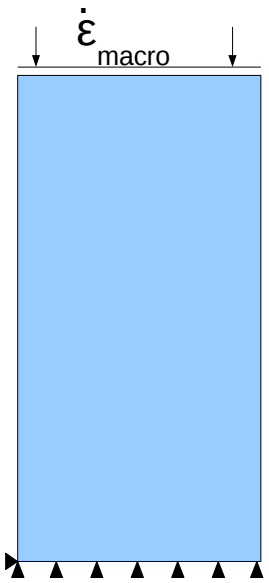

FIG. 5.7: Schematic view of the uniaxial compression test simulated

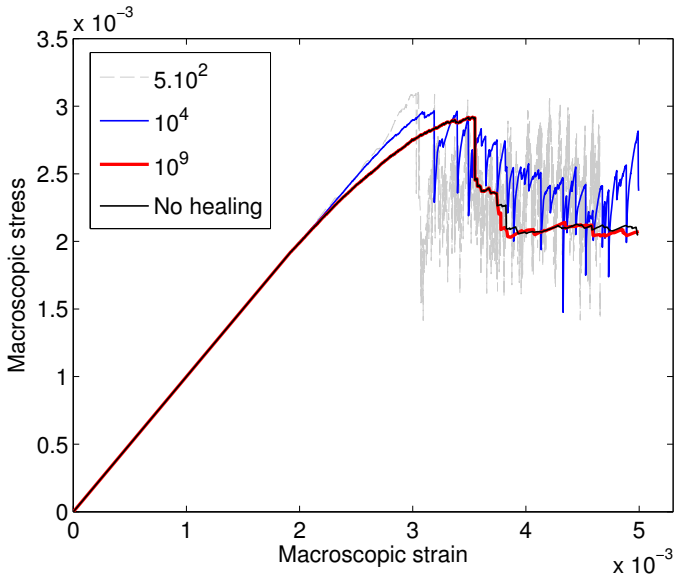

FIG. 5.8: Macroscopic strain versus stress for coarse mesh simulations for different values of the characteristic healing time t_h, and for a simulation without healing.

5.3.2 Macroscopic behavior and strain fields

We first consider the coarse mesh simulations and examine the macroscopic strain-stress curves obtained with different healing times t_h (figure 5.8). For the largest value $t_h = 10^9$, the macroscopic behavior ressembles closely the one obtained without healing. In this simulation, the evolution of damage is also similar to the case where healing is absent. In early stages of the simulation, damage is homogeneously scattered throughout the mesh and the macroscopic behavior is linear. Further on in the simulation, the damage activity increases and a deviation from elasticity is observed corresponding to a softening. Finally, a catastrophic avalanche of damage events occurs, spanning across the mesh, inducing a large drop in the macroscopic stress. After the catastrophic avalanche, damage events are mostly localised in the same band of strongly damaged elements. The fact that a similar behavior is obtained at large t_h and without healing ensures the continuity between the two situations, i.e. neglecting healing is equivalent to using an infinitely large healing time.

For $t_h = 10^4$, the effect of healing strongly affects the macroscopic strain-stress curve (figure 5.8). In the first stages of this simulation, the deviation from the linear elastic behavior is less marked than without healing, and the softening is delayed. Then, large successive drops in the macroscopic stress are observed. Between these large drops, recovery periods where stress increases can be identified. Similarly to a situation without healing, the first significant drop of macroscopic stress corresponds to a catastropic avalanche of damage events spanning the mesh. This first catastrophic event is followed by a stage where strongly damaged elements heal quickly, resulting in a temporary increase of the macroscopic stress, until the occurrence of another catastrophic event. This second catastrophic event results in a band of strongly damaged events spanning the mesh at a different location than the one resulting from the first catastrophic event. The sequence of catastrophic events and recovery periods is repeated several times. For $t_h = 500$, a similar behavior is observed but the frequency of the damaging/recovery cycles is larger.

This qualitative description is supported by the analysis of the simulations obtained with the fine mesh.

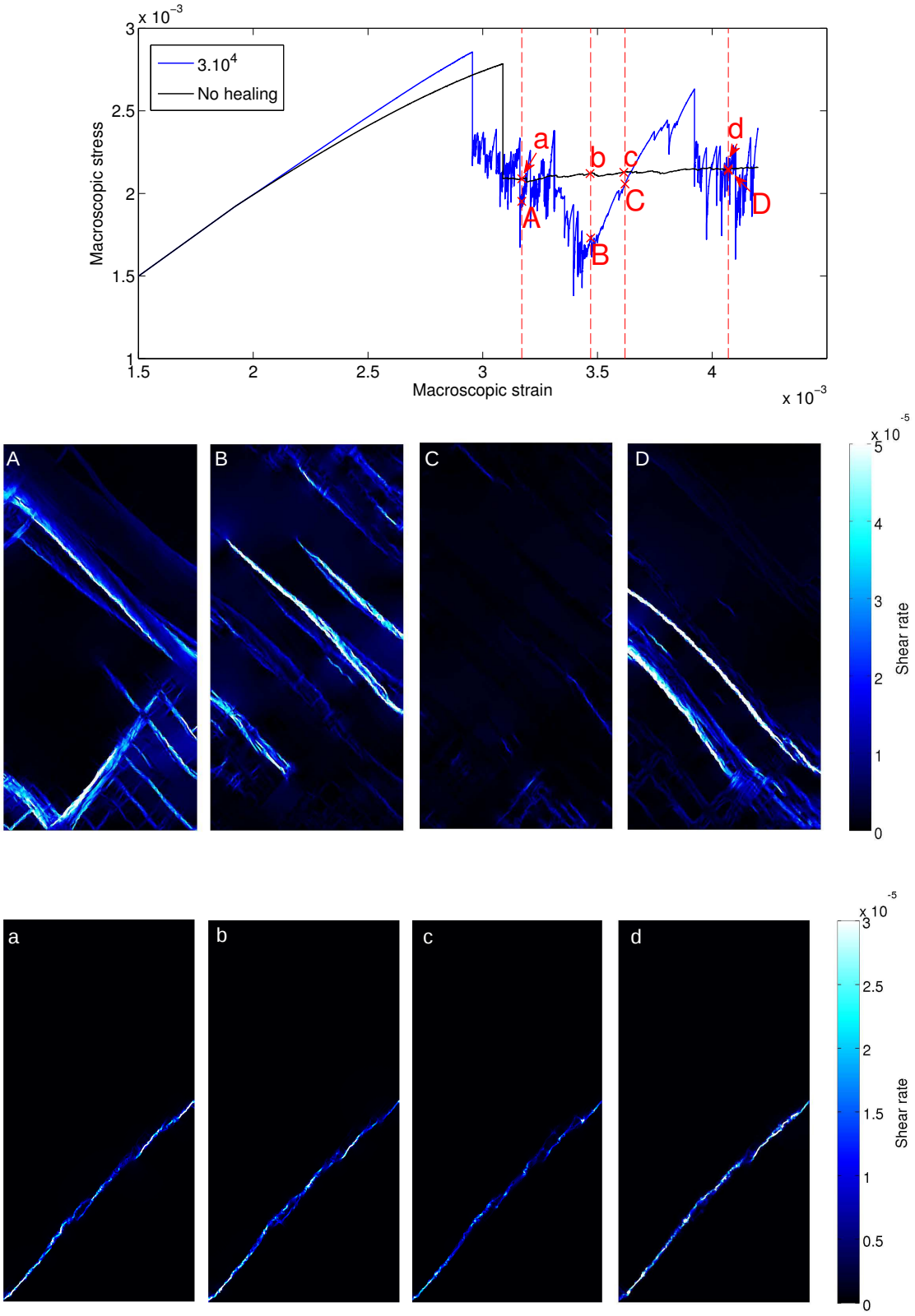

FIG. 5.9: Macroscopic strain-stress curves from two fine mesh simulations, with $t_h = 3.10^4$ and without healing (top panel). The other panels show shear rate fields, computed from the strain cumulated over 50 timesteps, for different states of the simulations, identified from capital letters for the simulation with healing and small letters for the simulation without healing.

For four macroscopic states following the first catastrophic event, the shear rate fields are computed (figure 5.9), where the shear rate is defined as,

$$\dot{\epsilon}_{shear} = \sqrt{\left(\dot{\epsilon}_{xx} - \dot{\epsilon}_{yy}\right)^2 + \left(2\dot{\epsilon}_{xy}\right)^2}. \tag{5.17}$$

The macroscopic strain-stress curves of the simulation with healing time $t_h = 3.10^4$ (figure 5.9) shows cycles of damaging and recovery periods, as described previously from figure 5.8. All shear rate fields show a strong localisation of the deformation. The two first fields (A and B) correspond to a period of intense damaging, with a decreasing macroscopic stress. The linear bands that accomodate most of the deformation have different locations in the two fields. Shear rate field C corresponds to a recovery period of increasing macroscopic stress and do not show large values. Finally, field D shows again a strong localisation of high shear rates in linear bands that do not correspond to the ones observed in fields A and B. On the other hand, shear rate fields from the simulation without healing also show a strong localisation of high shear values, but these high values are all accomodated by a linear band that persists in all fields (a,b,c and d).

5.3.3 Emergence of a marginally stable state ?

Simulations including only damaging processes are inevitably driven towards failure, e.g. the catastrophic damage event. In the vicinity of this catastrophic event, which is compared to a critical point, a divergence of the correlation length and spatial scale invariance are observed (chapter 3). In this case, no variations in time occur after the critical point since most of the deformation is accomodated by a persistant feature, as seen on panels a-d of figure 5.9. When healing is considered, important fluctuations are observed in time after the first catastrophic event. This raises the following questions regarding the statistical and scaling properties of the simulated deformation fields :

- Does a spatial scale invariance emerge ?
- Does a time invariance also emerge or does the time scale associated with healing impose a characteristic cycle ?
- Does the system reach a 'marginally stable state', fluctuating around a critical point ?

In the spatial domain, one can suspect that the scale invariance emerges similarly to simulations without healing, in the vicinity of the first catastrophic event. In the time domain, the evolution of the temporal correlation length needs to be investigated. The associated finite size effects and the possible inheritance from the time scale associated with healing should also be characterised. Such analysis has not been achieved yet but will be conducted to answer these questions through an active collaboration with the Laboratoire de Géophysique Interne et Tectonophysique (LGIT), Grenoble, France.

The questions raised in this section bridge the fundamental study of brittle deformation of geophysical objects and sea ice modelling. On a more practical point of view the statistical and scaling properties of ice deformation provide a powerful metric to evaluate rheological models. This is another reason for considering these aspects during the development of the model.

5.4 Towards the implementation of the EB rheology within a global sea ice model

The mechanical framework of the EB rheology is based on continuum mechanics and could therefore be readily implemented within a global sea ice model. However, the use of an elastic constitutive law raises an important difficulty for the implementation. This section discusses this difficulty and describes the interactions between the rheology and the ice state and dynamics.

Current global sea ice models are all based on a fixed grid where the ice velocities are computed within a Eulerian framework. In such a case, the use of an elastic constitutive law is problematic since it requires a strain field while only the strain-rate field is provided in a Eulerian approach. The elastic-plastic rheology of the AIDJEX model already faced such a problem (Coon *et al.*, 1974) and one of the possibility envisaged was to indefinitely keep track of all strain states. This required an important extra computational load which was not feasible numerically, especially at that time (Colony & Pritchard, 1975). Note that in the case of Lagrangian dynamics the strain field is directly calculated and the problem does not exist. While determining the exact ice strain field under Eulerian dynamics is dubious, an approximated strain field could be obtained more easily and could be sufficient for a sea ice model application. A possible way to perform such an approximation is to keep track of preceding strain-rate fields over a fixed period of time t_c and to estimate the strain field using an evanescent memory,

$$\epsilon_{ij}(t) = \sum_{n=t-t_c}^{t} \gamma(n)\dot{\epsilon}_{ij}(n)\Delta t \tag{5.18}$$

where $\epsilon_{ij}(t)$ is the estimated strain, $\dot{\epsilon}_{ij}(n)$ are the preceding strain-rates, Δt is the timestep length and $\gamma(n)$ is a weighting function. A lower limit for the time scale t_c would be the synoptic time scale (~ 1 week), i.e. the time scale over which the main forcing term, namely the wind stress, shows coherence and memory effects. On the other hand, scaling analysis shows that there is no characteristic time scale for sea ice deformation at least between an hour and a month (Rampal *et al.*, 2008). This means that long term memory effects of sea ice dynamics would be neglected if the ice strain is estimated with the preceding procedure and $t_c \simeq 1$ week. The methodology should be tested to assess its reliability and to determine the sensivity of the simulated ice dynamics with the time scale t_c.

In the framework presented in this chapter, the permanent stresses associated to healing are cumulated over time (eq. 5.15). In simulations based on an Eulerian framework, if the ice strain is estimated using the evanescent memory (eq. 5.18) assuming that the memory of deformation is lost after a given time t_c, then the evanescent memory should also be applied to the permanent stresses :

$$\underline{F_p}(t) = \sum_{n=t-t_c}^{t} \gamma(n)\underline{f_p}(n). \tag{5.19}$$

The interactions between the EB rheology and the other model components are through the ice thickness and concentration, for the determination of the elastic stiffness (eq. 5.2). The rheology provides the stress field of the momentum equation (eq. 5.3). All preliminary applications of the EB rheology were based on a 'quasi-static' approximation, where the acceleration term $\frac{\partial u}{\partial t}$ was neglected, as in a solid mechanics framework. In a global sea ice model, the quasi-static approximation could be maintained during the sub-iterations related to damage propagation (fig. 5.2) as the time scale associated is small and the associated ice acceleration could be neglected. This approximation could reduce the computation time and limit the stability problems associated with the resolution of the momentum equation, but it remains to be tested. We are currently working on the implementation of the EB rheology within the Second-generation Louvain-la-Neuve

Ice-ocean Model (SLIM), through a collaboration with the Georges Lemaître Centre for Earth and Climate Research. The rheology will first be tested in a Lagrangian configuration. This will allow several tests in order to determine the model parameters such as the cohesion C, the Young modulus Y and the parameterization of healing. Secondly, the Eulerian configuration will be tested to investigate the validity of the evanescent memory (eq. 5.18) described in this section. In future developments based on the EB framework, the validation of the numerical methods and the model convergence should be based on statistical properties, as suggested in chapter 2. This differs from criterions used to determine the convergence of classical models based on a fluid mechanics approach such as the VP rheology. There is a non-deterministic aspect in the EB framework, since the cohesion C is randomly drawn from a distribution at the begining of the simulations and redrawn after each damage event. In order to run a similar simulation several times, as often needed for the validation of numerical methods, a random number generator that can be reset at a given state should be used.

5.5 Discussion and conclusions

This section discusses the advantages and the expected limitations of the EB mechanical framework for sea ice models. The differences with other approaches followed to account for the brittle behavior of sea ice in models are also discussed. The main mechanism represented by the EB framework is damage at the local element scale, coupled to long-range elastic interactions that can occur in the sea ice cover. This mechanism has an essential role on the brittle deformation of sea ice. A first application of the EB rheology showed that long-range elastic interactions allow the emergence of heterogeneous deformation fields with similar statistical and scaling properties as observed for sea ice. In particular, the power law scaling of sea ice deformation, expressed as $\langle \dot{\epsilon}_{tot} \rangle \sim L^{-b}$, where $\dot{\epsilon}_{tot}$ is the total deformation rate and L the spatial scale, was captured in these EB simulations, with an exponent $b = 0.1$ (Girard *et al.*, 2010b). To our knowledge, it is the first time that a sea ice model captures such properties of sea ice deformation, which is a noteworthy point. The evolution of the statistical properties with time and the temporal scaling properties of the simulated ice deformation remains to be investigated, suggestions for such analysis were presented in section 5.3.3.

One can question to what extent long-range elastic interactions are a relevant mechanism for sea ice deformation. When ice concentrations are not close to one, such as in the marginal ice zone, stresses cannot be transmitted as well as in a more continuous ice cover. In this case, the ice cover consists of floes drifting as a granular flow (Feltham, 2005), or almost freely when ice concentrations are even lower (figure 5.10). While it is not possible to define clear boundaries between these different behaviors, one can suspect that the solid plate approach that we have presented is most relevant for ice concentrations above 95%. At lower ice concentrations, the elastic stiffness decreases quickly due to the exponential dependance of relation 5.2 and the stresses may well decrease towards zero, simulating a free drift case. However, considering the ice cover as a continuous elastic plate when it consists of discrete floes appears inappropriate. Instead a threshold concentration could

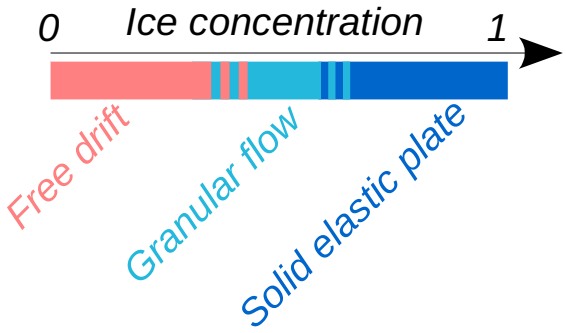

FIG. 5.10: Schematic and unscaled view of the different mechanical behaviors of the sea ice cover.

be defined, below which the rheology is simply desactivated. The EB rheology is not particularly relevant either in regions where the ice dynamics is strongly influenced by the coastal topography or by the forcing conditions, such as in the Fram Strait and along the east Greenlandic coast.

Stern & Lindsay (2009) recently presented a thorough analysis of the spatial scaling properties of sea ice deformation using the RGPS observations from 7 years, recorded between october and the end of july. The scaling properties of sea ice deformation remain for all months of the year, suggesting a persistance of the elasto-brittle behavior, but a distinct annual cycle of the scaling exponent b is observed. The exponent becomes larger in summer as the ice pack weakens and internal stresses are not as readily transmitted over long distances. Moreover, b tends to be larger where the concentration of multiyear ice is low, consistent with a thinner and weaker ice pack. The value $b = 0.1$, obtained from the first application of the EB rheology, is typically found for a winter ice pack or for multiyear ice. As expected, this suggests that the EB rheology is mostly adapted to capture the behavior of sea ice at very high concentrations, as seen in winter. However, this first application considered only short simulations and further work is needed to assess if the EB rheology, once included in a global sea ice model, could capture the variations of the spatial scaling properties. Consequently further work is needed to assess over which range of pack ice concentrations the framework of the EB rheology is relevant.

Among the other approaches followed to account for the brittle behavior of sea ice, the elasto-decohesive model considers many of the same issues adressed in this chapter (Schreyer *et al.*, 2006). This model accounts for failure by a loss of cohesion rather than damage and the leads/fractures are represented explicitely, instead of using a continuum damage formulation. However, no attempt has been made so far to include ice freezing, or healing in our terms, to the elasto-decohesive model. Moreover, the explicit representation of leads as discontinuities might complicate the implementation of such a rheology within a coupled ocean/sea ice model. The EB rheology is based on simpler assumptions than the elasto-decohesive model, since it considers the sea ice cover as fully continuous. The first results reported in this chapter and earlier (Girard *et al.*, 2010b) were however very promising. The inclusion of the EB rheology within a global sea ice models is now needed to investigate the model behavior on a broad range of spatial and temporal scales. In a more general perspective, the EB framework follows on from statistical models of fracture but it is pioneering in the fact that it is a tensorial model accounting for healing processes. This opens broad perspectives for the fundamental study of brittle deformation of geophysical objects on a broad range of scales.

Chapitre 6

Conclusions et perspectives

6.1 Résumé des conclusions

Cette section résume les conclusions principales des travaux que j'ai mené au cours de cette thèse. Une première série de conclusions concerne l'évaluation des modèles rhéologiques de banquise ainsi que les limitations du cadre de modélisation visqueux-plastique (VP) actuellement utilisé dans les modèles globaux de banquise eux-même insérés dans les modèles de climat (chapitre 2) :

- L'évaluation des vitesses de déformation de la banquise simulées par les modèles ne peut pas être basée sur une simple comparaison de valeurs moyennes ou d'écarts types. Au contraire, cette évaluation doit prendre en compte les propriétés statistiques et propriétés d'échelle de la déformation.
- Les fonctions de distributions (PDFs) de vitesses de déformation issues d'observations ont trait au « hasard sauvage » et présentent des queues en loi puissance, tandis que les PDFs des vitesses de déformation issues de modèles VP sont dans le bassin d'attraction gaussien et sous-estiment largement les fortes valeurs.
- Les lois d'échelles spatiales et temporelles qui caractérisent l'hétérogénéité et l'intermittence du champ de déformation de la banquise ne sont pas reproduites par les modèles VP. Cela signifie que les modèles VP sont incapables de représenter les corrélations spatiales et temporelles du champ de déformation de la banquise.
- Les propriétés statistiques et propriétés d'échelle de la déformation de la banquise émanent du comportement mécanique de la banquise. Le fait que ces propriétés ne soit pas reproduites par les modèles VP suggère que le cadre de modélisation mécanique est inadapté à la banquise.
- Augmenter la résolution des modèles VP ou la résolution des champs de forçage utilisés par ces modèles ne permettra pas d'améliorer de manière significative la représentation de la déformation de la banquise.

Une seconde série de conclusions découle de l'étude fondamentale de la rupture en tant que point critique à l'aide d'un modèle d'endommagement progressif et de simulations de compression uniaxiale (chapitre 3) :

- La taille et l'énergie dissipé par les évènements d'endommagement sont distribués suivant une loi puissance qui présente une coupure liée à un effet de taille finie. L'effet de taille finie peut également être caractérisé à partir des fonctions de corrélation spatiale des évènements d'endommagement.
- L'approche à la rupture est caractérisée par une divergence de la longueur de corrélation spatiale. Celle-ci est estimée à partir des propriétés d'échelle du champ de déformation, ainsi qu'à l'aide des fonctions

de corrélation des évènements d'endommagement. Ces résultats suggèrent que la rupture peut être interprétée comme un point critique.
- Des propriétés multifractales du champ de déformation émergent à l'approche de la rupture. Au point critique, ces propriétés sont proches de celles caractérisant la déformation de la banquise.

Ce modèle d'endommagement progressif constitue le coeur de ce que nous avons baptisé la rhéologie élasto-fragile (EB) pour la banquise. Dans le chapitre 4 j'ai présenté une première application idéalisée de la rhéologie EB à la banquise arctique. Les champs de déformation simulés par la rhéologie EB en réponse aux efforts engendrés par le vent sur des périodes de 3 jours ont été analysés en termes de propriétés statistiques et de propriétés d'échelles. Les résultats ont été comparés, par le biais de ces propriétés, à des vitesses de déformations observées ainsi qu'à des simulations basées sur la rhéologie VP. Les conclusions suivantes ont été formulées à l'issue de cette étude :

- Dans les simulations EB, la relaxation de contrainte engendrée par un évènement d'endommagement peut se propager à grande distance et entraîner une avalanche d'évènements d'endommagement. Il résulte de ce processus un champ hétérogène où l'endommagement est localisé le long de zones quasi-linéaires qui accommodent une grande part de la déformation cisaillante.
- Une correlation élevée entre les champs de vitesses de cisaillement et de divergence suggère que le mécanisme de déformation le long de failles cisaillantes associé à de la dilatance est bien représenté par la rhéologie EB.
- Les fonctions de distribution de vitesses de déformation obtenues par les simulations EB sont très proches des fonctions de distribution issues d'observations (RGPS). La loi d'échelle spatiale du champ de déformation est également reproduite dans ces simulations, tandis qu'aucune des propriétés statistiques caractérisant la déformation de la banquise n'est restituée dans les simulations basées sur la rhéologie VP. Ces premiers résultats prometteurs motivent donc l'implémentation de la rhéologie EB dans un modèle global de banquise.

Finalement, le chapitre 5 présente l'architecture complète du modèle rhéologique elasto-fragile en vue d'une implémentation dans un modèle global de banquise. Les points que j'ai abordé au cours de ce chapitre sont les suivants :

- Une présentation exhaustive du mécanisme d'endommagement qui complète la description plus succinte du chapitre 4.
- L'implémentation d'une loi de cicatrisation, qui décrit le recouvrement des propriétés mécaniques de la banquise lors du regel des failles et des fractures. Cette loi est établie à partir d'une analogie simple avec la cinétique de l'épaississement de la banquise, en fonction d'un temps charactéristique de cicatrisation qui varie lui même avec la température de l'air. Le regel étant un processus qui 'fige' l'état de déformation, l'implémentation de la cicatrisation passe également par la prise en compte de forces permanentes qui décrivent ce processus.
- Des résultats préliminaires issus de simulations incluant la cicatrisation montrent la continuité entre un cas sans cicatrisation et un temps de cicatrisation très grand, i.e. une cicatrisation très lente. Les champs de déformation obtenus lorsque la cicatrisation est prise en compte montrent une forte fluctuation dans l'espace et dans le temps des zones quasi-linéaires qui accomodent une grande partie de la déformation. Ces fluctuations devront être caractérisées par une analyse d'échelle spatio-temporelle de la déformation.

- Une méthodologie visant à estimer le champ de déformation à partir d'une 'mémoire evanescente' est présentée. Cette méthodologie vise à résoudre la difficulté principale que posera l'implémentation de la rhéologie EB dans un schema Eulérien, qui reste la norme pour les modèles globaux de banquise ou de climat.

6.2 Discussion et perspectives

6.2.1 Intérêts et limites du cadre de modélisation élasto-fragile

Le cadre de modélisation elasto-fragile (EB) développé au cours de cette thèse considère la banquise comme une plaque élastique continue où les processus de fracturation sont représentés par un niveau d'endommagement local, associé à des interactions élastiques à grande distance. Une première application de la rhéologie EB a mis en évidence que les interactions élastiques à grande distance permettent l'émergence de champs de déformation hétérogènes dont les propriétés statistiques et propriétés d'échelle spatiale sont similaires à celles observées pour la banquise. Ces résultats sont remarquables car c'est la permière fois qu'un modèle de banquise parvient à reproduire les propriétés caractéristiques de la déformation de la banquise.

En considérant la banquise comme un solide élastique continu, l'approche que nous avons choisie est particulièrement adaptée à représenter le comportement d'un pack de banquise très dense, i.e. où la fraction/concentration de glace est supérieure à 95%. Lorsque la concentration de glace diminue, les contraintes ne peuvent plus être transmises aussi bien que dans une banquise continue. Dans ce cas, la banquise est constituée de floes distincts, dérivant avec un comportement granulaire ou même librement lorsque la concentration de glace est suffisamment faible pour qu'il n'y ait presque plus d'interactions entre les floes. Il apparait donc que la rhéologie EB est particulièrement adaptée à représenter le comportement mécanique d'une banquise de type hivernale caractérisée par une concentration élevée. Par contre, en dessous d'un certain seuil de concentration, elle ne permet pas de représenter le comportement d'une banquise plus disloquée.

C'est lors de la saison hivernale que le comportement mécanique de la banquise a le plus d'influence sur sa déformation et sa dérive. La banquise couvre alors tout l'océan Arctique où elle est confinée, et les contraintes internes peuvent être élevées. D'autre part, c'est également au cours de la saison hivernale que les échanges de chaleur mer-air peuvent être les plus intenses, due à une forte différence de température entre ces deux milieux. Dans les modèles globaux de banquise ou de climat, il apparait donc essentiel de représenter correctement les propriétés statistiques de déformation de la banquise, qui contrôlent ces échanges de chaleur. Ces remarques soutiennent l'utilisation de la rhéologie EB dans des modèles globaux, pour des application climatiques, puisqu'elle donne une bonne représentation du comportement mécanique de la banquise hivernale. Pour de telles applications, la limite de la rhéologie pourrait être prise en compte en définissant une concentration de glace seuil en dessous de laquelle la rhéologie serait désactivée. Cela revient à considérer un champ de contrainte nul et une banquise en dérive libre. Plus de travaux sont nécessaires pour tester la validité de ces hypothèses et estimer la valeur d'une éventuelle concentration seuil.

En Arctique, les glaces pluri-annuelles ont subit un déclin rapide au cours des dernière années et de nombreuses études concluent que leur disparition durant les prochaines décennies semble inéluctable (Serreze

et al., 2007; Lemke *et al.*, 2007). Cela se traduit par une disparition progressive de la banquise estivale. La banquise hivernale a subit une importante perte d'épaisseur mais son étendue ne diminue que faiblement comparée à la banquise estivale (Stroeve *et al.*, 2007). Le contraste que l'on observe actuellement entre la banquise estivale, de faible étendue et de concentration peu élevée, et la banquise hivernale, qui atteint une concentration proche de 100% sur tout le bassin Arctique, va donc s'amplifier (figure 6.1). A terme, la banquise Arctique pourrait donc devenir saisonière, avec une couverture hivernale de faible épaisseur mais une étendue considérable, qui pourrait disparaître au cours de chaque été. Dans ce contexte, le compromis que nous présentons considérant que la banquise a (i) un comportement élasto-fragile pour des concentrations élevées, ou (ii) une dérive libre, semble bien adapté pour des applications climatiques, puisque la transition entre ces deux états est amenée à être de plus en plus rapide.

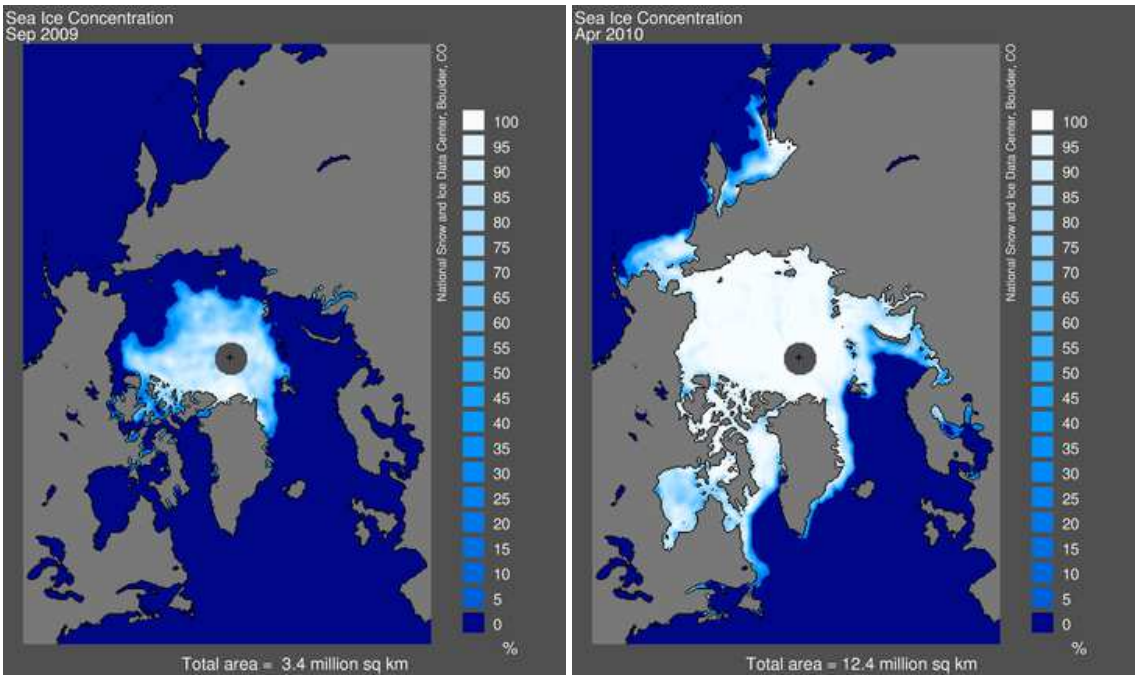

FIG. 6.1: Concentration mensuelle moyenne de la banquise en septembre 2009 (à gauche) et en avril 2010 (à droite) estimée à partir données SSMIS DMSP-F17, source NSIDC.

Nous travaillons actuellement à l'implémentation de la rhéologie EB dans le modèle global de banquise Second-generation Louvain-la-Neuve Ice-ocean Model (SLIM), par le biais d'une collaboration active avec le Centre de recherche sur la Terre et le climat Georges Lemaître, à Louvain-la-Neuve, Belgique. Le modèle rhéologique sera prochainement testé dans une configuration Lagrangienne, puis dans une configuration Eulérienne du modèle SLIM. A terme, l'objectif de cette collaboration est d'intégrer la rhéologie EB dans le modèle couplé océan-banquise NEMO-LIM, utilisé au niveau européen pour l'étude du climat.

6.2.2 Perspectives pour l'étude de la déformation fragile des objets géophysiques

Les travaux présentés dans le chapitre 3 s'inscrivent dans le contexte plus général de l'étude de la déformation fragile des objets géophysiques. Dans cette étude nous n'avons considéré que les processus d'endommagement, sans prendre en compte la cicatrisation. Dans ce cas, le système est inévitablement conduit à la rupture. Nous avons montré que l'approche à la rupture était caractérisée par une divergence de la longueur de corrélation spatiale et l'émergence de propriétés d'échelle de la déformation. A la rupture, que nous avons comparée à un point critique, les propriétés d'échelle de la déformation obtenues sont proches de

celles observées pour la banquise et pour la croûte terrestre. Ces résultats soutiennent les hypothèses émises sur l'origine de ces propriétés d'échelle (Weiss *et al.*, 2007; Rampal, 2008; Cowie *et al.*, 1995), qui émergent principalement :

(i) d'un mécanisme à seuil qui entraîne une redistribution des contraintes élastiques,

(ii) de l'hétérogéneité du matériau, réprésentée par une distribution aléatoire des seuils de rupture,

(iii) d'interactions élastiques à grande distance.

L'interpretation de l'approche à la rupture que nous avons proposée, basée sur la divergence de la longueur de correlation, diffère de celle émise par d'autres études, considérant comme précurseur à la rupture une décroissance de la dimension de correlation des évenements d'endommagement (Hirata *et al.*, 1987; Cowie *et al.*, 1995; Amitrano, 2006) ou une décroissance de l'exposant caractérisant la distribution d'énergie dissipée par endommagement (Amitrano *et al.*, 1999).

D'autre part, le comportement critique que nous avons mis en évidence dans cette étude ne semble pas influencé par le mode de chargement (constitué de deux manières différentes d'imposer une compression uniaxiale). Dans le cadre de l'application à la banquise Arctique présenté dans le chapitre 4, un autre type de chargement a été utilisé, sous forme d'un champ de forces superficielles décrivant l'effort exercé par le vent sur la glace. Les propriétés statistiques et propriétés d'échelle de la déformation obtenues pour cette application sont pourtant très proches de celles obtenues pour les essais de compression uniaxiale. Existerait-il un caractère 'universel' aux propriétés d'échelles décrivant la déformation fragile ?

La prise en compte du processus de cicatrisation (chapitre 5) ouvre de nombreuses perspectives pour l'étude de la criticalité de la déformation des objets géophysiques. La possible criticalité de la déformation et de la fracturation de la croûte terrestre est un problême de longue date qui est encore d'actualité (Sornette & Sornette, 1989). Si les processus de cicatrisation des failles de la croûte terrestre apparaissent difficiles à décrire (Gratier & Gueydan, 2005), l'étude de la banquise nous a permis de présenter une loi de cicatrisation simple déduite d'une analogie avec la cinétique du regel, qui offre une base idéale à une étude théorique. Les résultats préliminaires présentés dans le chapitre 5 donnent un premier aperçu de la richesse du comportement simulé. Ce travail se poursuivra dans le cadre de la thèse de Florent Gimbert, au Laboratoire de Géophysique Interne et de Tectonophysique (LGIT), à Grenoble, par une analyse d'échelle spatio-temporelle visant à caractériser les propriétés des champs de déformation simulés. Cette analyse permettra d'explorer l'intermittence et l'hétérogénéité de la déformation, mais aussi d'examiner l'existence d'un possible état 'marginalement stable' dans lequel le système reste proche du point critique.

Bibliographie

Aagaard, K. A., & Carmack, E. C. 1989. The role of sea ice and other fresh water in the Arctic circulation. *J. Geophys. Res.*, **94**, 14485 – 14498.

Alava, M. J., Nukala, P.K.V.V., & Zapperi, S. 2006. Statistical models of fracture. *Advances in Physics*, **55**, 349.

Alexandrov, D. V., Malygin, A. P., & Alexandrova, I. V. 2006. Solidification of leads : approximate solutions of non-linear problem. *Annals of Glaciology*, **44**, 118 – 122.

Amitrano, D. 2003. Brittle-ductile transition and associated seismicity : Experimental and numerical studies and relationship with the b value. *J. Geophys. Res.*, **108**(2044).

Amitrano, D. 2006. Failure by damage accumulation in rocks. *International Journal of Fracture*, **139**, 369.

Amitrano, D., & Helmstetter, A. 2006. Brittle creep, damage and time to failure in rocks. *J. Geophys. Res.*, **111**(B11201).

Amitrano, D., & Schmittbuhl, J. 2002. Fracture roughness and gouge distribution of a granite shear band. *J. Geophys. Res.*, **107**.

Amitrano, D., Grasso, J.R., & Hantz, D. 1999. From diffuse to localised damage through elastic interaction. *Geophysical Research Letters*, **26**, 2109 – 2112.

Amitrano, D., Grasso, J. R., & Senfaute, G. 2005. Seismic precursory patterns before a cliff collapse and critical point phenomena. *Geophys. Res. Lett.*, **32**(L08314).

Anderson, E. M. 1905. The dynamics of faulting. *Trans. Edinb. Geol. Soc.*, **8**, 393 – 402.

Andreas, E.L., & Cash, B.A. 1999. Convective heat transfer over wintertime leads and polynyas. *J. Geophys. Res.*, **104**, 25721 – 25734.

Barnier, B., Madec, G., Penduff, T., Molines, J.M., Tréguier, A.M., Beckmann, A., Biastoch, A., Boning, C., Dengg, J., Gulev, S., Sommer, J. Le, Rémy, E., Talandier, C., Theetten, S., Maltrud, M., & Lean, J. Mc. 2006. Impact of partial steps and momentum advection schemes in a global ocean circulation model at eddy permitting resolution. *Ocean Dynamics*, **56**, 543 – 567.

Bouillon, S., Maqueda, M. A. Morales, Legat, V., & Fichefet, T. 2009. An Elastic-Viscous-Plastic Sea Ice Model formulated on Arakawa B and C Grids. *Ocean Modelling*.

Bowman, D. D., Ouillon, G., Sammis, C. G., Sornette, A., & Sornette, D. 1998. An observational test of the critical earthquake concept. *J. Geophys. Res.*, **103**, 24359.

Brandt, R. E., Warren, S. G., Worby, A. P., & Grenfell, T. C. 2005. Surface albedo of the Antarctic sea ice zone. *Journal of Climate*, **18**, 3606 –3622.

Brodeau, L., Barnier, B., Penduff, T., Treguier, A-M., & Gulev, S. 2008. An ERA40 based atmospheric forcing for global ocean circulation models. *Ocean Modelling, submitted*.

Bufe, C. G., & Varnes, D. J. 1993. Predictive modeling of the seismic cycle of the greater San Francisco Bay region. *J. Geophys. Res.*, **98**, 9871.

Burroughs, S. M., & Tebbens, S. F. 2002. The upper-truncated power law applied to earthquake cumulative frequency-magnitude distributions : Evidence for a time-independent scaling parameter. *Bulletin of the Seismological Society of America*, **92**, 2983.

Byerlee, J. D. 1978. Friction of rocks. *Pure Applied Geophysics*, **116**, 615–626.

Chessa, A., Vespignani, A., & Zapperi, S. 1999. Critical exponents in stochastic sandpile models. *Computer Physics Communications*, **121**, 299.

Colony, R., & Pritchard, R. S. 1975. Integration of elastic-plastic constitutive laws. *AIDJEX Bull.*, **30**, 55 – 80.

Comblen, R., Legrand, S., Deleersnijder, E., & Legat, V. 2008. A finite element method for solving the shallow water equations on the sphere. *Ocean Modelling*, **28**, 12 – 23.

Comiso, J., Parkinson, C. L., Gersten, R., & Stock, L. 2008. Accelerated decline in the Arctic sea ice cover. *Geophysical Research Letters*, **35**(L01703).

Comiso, J. C. 2002. A rapidly declining perennial sea ice cover in the Arctic. *Geophys. Res. Lett.*, **29**.

Comiso, J. C. 2005. Impacts of the variability of 2nd year ice types on the decline of the perennial ice cover. *Ann. Glaciol.*, **44**.

Comiso, J. C. 2006. Abrupt decline in the Arctic winter sea ice cover. *Geophys. Res. Lett.*, **33**(L18504).

Coon, M., Kwok, R., Levy, G., Pruis, M., Schreyer, H., & Sulsky, D. 2007. Arctic ice dynamics joint experiment (AIDJEX) assumptions revisited and found inadequate. *J. Geophys. Res.-Oceans*, **112**.

Coon, M. D., Maykut, G. A., Pritchard, R. S., & Rothrock, D. A. 1974. Modeling pack ice as an elastic-plastic material. *AIDJEX Bulletin*, **24**, 1–105.

Coulomb, C. A. 1773. Sur une application des règles de maximis et minimis à quelques problèmes de statique relatifs à l'architecture. *Acad. R. Sci. Mém. Math. Phys. Divers Savants*, **7**, 343 – 382.

Cowie, P. A., Sornette, D., & Vanneste, C. 1995. Multifractal scaling properties of a growing fault population. *Geophys. J. Int.*, **122**, 457.

Deschanel, S., Vanel, L., Godin, N., Vigier, G., & Ciliberto, S. 2009. Experimental study of crackling noise : conditions on power law scaling correlated with fracture precursors. *J. Stat. Mech.*, **P01018**.

Drakkar-Group. 2007. Eddy-permitting ocean circulation hindcasts of past decades. *CLIVAR Exchanges*, **12**(3).

Eicken, H., Grenfell, T. C., Perovich, D. K., Richter-Menge, J. A., & Frey, K. 2004. Hydraulic controls of summer Arctic pack ice albedo. *J. Geophys. Res.*, **109**(C08007).

Erlingsson, B. 1988. Two-dimensional deformation patterns in sea ice. *J. Glaciol.*, **34**, 301 – 308.

Evans, A. G. 1979. *Acoustic emission sources in brittle solids, in : Fundamentals of acoustic emission*. Ono K., (Ed) ; University of California, Los Angeles.

Feltham, D. L. 2005. Granular flow in the marginal ice zone. *Phil. Trans. R. Soc. A*, **363**, 1677 – 1700.

Feltham, D.L. 2008. Sea ice rheology. *Annual Review of Fluid Mechanics*, **40**, 91 – 112.

Fichefet, T., & Morales-Maqueda, M. A. 1997. Sensitivity of a global sea ice model to the treatment of ice thermodynamics and dynamics. *J. Geophys. Res.*, **102**, 12609 – 12646.

Fily, M., & Rothrock, D.A. 1990. Opening and closing of sea ice leads : digital measurements from synthetic aperture radar. *J. Geophys. Res.*, **95**, 789 – 796.

Fortt, A.L., & Schulson, E.M. 2007. The resistance to sliding along Coulombic shear faults in ice. *Acta Materialia*, **55**, 2253 –2264.

Frisch, U. 1995. *Turbulence : the legacy of A.N Kolmogorov*. Cambridge Univ. Press.

Frohlich, C., & Davis, S. D. 1990. Single-link cluster analysis as a method to evaluate spatial and temporal properties of earthquakes catalogues. *Geophys. J. Int.*, **100**, 19.

Gascard, J. C., Festy, J., le Goff, H., Weber, M., Bruemmer, B., Offermann, M., Doble, M., Wadhams, P., Forsberg, R., Hanson, S., Skourup, H., Gerland, S., Nicolaus, M., Metaxian, J. P., Grangeon, J., Haapala, J., Rinne, E., Haas, C., Heygster, G., Jakobson, E., Palo, T., Wilkinson, J., Kaleschke, L., Claffey, K., Elder, B., & Bottenheim, J. 2008. Exploring Arctic Transpolar Drift during dramatic sea ice retreat. *EOS*, **89**, 21 – 28.

Girard, L., Weiss, J., Molines, J.M., Barnier, B., & Bouillon, S. 2009. Evaluation of high-resolution sea ice models on the basis of statistical and scaling properties of Arctic sea ice drift and deformation. *J. Geophys. Res.*, **114**(C08015).

Girard, L., Amitrano, D., & Weiss, J. 2010a. Failure as a critical phenomenon in a progressive damage model. *Journal of Statistical Mechanics : Theory and Experiment*.

Girard, L., Bouillon, S., Weiss, J., Amitrano, D., Fichefet, T., & Legat, V. 2010b. A new modelling framework for sea ice mechanics based on elasto-brittle rheology. *submitted to Annals of Glaciology*.

Grasso, J. R., & Sornette, D. 1998. Testing self-organizing by induced seismicity. *J. Geophys. Res.*, **103**, 29965.

Gratier, J. P., & Gueydan, F. 2005. *Deformation in the presence of fluids and mineral reactions : effect of fracturing and fluid-rocks interaction on seismic cycle, in : The Dynamics of Fault Zones*. M.R. Handy, G. Hirth, N. Hovius, Dahlem Workshop, The MIT Press, Cambridge, Mass., USA.

Gray, J. M. N. T., & Morland, L. W. 1994. A two-dimensional model for the dynamics of sea ice. *Philos. Trans. R. Soc. Lond. A*, **347**, 219 – 290.

Griffith, A. A. 1920. The phenomena of rupture and flow in solids. *Philosophical Transactions of the Royal Society of London, Series A*, **221**, 163.

Guarino, A., Garcimartin, A., & Ciliberto, S. 1998. An experimental test of the critical behaviour of fracture precursors. *Eur. Phys. J. B.*, **6**, 13.

Gutenberg, B., & Richter, C.F. 1954. *Seismicity of the Earth and associated phenomenon*. Princeton University Press, Princeton.

Haas, C. 2004. Late-summer sea ice thickness variability in the Arctic Trans-polar Drift 1991-2001 derived from ground-based electromagnetic sounding. *Geophys. Res. Lett.*, **31**(L09402).

Hardebeck, J. L., Felzer, K. R., & Michael, A. J. 2008. Improved tests reveal that the accelerating moment release hypothesis is statistically insignificant. *J. Geophys. Res.*, **113**(B08310).

Heil, P., & Hibler, W. D. 2002. Modeling the high-frequency component of Arctic sea ice drift and deformation. *J. Phys. Oceanogr.*, **32**, 3039 – 3057.

Hemmer, P. C., & Hansen, A. 1992. The distribution of simultaneous fiber failures in fiber bundles. *J. Appl. Mech.*, **59**, 909.

Hentschel, H. G. E., & Proccacia, I. 1984. The infinite number of generalized dimensions of fractals and strange attractors. *Physica D*, **8**, 435.

Herrmann, H. J., & Roux, S. 1990. *Statistical models for the fracture of disordered media*. Amsterdam : North-Holland.

Hibler, W. D. 1977. A viscous sea ice law as a stochastic average of plasticity. *J. Geophys. Res.*, **82**, 3932 – 3938.

Hibler, W.D. 1979. A dynamic thermodynamics sea ice model. *J. Phys. Oceanogr.*, **9**, 815 – 846.

Hibler, W.D. 1986. *Ice dynamics, in Geophysics of Sea Ice, Ser. B : Physics*. Vol. 146. Plenum, New York, edited by N. Untersteiner.

Hirata, T., Satoh, T., & Ito, K. 1987. Fractal structure of spatial distribution of microfracturing in rock. *Geophys. J. R. Astron. Soc.*, **90**, 369.

Hopkins, M. A., & Thorndike, A. S. 2006. Floe formation in Arctic sea ice. *J. Geophys. Res. Oceans*, **111**(C11S23).

Hunke, E.C., & Dukowicz, J.K. 1997. An elastic-viscous-plastic model for sea ice dynamics. *J. Phys. Oceanography*, **27**, 1849 – 1867.

Hunke, E.C., & Lipscomb, W.H. 2001. *CICE : the Los Alamos sea ice model, documentation and software user's manual, http ://climate.lanl.gov/Models/CICE/*.

Hutchings, J. K., Roberts, A., Geiger, C., & Richter-Menge, J. 2010. Spatial and temporal characterisation of sea ice deformation. *submitted to Annals of Glaciology*.

Jaeger, J. C., & Cook, N. G. W. 1983. *Fundamentals of Rock Mechanics*. London, Chapman & Hall.

Jaume, S.C., & Sykes, L.R. 1999. Evolving Towards a Critical Point : A Review of Accelerating Seismic Moment/Energy Release Prior to Large and Great Earthquakes. *P. & A. Geoph.*, **155**, 279.

Kachanov, L. M. 1986. *Introduction to continuum damage mechanics*. Dordrecht, Boston, M. Nijhoff.

Kachanov, M. 1994. Elastic solids with many cracks and related problems. *Advances in Applied Mechanics*, **30**, 259.

Kagan, Y. Y. 1991. Fractal dimension of brittle fracture. *J. Nonlinear Sci.*, **1**, 1 – 16.

Kagan, Y. Y. 2007. Earthquake spatial distribution : the correlation dimension. *Geophys. J. Int.*, **168**, 1175.

Kagan, Y. Y., & Jackson, D. D. 1991. Long-term earthquake clustering. *Geophys. J. Int.*, **104**, 117 – 133.

Kagan, Y. Y., & Knopoff, L. 1980. Spatial distribution of earthquakes : The two point correlation function. *Geophys. J. R. Astron. Soc.*, **62**, 303.

Kanamori, H. 1978. Quantification of Earthquakes. *Nature*, **271**, 411.

Katz, O., & Reches, Z. 2004. Microfracturing, damage, and failure of brittle granites. *J. Geophys. Res.*, **109**(B01206).

Kwok. 1998a. Sea ice motion from satellite passive microwave imagery assessed with ERS SAR and buoy motions. *J. Geophys. Res.*, **103**, 8191 – 8214.

Kwok, R. 1998b. *The RADARSAT geophysical processor system, in Analysis of SAR data of the polar oceans : Recent Advances*. Springer, New York. Pages 235 – 257.

Kwok, R. 2001. *IUTAM Scaling Laws in Ice Mechanics and Ice Dynamics*. Kluwer Academic Publishers. Chap. Deformation of the arctic ocean sea ice cover between november 1996 and april 1997 : a survey, pages 315 – 322.

Kwok, R. 2006. Contrasts in sea ice deformation and production in the Arctic seasonal and perennial ice zones. *J. Geophys. Res.*, **111**(C11S22).

Kwok, R., & Rothrock, D. A. 2009. Decline in Arctic sea ice thickness from submarine and ICESat records : 1958-2008. *Geophys. Res. Lett.*, **36**(L15501).

Kwok, R., Hunke, E. C., Maslowski, W., Menemenlis, D., & Zhang, J. 2008. Variability of sea ice simulations assessed with RGPS kinematics. *J. Geophys. Res.*, **113**.

Kwok, R., Cunningham, G. F., Wensnahan, M., Rigor, I., Zwally, H. J., & Yi, D. 2009. Thinning and volume loss of the Arctic Ocean sea ice cover : 2003-2008. *J. Geophys. Res.*, **114**(C07005).

Laxon, S., Peacock, N., & Smith, D. 2003. High interannual variability of sea ice thickness in the Arctic region. *Nature*, **425**, 947 – 950.

Lemieux, J. F., Tremblay, B., Sedlacek, J., Tupper, P., Thomas, S., Huard, D., & Auclair, J. P. 2010. Improving the numerical convergence of viscous-plastic sea ice models with the Jacobian-free Newton-Krylov method. *Journal of Computational Physics*, **229**, 2840 – 2852.

Lemke, P., Ren, J., Alley, R.B., Allison, I., Carrasco, J., Flato, G., Fujii, Y., Kaser, G., Mote, P., Thomas, R.H., & Zhang, T. 2007. *Observations : Changes in Snow, Ice and Frozen Ground. In : Climate Change 2007 : The Physical Science Basis. Contribution of Working Group I to the Fourth Assessment Report of the Intergovernmental Panel on Climate Change*. Cambridge University Press, Cambridge, United Kingdom and New York, NY, USA.

Lietaer, O., Fichefet, T., & Legat, V. 2008. The effects of resolving the Canadian Arctic Archipelago in a finite element sea ice model. *Ocean Modelling*, **24**, 140 – 152.

Lindsay, R. W., & Zhang, J. 2005. The thinning of Arctic sea ice, 1988-2003 : Have we passed a tipping point ? *Journal of Climate*, **18**, 4879 – 4894.

Lindsay, R.W., & Stern, H.L. 2003. The RADARSAT geophysical processor system : Quality of sea ice trajectory and deformation estimates. *Journal of Atmospheric and Oceanic Technology*, **20**, 1333 – 1347.

Lindsay, R.W., Zhang, J., & Rothrock, D.A. 2003. Sea-ice deformation rates from satellite measurements and in a model. *Atmosphere-Ocean*, **41**, 35 – 47.

Lipscomb, W.H. 2001. Remapping the thickness distribution in sea ice models. *J. Geophys. Res.-Oceans*, **106**, 13989 – 14000.

Lique, C., Treguier, A. M., Scheinert, M., & Penduff, T. 2009. A model-based study of ice and freshwater transport variability along both sides of Greenland. *Climate Dynamics*, **33 (5)**, 685 – 705.

Lockner, D. 1993. The role of acoustic emission in the study of rock fracture. *Int. J. Rock. Mech. Min. Sci. & Geomech. Abstr.*, **30**, 883.

Lockner, D. A., & Byerlee, J. D. 1991. Vth Conf. AE/MS Geol. Str. and Mat. (ed. Hardy). Trans Tech publications, Germany, The pennsylvania State University.

Lockner, D. A., Byerlee, J. D., Kuskenko, V., Ponomarev, A., & Sidorin, A. 1991. Quasi-static fault growth and shear fracture energy in granite. *Nature*, **350**, 39.

Lüpkes, C., Vihma, T., Birnbaum, G., & Wacker, U. 2008. Influence of leads in sea ice on the temperature of the atmospheric boundary layer during polar night. *Geophys. Res. Lett.*, **35**.

Main, I. 1996. Statistical physics, seismogenesis, and seismic hazard. *Reviews of Geophysics*, **34**, 433.

Marko, J. R., & Thomson, R. E. 1977. Rectilinear leads and internal motions in the ice pack of the western Arctic ocean. *J. Geophys. Res.*, **82**, 979 – 987.

Marsan, D., Stern, H., Lindsay, R., & Weiss, J. 2004. Scale dependence and localization of the deformation of arctic sea ice. *Phys. Rev. Lett.*, **93**(178501).

Martin, S., & Thorndike, A.S. 1985. Dispersion of sea ice in the Bering Sea. *J. Geophys. Res.*, **90**, 7223 – 7226.

Maslowski, W., & Lipscomb, W.H. 2003. High resolution simulations of Arctic sea ice, 1979-1993. *Polar Research*, **22**, 67 – 74.

Maykut, G.A. 1982. Large scale heat exchange and ice production in the central Arctic. *J. Geophys. Res.*, **87**, 7971 – 7984.

Maykut, G.A. 1986. *The surface heat and mass balance, in Geophysics of Sea Ice, Ser. B : Physics*. Vol. 146. Plenum, New York, edited by N. Untersteiner.

Maykut, G.A., & Untersteiner, N. 1971. Some results from a time dependent thermo-dynamic model of sea ice. *J. Geophys. Res.*, **76**, 1550 – 1575.

McBean, G., Alekseev, G., Chen, D., Fï¿½rland, E., Fyfe, J., Groisman, P. Y., King, R., Melling, H., Vose, R., & Whitfield, P. H. 2005. *Arctic Climate Impact Assessment report*. Cambridge University Press. Chap. Chapter 2 : Arctic climate : Past and present.

McPhee, M.G. 1975. Ice-ocean momentum transfer for the AIDJEX ice model. *AIDJEX Bull.*, **29**, 93 – 111.

Moritz, R.E., & Stern, H.L. 2001. *Scaling Laws in Ice Mechanics and Ice Dynamics*. Kluwer Academic Publishers. Chap. Relationships between geostrophic winds, ice strain rates and the piecewise rigid motions of pack ice, pages 335 – 348.

Moritz, R.E., Bitz, C.M., & Steig, E.J. 2002. Dynamics of recent climate change in the Arctic. *Science*, **297**, 1497 – 1502.

Nechad, H., Helmstetter, A., Guerjouma, R. El, & Sornette, D. 2005. Creep ruptures in heterogeneous materials. *Phys. Rev. Lett*, **94**, 045501.

Nye, J. F. 1973. Is there any physical basis for assuming linear viscous behavior for sea ice ? *AIDJEX Bulletin*, **21**.

Parmerter, R. R., & Coon, M. D. 1973. Mechanical model of ridging in the Arctic sea ice cover. *AIDJEX Bull.*, **19**, 59 – 112.

Perovich, D. K., Grenfell, T. C., Light, B., & Hobbs, P. V. 2002. Seasonal evolution of the albedo of multiyear Arctic sea ice. *J. Geophys. Res.*, **107**(8044).

Petri, A., Paparo, G., Vespignani, A., Alippi, A., & Costantini, M. 1994. Experimental evidence for critical dynamics in microfracturing processes. *Phys. Rev. Lett.*, **73**, 3423.

Petrich, C., Langhorne, P. J., & Haskell, T. G. 2007. Formation and structure of refrozen cracks in land-fast first-year sea ice. *J. Geophys. Res.*, **112**(C04006).

Pfirman, S. L., Colony, R., Nurnberg, D., Eicken, H., & Rigor, I. 1997. Reconstructing the origin and trajectory of drifting Arctic sea ice. *J. Geophys. Res.*, **102**, 12575 – 12586.

Picallo, C. B., & Lopez, J. M. 2008. Energy dissipation statistics in the random fuse model. *Phys. Rev. E*, **77**(046114).

Pradhan, S., Hansen, & Hemmer, P.C. 2005. Crossover behavior in burst avalanches : Signature of imminent failure. *Phys. Rev. Lett.*, **95**, 125501.

Pradhan, S., Hansen, & Hemmer, P. C. 2009. *IUTAM Symposium on Scaling in Solid Mechanics*. F. M. Borodich, Springer. Chap. Burst statistics as a criterion for imminent failure, page 165.

Pringle, D. J., Eicken, H., Trodahl, H. J., & Backstrom, L. 2007. Thermal conductivity of landfast Antarctic and Arctic sea ice. *J. Geophys. Res.*, **112**(C04017).

Rampal, P. 2008. *Etude de la dérive et de la déformation de la banquise Arctique par l'analyse de trajectoires lagrangiennes*. Thèse de doctorat de l'université J. Fourier, Grenoble I.

Rampal, P., & Weiss, J. 2010. IPCC climate models strongly underestimate Arctic sea ice thinning and drift acceleration. *submitted to J. Geophys. Res.*

Rampal, P., Weiss, J., Marsan, D., Lindsay, R., & Stern, H. 2008. Scaling properties of sea ice deformation from buoy dispersion analyses. *J. Geophys. Res.*, **113**.

Rampal, P., Weiss, J., Marsan, D., & Bourgoin, M. 2009a. Arctic sea ice velocity field : General circulation and turbulent-like fluctuations. *J. Geophys. Res.*, **114**.

Rampal, P., Weiss, J., & Marsan, D. 2009b. Positive trend in the mean speed and deformation rate of Arctic sea ice, 1979-2007. *J. Geophys. Res.*, **114**.

Richter-Menge, J. A., McNutt, S. L., Overland, J. E., & Kwok, R. 2002. Relating Arctic pack ice stress and deformation under winter conditions. *J. Geophys. Res.*, **107**(8040).

Rothrock, D., Percival, D. B., & Wensnahan, M. 2008. The decline in arctic sea-ice thickness : Separating the spatial, annual, and interannual variability in a quarter century of submarine data. *J. Geophys. Res.*, **113**(C05003).

Rothrock, D. A. 1975. The energetics of the plastic deformation of pack ice by ridging. *J. Geophys. Res.*, **80**, 4514 – 4519.

Salminen, L. I., Tolvanen, A. I., & Alava, M. J. 2002. Acoustic emission from paper fracture. *Phys. Rev. Lett.*, **89**, 185503.

Schofield, A., & Wroth, P. 1968. *Critical State Soil Mechanics*. New York : McGraw-Hill.

Scholz, C. H. 1968. The frequency-magnitude relation of microfracturing in rock and its relation to earthquakes. *Bulletin of the Seismological Society of America*, **58**, 399.

Schreyer, H. L., Sulsky, D. L., Munday, L. B., Coon, M. D., & Kwok, R. 2006. Elastic-decohesive constitutive model for sea ice. *J. Geophys. Res.*, **3**(C11S26).

Schulson, E. M. 2004. Compressive shear faults within the Arctic sea ice : fracture on scales large and small. *J. Geophys. Res.*, **109**(C07016).

Schulson, E. M., & Duval, P. 2009. *Creep and fracture of ice*. Cambridge university press. Chap. Elasticity, friction and diffusivity, pages 62 – 63.

Schulson, E. M., Fortt, A. L., Iliescu, D., & Renshaw, C. E. 2006a. Failure envelope of first-year Arctic sea ice : the role of friction in compressive failure. *J. Geophys. Res.*, **111**(C11S25).

Schulson, E.M., & Hibler, W.D. 1991. The fracture of ice on scales large and small : arctic leads and wing cracks. *J. Glaciol.*, **37**, 319 – 322.

Schulson, E.M., Fortt, A.L., Iliescu, D., & Renshaw, C.E. 2006b. Failure envelope of first-year Arctic sea ice : The role of friction in compressive fracture. *J. Geophys. Res.*, **111**(C11S25).

Serreze, M. C., Holland, M. M., & Stroeve, J. 2007. Perspectives on the Arctic's shrinking sea-ice cover. *Science*, **315**, 1533 – 1536.

Sethna, J. P., Dahmen, K. A., & Myers, C. R. 2001. Crackling noise. *Nature*, **410**, 242.

Smith, W. D. 1981. The b-value as an earthquake precursor. *Nature*, **289**.

Sornette, A., & Sornette, D. 1989. Self-organized criticality and earthquakes. *Europhys. Lett.*, **9**, 197.

Sornette, A., Davy, P., & Sornette, D. 1990. Growth of fractal fault patterns. *Phys. Rev. Lett.*, **64**, 2266 – 2269.

Sornette, D. 2000. *Critical phenomena in Natural Sciences*. Springer, Berlin.

Sornette, D., & Andersen, J. V. 1998. Scaling with respect to disorder in time-to-failure. *Eur. Phys. J. B.*, **1**, 353.

Sorteberg, A., Kattsov, V., Walsh, J.E., T., A.F., & Pavlova. 2007. The arctic surface energy budget as simulated with the IPCC AR4 AOGCMs. *Climate Dynamics*, **29**, 131 – 156.

Stauffer, D., & Aharony, A. 1994. *Introduction to Percolation Theory*. Taylor and Francis, London.

Stern, H. L., & Lindsay, R. W. 2009. Spatial scaling of Arctic sea ice deformation. *J. Geophys. Res.*, **114**(C10017).

Stroeve, J., Holland, M. M., Meier, W., Scambos, T., & Serreze, M. 2007. Arctic sea ice decline : Faster than forecast. *Geophys. Res. Lett.*, **34**(L09501).

Sulsky, D., Schreyer, H., Peterson, K., Kwok, R., & Coon, M. 2007. Using the material-point method to model sea ice dynamics. *J. Geophys. Res.*, **112**(C02S90).

Taylor, P.D., Feltham, D., Sammonds, P.R., & Hatton, D. 2006. Continuum sea ice rheology determined from subcontinuum mechanics. *J. Geophys. Res.*, **11**.

Thomas, D. 1999. The quality of sea ice velocity estimates. *J. Geophys. Res.*, **104**, 13627 – 13652.

Thorndike, A. S., Rothrock, D. A., Maykut, G. A., & Colony, R. 1975. The thickness distribution of sea ice. *J. Geophys. Res.*, **80**, 4501 – 4513.

Thorndike, A.S. 1986. *The geophysics of sea ice*. Plenum Press, New York. Chap. Kinematics of sea ice, pages 489 – 549.

Thorndike, A.S., & Colony, R. 1980. *Arctic Ocean Buoy Program Data Report*. Tech. rept. Applied Physics Laboratory, University of Washington, Seattle WA.

Thorndike, A.S., & Colony, R. 1982. Sea ice motion in response to geostrophic winds. *J. Geophys. Res.*, **87**, 5845 – 5852.

Tremblay, L.-B., & Mysak, L. A. 1997. Modeling Sea Ice as a Granular Material, Including the Dilatancy Effect. *J. of Phys. Oceanography*, **27**, 2342 – 2360.

Wadhams, P., & Davis, N. R. 2000. Further evidence of ice thinning in the Arctic Ocean. *Geophys. Res. Lett.*, 3973 – 3975.

Wang, K., & Wang, C. 2009. Modeling linear kinematic features in pack ice. *J. Geophys. Res.*, **114**(C12011).

Weibull, W. 1939. A statistical theory of the strength of materials. *Proc. Royal Swedish Academy of Eng. Sci.*, **151**, 5–45.

Weiss, J. 2003. Scaling of fracture and faulting in ice on Earth. *Surveys of Geophysics*, **24**, 185.

Weiss, J. 2008. Intermittency of principal stress directions within Arctic sea ice. *Physical Review E*, **77**.

Weiss, J., & Marsan, D. 2004. Scale properties of sea ice deformation fracturing. *C. R. Physique*, **5**.

Weiss, J., & Schulson, E. M. 2009. Coulombic faulting from the grain scale to the geophysical scale : lessons from ice. *J. Phys. D : Appl. Phys.*, **42**(214017).

Weiss, J., Schulson, E.M., & Stern, H.L. 2007. Sea ice rheology from in-situ, satellite and laboratory observations : Fracture and friction. *Earth Planet. Sci. Lett.*, **255**.

Weiss, J., Marsan, D., & Rampal, P. 2009. *IUTAM Symp. on Scaling in Solid Mechanics, IUTAM Book Series vol 10*. P Borodich (Berlin : Springer). Chap. Space and time scaling laws induced by the multiscale fracturing of the Arctic sea ice cover, pages 101 – 109.

Wettlaufer, J. S., Worster, M. G., & Huppert, H. E. 2000. Solidification of leads : Theory, experiment, and field observations. *J. Geophys. Res.*, **105**, 1123 – 1134.

Wilchinsky, A. V., & Feltham, D. L. 2004. A continuum anisotropic model of sea-ice dynamics. *Proc. R. Soc. Lond. A*, **460**, 2105 – 2140.

Wilchinsky, A. V., & Feltham, D. L. 2006a. Anisotropic model for granulated sea ice dynamics. *J. Mech. Phys. Solids*, **54**, 1147 – 1185.

Wilchinsky, A. V., & Feltham, D. L. 2006b. Modelling the rheology of sea ice as a collection of diamond-shaped floes. *J. Non-Newtonian Fluid Mech.*, **138**, 22 – 32.

Wilchinsky, A. V., Feltham, D. L., & Hopkins, M. A. 2010a. The effect of shear rupture on aggregate scale formation in sea ice. *J. Geophys. Res.*, **in press**.

Wilchinsky, A. V., Feltham, D. L., & Hopkins, M. A. 2010b. Modelling the re-orientation of sea ice faults as the wind changes direction. *Annals of Glaciology*, **this issue**.

Zapperi, S., Vespignani, A., & Stanley, E. 1997. Plasticity and avalanche behaviour in microfracturing phenomena. *Nature*, **388**, 658.

Zapperi, S., Cizeau, P., Durin, G., & Stanley, H. E. 1998. Dynamics of a ferromagnetic domain wall : Avalanches, depinning transition, and the Barkhausen effect. *Phys. Rev. B*, **58**, 6353.

Zapperi, S., Nukala, P. K. V. V., & Simunovic, S. 2005. Crack roughness and avalanche precursors in the random fuse model. *Phys. Rev. E*, **71**(026106).

Zhang, H. M., Prater, M., & Rossby, T. 2001. Isopycnal Lagrangian statistics from the North Atlantic Current RAFOS float observations. *J. Geophys. Res.*, **106**, 13 817 – 13836.

Zhang, J., Rothrock, D., & Steele, M. 2000. Recent changes in arctic sea ice : the interplay between ice dynamics and thermodynamics. *Journal of Climate*, **13**, 3099 – 3114.

Zoller, G., Hainzl, S., & Kurths, J. 2001. Observation of growing correlation length as an indicator for critical point behavior prior to large earthquakes. *J. Geophys. Res.*, **106**, 2167.